Deep-Sea Nodule Mining

Vertical transportation of collected manganese nodules by means of mechanical lifting

S.L.J. Graat

30-11-2017

TU Delft

Deep-Sea Nodule Mining

Vertical transportation of collected manganese nodules by means of mechanical lifting

by

S.L.J. Graat

to obtain the degree of Master of Science
at the Delft University of Technology,
to be defended publicly on Thursday November 30, 2017 at 14:30 PM.

Student number:	4335511	
Project duration:	Februari 6, 2017 – November 30, 2017	
Thesis committee:	Prof. dr. A. Metrikine,	TU Delft, supervisor
	Dr. ir. H. Hendrikse,	TU Delft
	Dr. ir. F. Pisanó,	TU Delft
	Ing. G. Visch,	Royal Boskalis Westminster NV

This thesis is confidential and cannot be made public until 30-11-2022.

TU Delft Boskalis

Abstract

With a rapidly growing population and subsequent technological developments, an increase in demand of rare-earth metals evolves. Land-based deposits seem to be insufficient and shortage impends within the coming decades. Mineral resources from the deep ocean are considered as a possible complement. These minerals occur in various forms. One of these forms is lying on the subsea sediment of the deep ocean; polymetallic nodules. The nodules can be best described as potato shaped objects containing amounts of rare earth minerals like copper, nickel and cobalt. The economic feasibility depends on nodule abundance per square meter. An exploitation region with high prospectiveness in terms of economic feasibility is the Clarion-Clipperton Zone, a region in the centre of the Pacific Ocean. As deep-sea mining implies, the mining site is located at a water depth of approximately $4000m$. Characteristics such as these automatically result into challenging conditions. Exploitation of the nodules includes subsea harvesting and vertical transportation towards the sea surface. Activities which are within the scope of Boskalis, appealing their know-how and experience in dredging and marine operations. Currently, most developments are focused on vertical transport by means of hydraulic lifting through a riser. In order to avoid challenges such as flow assurance, riser handling and efficiency, Boskalis proposes an alternative solution; mechanical lifting.

Mechanical lifting can be considered as a newcomer in the relative early field of deep-sea mining. However, experience can be gathered from successive deep-sea lowering operations in the oil and gas industry. The objective of this thesis is to investigate the static configuration and dynamic response of the proposed mining system during operation, identify potential showstoppers and in the end asses whether deep-sea mining by mechanical lifting is technical feasible. When simplified, it is merely a matter of collection of nodules in transportation skips and hoisting of these skips towards the sea surface. Nevertheless, within this simple procedure various challenges arise. Therefore a start is made with a proper description of the proposed production method and identification of potential hazards and showstoppers. In complementing the initial research, the project site has been studied in terms of sea floor characteristics and metocean data. These obtained results served as input in further analysis. For example a sheared current is present, influencing the geometry of the hoisting wires. The sheared current phenomenom has been studied in which a quasi-static analysis is performed. The analysis has been carried out by discretization of the hoisting wires in a number of elements with a payload attached at the tip acting as a sinker. Here it became clear that for the applied hoisting setup, the influence of the local current is minimal and the influence of a forward vessel motion significant.

When acting in an offshore environment, the vessel motions might affect the deep-sea mining operation as a result of the connection with the nodule collector. Preliminary to a dynamic analysis, typical vessel motions are determined. This is done by selection of an appropriate mining vessel and implementation of a characteristic sea state using a Pierson-Moskowitz spectrum. Vessel motions are calculated with the software package Seaway, resulting in an output in the frequency domain. The suspended hoisting wires are still numerically modelled by a discretization method. Axial analysis for the applied hoisting setup shows significant magnification of the response of the attached payload at full depth ($4000m$). This hurdle should be overcome by applying heave compensation, which has become a commonplace in this type of marine operations. Transversal motions for the applied setup are expected to be minimal as a result of the submerged state.

Conclusively, within this research first insight in technical feasibility is gained, but as a matter of fact yield further valuable questions along the lines of deep-sea technology. Therefore, we can conclude that deep-sea mining by means of mechanical lifting is feasible, but still offers numerous interesting topics in future research exceeding the current standards.

Preface

This report has been written in order to fulfill the requirements for the master program Offshore and Dredging Engineering at the Delft University of Technology. The study covers the topic of feasibility of mechanical lifting in deep-sea mining operations and is performed in collaboration with the R&D department of Royal Boskalis Westminster NV. The R&D department is concerned with divergent engineering topics covering all Boskalis' divisions and founded on extensive in-house knowledge and experience.

Deep-sea nodule mining by means of mechanical lifting is a topic I experienced as challenging. Gradually more interesting fields of research came across and defining a clear scope became essential. Nevertheless, the variety in engineering was pleasurable, something which resulted into a highly informative and instructive process. Conclusively I consider deep-sea operations as a topic that further sparked my interest in the offshore industry.

I would like to thank Boskalis for giving me the opportunity to conduct my graduation, offering me an interesting topic and providing me with a comfortable working environment. Furthermore I would like to thank my graduation committee Prof.Dr. A. Metrikine, Dr.ir. H. Hendrikse and Ing. G. Visch for their guidance, daily support and fruitful progress meetings. Finally I would like to thank my family, friends and fellow (graduate) students for their support and advice during the entire process.

S.L.J. Graat
Gendringen, November 2017

Nomenclature

List of Abbreviations

AHC	Active Heave Compensation
CCZ	Clarion-Clipperton Zone
CLB	Continuous Line Bucket System
CoG	Center of Gravity
DAF	Dynamic Amplification Factor
DISH	Deepwater Installation of Subsea Hardware
DP	Dynamic Positioning
DSM	Deep Sea Mining
FM	Forward Motion
HYCOM	Hybrid Coordinate Model
ISA	International Seabed Authority
MBF	Maximum Breaking Force
MBL	Maximum Breaking Load
ODE	Ordinary Differential Equation
PHC	Passive Heave Compensation
PSSV	Production-, Support- and Storage Vessel
RAO	Response Amplitude Operator
REE	Rare Earth Elements
RMS	Root Mean Squared
SMS	Seafloor Massive Sulphides
SWL	Safe Working Load
UTS	Ultimate Tensile Strength
WLL	Working Load Limit

List of Greek symbols

ζ	Wave surface elevation	m
ζ_a	Amplitude wave surface elevation	m
α_d	Material damping coefficient	[-]
δ_w	Wire elongation	m
γ_{soil}	Unit weight of soil	N/m^3

μ_{fric}	Coefficient of friction between soil and collector tracks	[-]
Ω	Exciting frequency	rad/s
ω_0	Peak frequency	rad/s
ϕ	Roll direction	rad
ψ	Yaw direction	rad
ρ_{nod}	Bulk density of nodules	kg/m^3
ρ_{st}	Density of steel	kg/m^3
ρ_w	Density of water	kg/m^3
σ_{η_r}	Standard deviation of the relative heave motion	m
σ_T	Standard deviation of the dynamic tension	N
θ	Pitch direction	rad

List of Latin symbols

$H(\omega)$	Transfer function of response amplitude operator	m/m
$H_r(\omega)$	Transfer function of the RAO relative heave motion	m/m
m_n	Spectral moment of n^{th} order	[-]
$\overline{u}_{cur}$	Mean current velocity	m/s
A_w	Cross-sectional surface area wire	m^2
A_{coll}	Track area nodule collector	m^2
A_{skip}	Area skip	m^2
c	Soil cohesion	Pa
$C_{D;skip}$	Skip drag coefficient	[-]
$C_{D;wire}$	Wire drag coefficient	[-]
C_{Df}	Tangential drag coefficient as result of skin friction	[-]
C_{fm}	Velocity nodule collector (forward motion)	m/s
c_{phc}	Passive heave compensator damping constant	Ns/m
D_w	Diameter of wire	m
E	Modulus of elasticity	Pa
EA	Axial rigidity	N
$F_{c;tot;x}$	Sum of forces acting on nodule collector in x-direction	N
$F_{c;tot;z}$	Sum of forces acting on nodule collector in z-direction	N
F_{comp}	Compensator stiffness and damping forces as result of nodal displacement	N
$F_{d;c;x}$	Drag force on collector in x-direction	N
$F_{d;hoist}$	Drag force as a result of hoisting	N
$F_{d;wire;x}$	Wire drag force in x-direction	N/m

$F_{d;wire;z;tot}$	Total wire drag force in z-direction	N
$F_{d;wire;z}$	Wire drag force in z-direction	N/m
$F_{hoist;max}$	Maximum hoisting force	N
$F_{v;tot;x}$	Sum of forces acting on mining vessel in x-direction	N
$F_{v;tot;z}$	Sum of forces acting on mining vessel in z-direction	N
g	Gravitational acceleration	m/s^2
H_s	Significant wave height	m
k_{phc}	Passive heave compensator stiffness constant	N/m
l	Element length after discretization	m
L_s	Stretched wire length	m
L_{pay}	Wire payout length	m
m_A	Added mass	kg
m_w	Mass of wire per unit length	kg/m
$P_{max;req}$	Maximum required hoisting power	W
q_u	Soil bearing capacity	Pa
$S_{\eta_r}(\omega)$	Energy density spectrum of the relative heave motion	m^2s
$S_\zeta(\omega)$	Energy density spectrum of wave surface elevation	m^2s
$S_{ct}(\omega)$	Energy density spectrum of crane-tip motion	m^2s
T_p	Peak period	s
T_z	Mean zero crossing period	s
$T_{dyn;mpm}$	Most probable maximum dynamic tension	N
T_{dyn}	Dynamic tension	N
T_{stat}	Static tension	N
T_{tot}	Total tension	N
U_0	Amplitude of exciting motion	m
u_{ct}	Displacement of the crane-tip	m
$u_{cur;max}$	Maximum current velocity	m/s
$u_{cur;min}$	Minimum current velocity	m/s
$u_{cur;res}$	Resultant current velocity	m/s
u_{cur}	Current velocity	m/s
V_{fm}	Velocity mining vessel (forward motion)	m/s
v_{hoist}	Hoisting velocity	m/s
$v_{low;max}$	Maximum lowering velocity	m/s
w_w	Weight of wire per unit length	N/m

$W_{c;s;req}$	Required submerged weight of nodule collector	N
$W_{c;s}$	Submerged weight of nodule collector	N
$W_{skip;e}$	Weight empty skip	N
$W_{skip;f}$	Weight of full skip loaded with nodules	N
$w_{w;s}$	Weight of submerged wire per unit length	N/m
x	Longitudinal direction/ coordinate - Surge direction	m
y	Lateral direction/ coordinate - Sway direction	m
z	Vertical direction/ coordinate - Heave direction	m

List of Figures

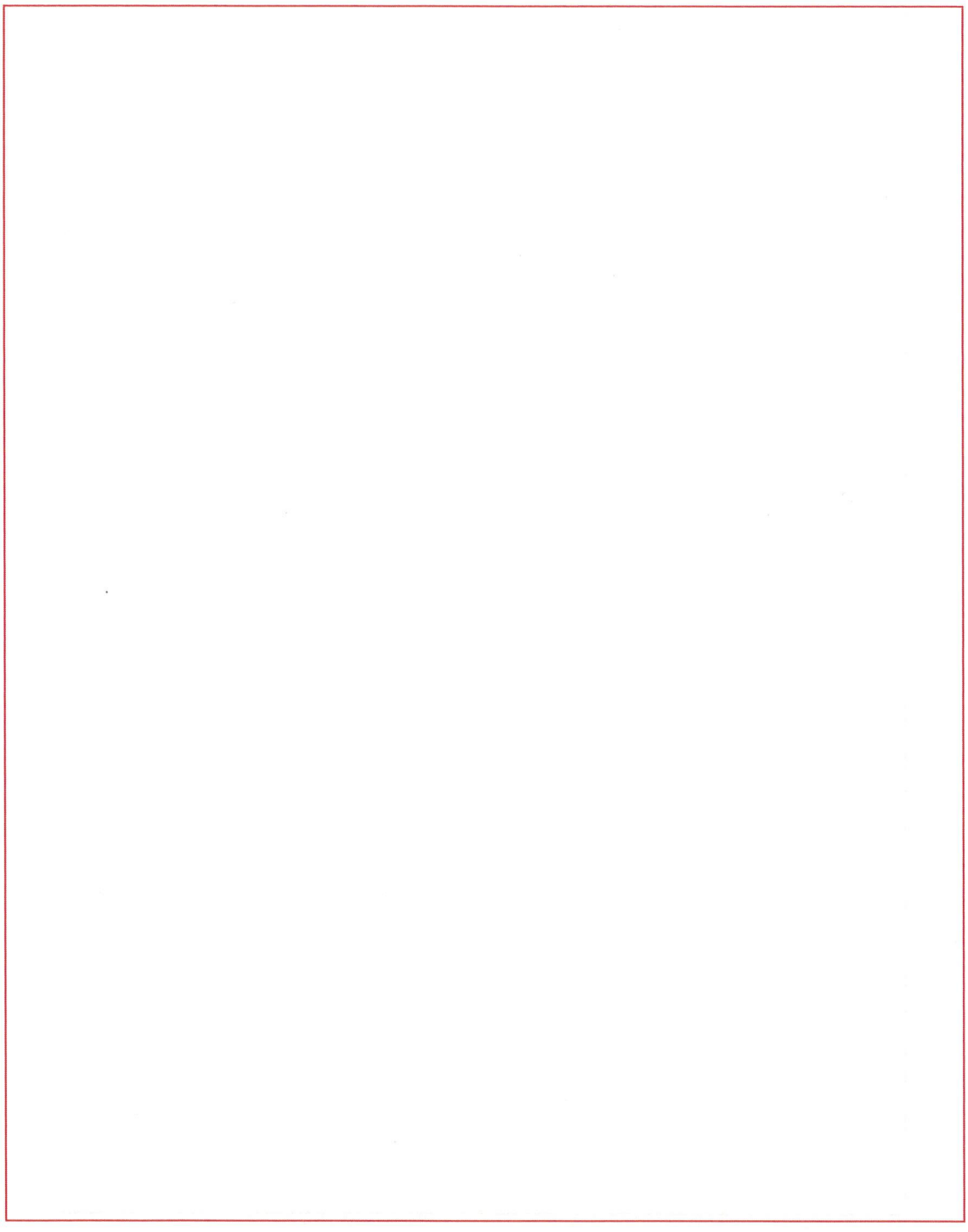

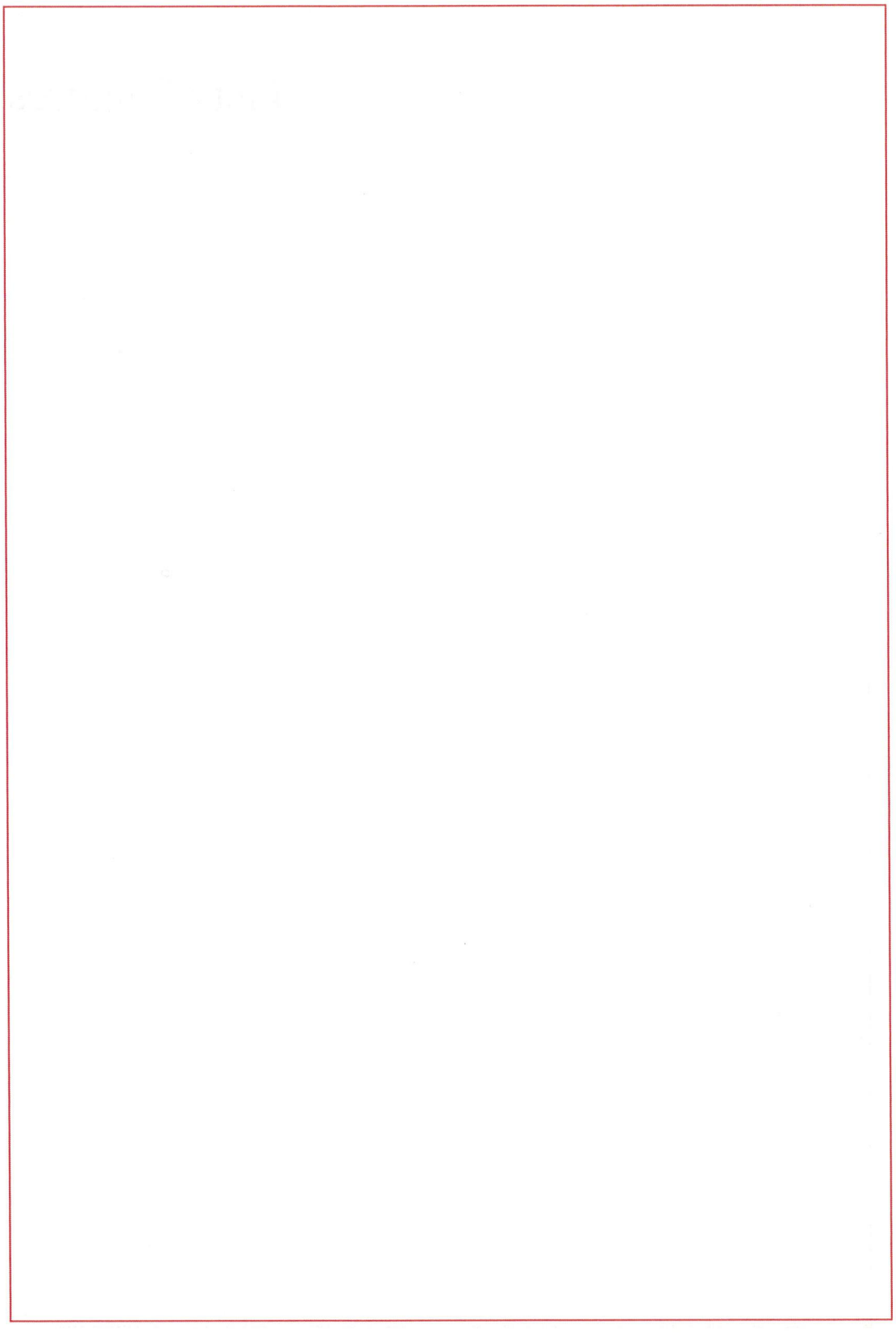

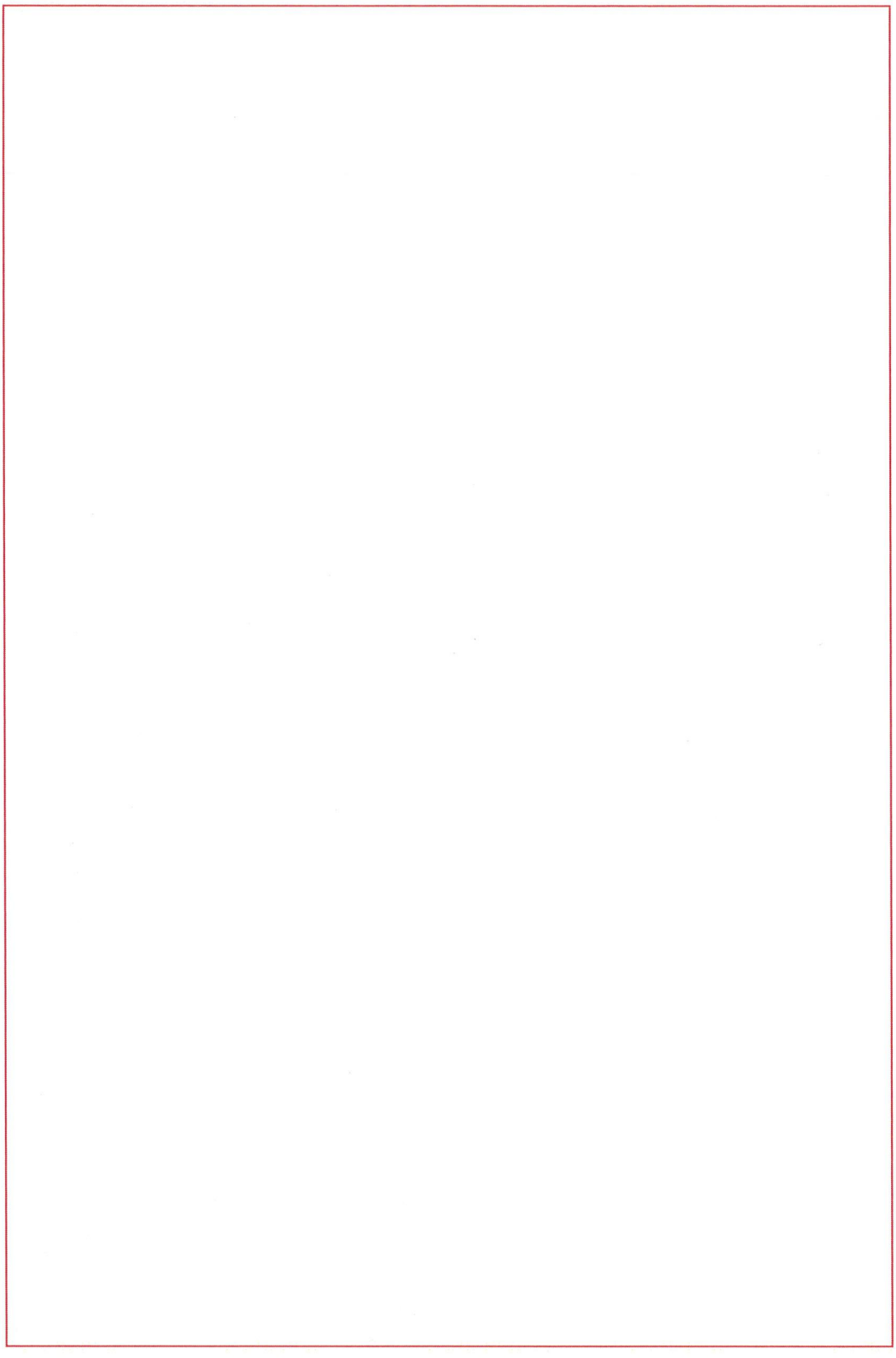

List of Tables

Contents

1 Introduction

1.1. Background

In the Clarion-Clipperton Zone (CCZ), a site which is located in the Pacific Ocean, a vast part of the ocean floor is covered with potato sized manganese nodules. These nodules can be considered as valuable polymetallic resources of great interest with respect to rare-earth metals. The recovery site is located in waters of approximately $4000m$ of depth. This results in challenging conditions in terms of collection and especially vertical transportation of these nodules to the sea surface. In the past this vertical transport was mainly attempted by means of hydraulic- or pneumatic lifting through a riser. A by Boskalis proposed mining method of alternative vertical transport is hoisting of filled containers by means of mechanical lifting. This can be considered as a sound method, whereas the vital parts of the system are mainly located above the waterline and complex subsystems will be absent. The central topic in this thesis will be a technical feasibility study of this proposed mining method.

1.2. Historical Overview

The resources of the deep oceans are known for about a century, when during the scientific research expedition of the HMS Challenger (1872-1876) potato shaped nodules were fished out of the deep. Nodules were actually already discovered in the Kara Sea and the Arctic Ocean of Siberia (1868). Commercial interest in this particular type of marine mineral resource was, with sufficient land-based resources, not addressed. This simmering interest was sparked when metal prices raise during the late sixties and John Mero published his book *'The mineral resources of the sea'* [25].

From 1957 till 1965 Mero wrote different papers and books regarding the topic, calling attention to the considerable potential value of minerals located on the ocean floor. With the offshore oil and gas successes in mind, producing minerals from the deep ocean became a probable feasible scenario, or at least worth investigating. This commercial interest resulted into the start-up in research and development of different technologies. Especially during the seventies when metal prices peaked, different experiments where done. Some of these tests indeed showing the feasibility of production. Besides a few out-of-the-box ideas (continuous-line-buckets and autonomous shuttles) most of the research was focused on riser technology, using hydraulic or pneumatic lifting methods. Eventually in the case of the latter methods, it led to practical tests and recovery of an amount of 600 tons nodules from the seafloor using a screw-driven collector and a hydraulic lifting system. When the metal prices dropped and new land-based resources were discovered, most of the plans were frozen. However, due to expected forthcoming shortages in rare-earth metals coming decades, a deep-sea revival impends. Currently, Canadian based Nautilus Minerals is in a late stage of exploiting Seafloor Massive Sulphide (SMS) crusts; again using riser technology. Recent developments concerning polymetallic nodule mining in general and mechanical lifting in particular are scarce and still belong to the future.

1.2.1. Deep-Sea Mining Projects

During the past decades multiple parties tried to conquer the abyssal planes of the deep ocean, with various success. An overview of the most promising and remarkable projects and parties is given in Table 1.1.

Year	Method	Characteristics	Ventures
1970	Hydraulic Lift	Atlantic Ocean-Florida	Deep Sea Ventures
1972	Continuous Line Bucket System	Japan	Japanese Syndicate
1972	Hydraulic Lift and Airlift	Hawaii; Depth 5400m; 600 tons collected; Sedco 445 Drill ship	Ocean Management (OMI)
1976	Airlift	CCZ; 550 tons collected; Production rate 50t/ hr	Ocean Mining Associates (OMA)
1978	Hydraulic Lift	Glomar Explorer; Amphirol collector; Depth 1800m	Ocean Minerals Company (OMCO)
1988	Hydraulic Lift	Platform with pipeline. 330 tons towed Seabed dredge.	Genomod
2006	Hydraulic Lift	Papua New Guinea; Solwara 1.	Nautilus Minerals; Tonga
2011	Hydraulic Lift	Research and Development	Oceanflore
2013	Hydraulic Lift	Research and Development	Lockheed Martin

Table 1.1: Overview deep-sea mining projects and ventures

That the interest in marine mineral resources revived, shows the start-up of the most recent deep-sea mining project Solwara 1 (2006) [15]. Within the Bismarck Sea in the vicinity of Papua New Guinea, Nautilus Minerals is experimenting with the deep-sea mining of Seafloor Massive Sulphides (SMS), which contain a large amount of gold, silver and other rare-earth elements (REE). The seafloor machinery has already been developed and built and recently the mining vessel is being prepared.

1.3. Problem Description and Objective

1.4. Research Question

The problem description and objective can be cast in following research question:

Main question

Is vertical transportation by means of mechanical lifting a technical feasible method in deep-sea mining?

This research question leads to the following set of preliminary sub-questions:

Sub-questions

1.5. Approach

1.6. Outline and Scope

2

Mining of Marine Mineral Resources

The oceans cover almost three quarters of surface area of our planet and are abundant in various natural resources. Metallic resources of the deep-ocean however, are still a relatively new unmoved reserve. In this chapter a brief introduction with respect to mining of mineral resources is given. In the following sections further information regarding the mineral market, mineral resources and proposed mineral mining methods is covered.

2.1. Marine Mineral Market

Mankind is confronted with a rapidly growing global population. Subsequently, economies of Brazil, Russia, India and China are developing rapidly as well. As more countries get developed and the middle class is growing, resources are required to develop a sustainable energy future [13, 22]. Especially rare-earth metals are needed to support development of high-tech energy solutions. Many of these rare elements are available from increasing limited sources. For example, China is a major producer and holds a monopoly but mainly focuses on the internal market, resulting in a shortage of rare-earth elements on the global market. Here the deep-ocean minerals provide an outcome. In the past, three factors kept mankind from exploitation: low metal prices as a result of sufficient land-based reserves, feasibility of deep-sea mining technology and quantification and mitigation of environmental impacts [1]. However, market developments like mentioned above can rekindle the interest. Perhaps deep-sea mining cannot replace land-based mining in the near future in terms of scale and output, but it can at least complement it. With respect to feasibility in technology, the deep-water successes of the oil and gas industry feed the confidence. Proven deep-water riser technology for example, can become the backbone of future deep-sea mining successes.

2.1.1. Land-based Mining Comparison

Interest in deep-sea mining is dampened, as long as land-based mining sites meet the required needs. This influence will in the end drive the metal prices, but there are additional factors. The grades of land-based mines are continually decreasing and large amounts of overburden need to be removed to obtain these resources. Nodules for example, are lying on the seabed and are therefore easily accessible once the extreme depth has been overcome. Besides the removal of overburden to reach the ore bodies, land-based mines are resulting into deep open-pit and mega-underground mines. The result is a massive footprint consisting out of violated habitats, roads, buildings, complexes, open-pits and waste rock (overburden). Compared to this, the impact of deep-sea-mining can be considered as less extreme.

2.2. Marine Mineral Resources

The term marine mineral resource generally defines those resources which can be found in the marine environment. A mineral on its own can be defined in various manners [24], but within this context we focus on the resource as explained by the mineral economist. It refers to a commercially traded commodity derived from a naturally occurring, nonliving, organic or inorganic, solid, liquid or gaseous substance originated in the marine environment. Marine mineral recources are generally subdivided into three categories; fuels, non-metallic and metallic. The wide variety and occurrence in metallic marine mineral resources can again

be subdivided into three governing types; manganese nodules, manganese crusts and seafloor massive sulphides.

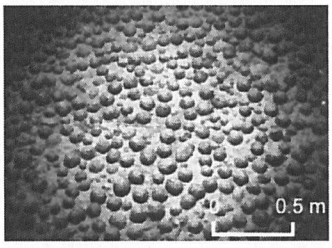

Figure 2.1: Manganese nodules

Figure 2.2: Manganese crusts

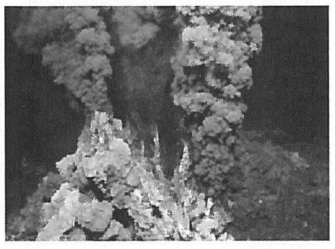

Figure 2.3: Seafloor massive sulphides

Locations of interest are concentrated in specific areas of the oceans. The polymetallic nodules and crusts are located within typical zones, like the Clarion-Clipperton Zone, Peru Basin, Indian Ocean and Cook Islands. The location of the sulphides is strongly related to boundaries of tectonic plates and so-called hydrothermal vents (black smokers). A global overview of these locations is given in Figure 2.4. In Section 2.2.1 till 2.2.3 a brief description of each marine mineral resource is given. For further reading [24], [13] or [34] can be consulted. For recent studies the International Seabed Authority (ISA) can be addressed.

2.2.1. Polymetallic Nodules

When speaking about marine mineral resources, polymetallic nodules were the ones first discovered (Figure 2.1). This type of resource offers vast amounts on the seafloor which are relatively easy recoverable compared to other mineral resources. The nodules are found on the abyssal planes of most oceans on our planet and cover globally around 46 million km^2. The nodules can best be described as potato shaped rock concretions formed of concentric layers of iron and manganese hydroxides around a core [5]. Origin and formation of the nodules is still sort of a mystery, most likely a diagenetic process which is sediment related and a hydrogenous process which is seawater and current related [1] . Its main components are: manganese (29%), iron(6%), aluminium (3%). Widely known are the nodules for the content of nickel and cobalt, which exceed the global estimated land-based resources of these elements in terms of reserve [13].

The abundance of the nodules is strongly correlated with the area examined. Some places have a coverage of 70% of the ocean floor, resulting in amounts exceeding 15 kg/m^2. The highest concentration of seafloor coverage is at locations with a water depth between 4000 m and 6000 m [7]. Most extensive deposits are known to be located in the Pacific Ocean.
The total amount of nodules on the seafloor known to men is purely based on estimation, whereas most of the ocean floor hasn't been explored yet and resources therefore not discovered. The first estimations are of John Mero, which estimated the total amount around 1.5 trillion tons. A more recent estimation of 500 billion tons [1] was made by Alan A. Archer of the US Geological Institute.

The vicinity of deep-sea minerals is most of the time strongly related to the presence of tectonic and volcanic activities. Abundance of nodules however, is spread over specific areas. Locations of interest are related to commercial feasibility expressed in recoverable amounts in tons per square-meter. The locations known in this stage are the Clarion-Clipperton Zone, the Peru Basin, Cook Islands and the Indian Ocean as shown in Figure 2.4. As mentioned, discoveries depend on exploration and not every square-meter of the ocean has been explored yet. Worth a note is that recently a discovery of a large field in the vicinity of Barbados (Golf of Mexico) has been done (Research Vessel Sonne, 2015) [10]. Who knows what the Atlantic Ocean still has to offer. More detailed information regarding the nodule properties can be found in Appendix A.

2.2.2. Manganese Crusts

This cobalt-rich type of marine mineral resource (Figure 2.2) is known as a sort of coating on marine rock and oceanfloor sediment (unconsolidated sediment). The rock-hard metallic layer is mainly formed on flanks of submarine volcanos, called seamounts. Crusts mainly contain copper, manganese and nickel. In general, the crusts grow slower than manganese nodules. The thickness of the crusts varies between $0.02m$ and $0.26m$. The layer is firmly attached to the rocks and bottom and can therefore not easily be picked up and

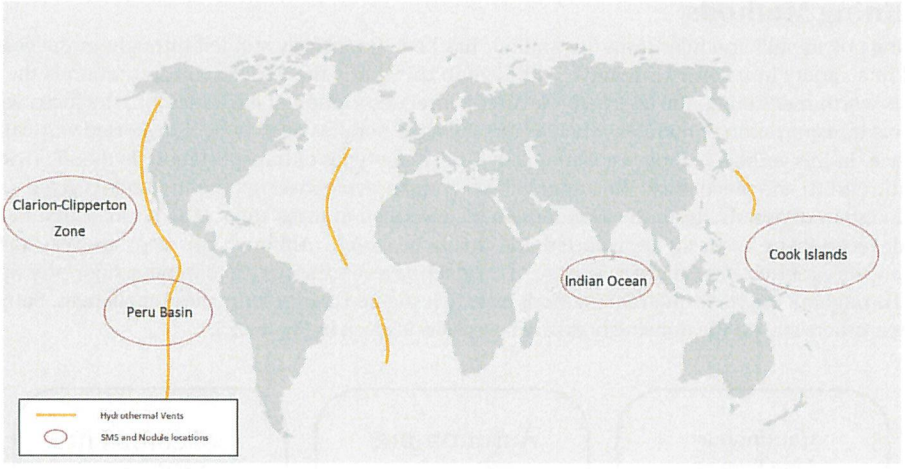

Figure 2.4: Overview global locations eligible for DSM exploitation

collected like the polymetallic nodules. As a result of this fixation, the crusts need to be cutted or scraped loose before collection can take place. The crusts originate as a result of precipitation of hydrogenetic bottom waters and are typically found in water depths between 400-7000m. The thickest and most metal-rich crusts are concentrated in water depths between 1500-2500m. Presence of the crusts depends on seamounts and sediment-free ridges, therefore the highest presence of crusts is found in the Pacific Ocean. A particular location of interest within the Pacific Ocean is the Prime Crust Zone, located in the western part of the Pacific Ocean. Physical characteristics are a high porosity (60%) and high specific-surface area (325 gr/m^2).

2.2.3. Seafloor Massive Sulphides

The polymetallic sulphides or seafloor massive sulphides (Figure 2.3), can be considered as a recently discovered resource compared to the discovery of other metallic mineral resources. The sulphides, often abbreviated as SMS, are bodies of metallic sulphides precipitated at and near the seafloor when submarine volcanic hot-springs (hydrothermal vents) fluids mix with cold seawater. The origin of these type of resources is related to hydrothermal mineralisation from flows out of black smokers. Location of black smokers and sulphide containing resources are found at plate boundaries of mid oceanic ridges. This type of mineral resource mainly consists out of sulphur compounds as its name already indicates. The hydrothermal process results into precipitation of the mineral rich flow on the ocean floor, which forms massive deposits. These deposits can be described as complex structures formed on the seafloor called chimneys.
Estimations of tonnages of this type of resource throughout the global ocean are little known, and therefore comparison with similar land-based materials has a high rate of uncertainty. The tonnages are roughly estimated around a few hundred million tonnes. Although the uncertainty in the amount is high, interest is nevertheless present, whereas seafloor massive sulphides contain large amounts of precious metals like copper, zinc, gold and silver [8].

2.3. Mining Methods

Recovering polymetallic nodules from the seafloor has been intensively studied throughout the years. This resulted in a variety in recovery methods. Although in this thesis the vertical transportation is the general topic, it is worth mentioning the alternatives. After a brief description of each method, the focus will be on the vertical transportation of nodules, whereas the collected nodules need to be transported vertically to the sea-surface. In this vertical regime, we distinguish three main types of transportation; hydraulic (with riser), pneumatic (airlift) and mechanical (hoisting). A brief comparison between these methods is given.
The exploitation of nodules from the seafloor can be described in three steps. The nodules first need to be collected, secondly be vertically transported and finally be stored. Although the steps are very basic, they contain a wide variety in challenges as a result of the deep-sea conditions (e.g. darkness, high-pressure, large depth). Throughout the years different methods were investigated to overcome these challenges. Some tested in practice, others still on the drawing board. An overview is given in Figure 2.5.

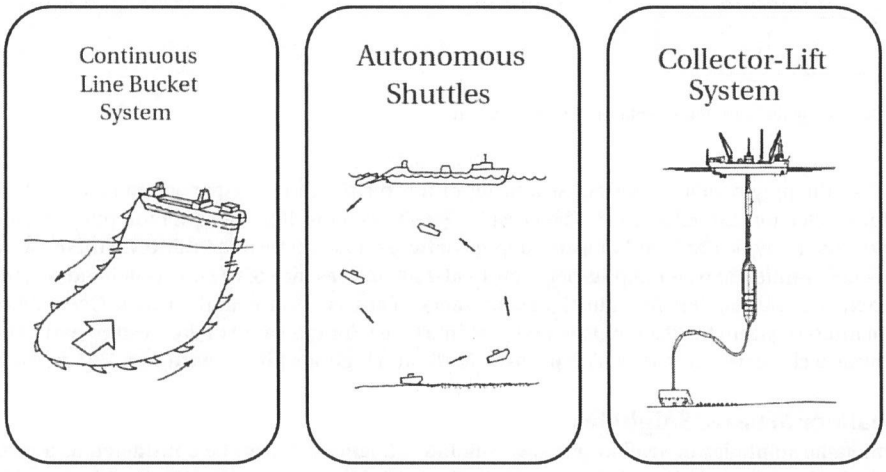

Figure 2.5: Overview different types of mining systems

2.3.1. Continuous Line Bucket System

Mining by means of a continuous line bucket system (CLB) is one of the first methods proposed and mainly investigated by Asian parties (Table 1.1). This method combines the collecting and vertical transportation in a single process. The system consists of a continuous line with buckets or skips attached. Once rotationally dragged over the seafloor, the buckets collect nodules using two vessels or even one vessel. The distance between these vessels or the length of the single vessel dictates the area being attained. Once above the sea surface, the buckets are emptied and returned to the seafloor in a continuous manner. Advantage of this method is its simplicity and minimal power consumption, especially when equipped with polypropylene rope and netted buckets. Disadvantages are:

- Lack of maneuverability
- Lack of production control (uncertain pickup efficiency)
- Entanglement (wires itself or entanglement with seafloor objects)
- Cutting power
- Heavy sediment disturbance
- Potential hazard of snapping of wire

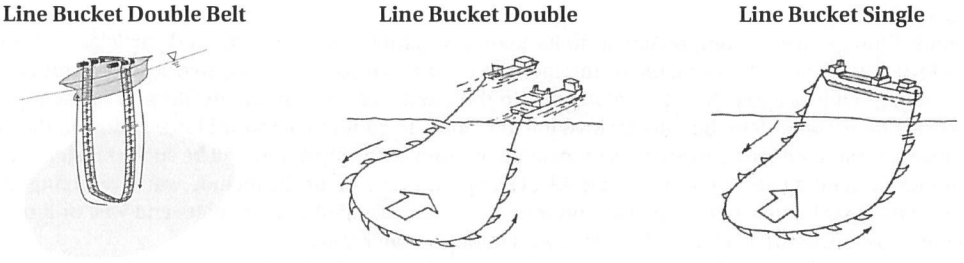

Figure 2.6: Continuous line bucket systems

The feasibility in larger water depth is a question as well, whereas all disadvantages will become more severe with increasing working depth. An alternative method to the continuous line bucket system is the two-belt continuous line bucket system. This system operates with a hanging belt which picks-up the nodules instead of dragging them into the buckets. Additional challenges of this method are wire entanglement and the risk of bucket collision.

2.3.2. Autonomous Shuttles

The autonomous shuttles can be regarded as a combined collector and transporter. The shuttle is launched from a vessel and propels itself independently towards the oceanfloor by use of ballast material. It collects nodules in its storage facility and ejects during the process an equal amount (by weight) of ballast material [4]. When it reaches its maximum storage capacity, it propels back to the surface where the collected resources are loaded into the PSSV (Moreau, 1984; Marchal, 1984; Lenoble 1989). Disadvantages of the method will be its high costs (especially in research and development), the energy consumption and the chance of loss of a precious shuttle. When the lowering of the shuttle is done by ballasting, an amount of certain ballast material will be present as deposit on the seafloor. This will contribute to the environmental impact.

2.3.3. Collector-Lift System

Throughout the years the collector-lift method has turned out to be the most feasible option. It has already been developed and tested during the seventies. As mentioned, the method of lifting can be roughly divided into three categories; mechanical, pneumatic and hydraulic. All different methods share the same goal, to transport the nodules to the sea surface. The general system consists of a production support vessel, a lifting mechanism and a nodule collector located at the oceanfloor. A short description including pros and cons for each method is given in following sections.

Hydraulic Lifting

In hydraulic lifting, a hydraulic pump system is applied to transport the nodules from seafloor to sea surface. A nodule collector at the seafloor will collect nodules and send them to a rigid riser with pumps attached. The pumps can be either of centrifugal or rotodynamic type. To overcome the large transportation distance, several pumps (booster stations) are required along the riser to transport the slurry (nodules and fluid) towards the surface. To create flow assurance, crushing of the nodules at the seafloor might be necessary.
By application of the knowledge from riser technology out of the oil and gas industry, a reliable design is feasible. One of the major drawbacks is the fact that most of the vital components will be beneath the sea surface. Furthermore, attention is required with respect to flow assurance and unstable flow regimes.

	Advantages		Disadvantages
+	Developed riser technology	-	Vital parts underwater
+	Already successfully tested	-	Flow assurance hazards
+	Oil and gas history and experience	-	Unstable flow regimes
+	Continuous production	-	Nodule size; crushing required
		-	Riser handling
		-	Dewatering mixture
		-	Wear of pump and riser equipment
		-	Energy consumption

Pneumatic Lifting
Pneumatic lifting — use of compressed air to lift liquids or liquids together with solid particles — has been known for a long time. The principle of the method is quite simple: air is injected into the vertical riser and the rising bubbles carry the liquid along due to the interfacial friction. As air fills part of the pipe, the pressure inside becomes less than the hydrostatic; therefore an additional upward force acting on the liquid is produced. If the solid particles are present near the bottom of the pipe, they will be sucked inside the pipe as well due to the drag exercised by the liquid. The applications of air-lift include water pumping, lifting corrosive and toxic liquids, CO^2 sequestration into the ocean, lifting of coal in shafts and well drilling. The riser content consists out of a three phase flow with nodules, water and air.
Even though the principles of the air-lift method are simple, its operation is not. Lack of direct control of the liquid and solid outputs, in contrast with for example submersible liquid–solid pumps, makes stabilizing continuous operation a non-trivial task. Furthermore, there is a reduced efficiency due to the fact that high power is required to send down air to a depth of 4000 meter.

	Advantages		**Disadvantages**
+	Vital parts on deck (compressor)	-	Low efficiency
+	Less wear in pumps parts, no slurry interaction	-	High pressure results in high temperatures
+	Riser experience	-	Unstable flow regimes
+	Continuous production	-	Nodule size; crushing required
		-	Riser handling

Mechanical Lifting
In mechanical lifting the material of interest is transported vertically using containers or skips. Main part in creating the vertical motion is a hoisting winch, by means of converting mechanical power into motion. When compared with other methods, mechanical lifting turns out to be the most energy efficient method [33]. Limitations for deep-water operations may be present in the capacity of the subsea winch. Sufficient hoisting capacity still needs to be developed. Vital parts of this lifting system will be above the waterline, which makes it easily accessible in terms of maintenance and incidents.

	Advantages		**Disadvantages**
+	Energy efficient	-	Limited winch capacity for hoisting
+	Vital parts above waterline	-	Wire behavior needs investigation
+	Access during maintenance or implications	-	Wire failure and entanglement
+	No riser handling or flow assurance; simplicity	-	Control of load during hoisting
+	Environmental impact; less machinery in water	-	Discrete production

2.4. Environmental Impact

As discussed in Section 2.1, our growing high-tech society triggers a growing demand in rare-earth metals. Before a new goldrush will be unleashed, the ecologial impact needs attention. A lot of research has already been carried out under the supervision of the International Seabed Authority (ISA) and mining consortia.
The first direct impact is the physical removal of the nodules from the seafloor. Nodules can be considered as a non-sustainable seabed resource. It took several million years to create the nodules of today and the proces is one of the slowest of all geological phenomena [1]. Therefore accurate management and planning are required to control the commercial seafloor exploitation. Further impact is related to disturbance of the seabed sediment and deep-sea habitat. In order to collect the nodules, the top centimeters of seabed will be disturbed which affects the fauna. Once exploited, the processing of the nodules will result in amounts of worthless waste material mainly consisting out of sediment. This waste material can't be deposited back at the location and should be stored somewhere on land.
At this moment the impact and footprint seem to be smaller compared to land-based mining. Fact is that the role of the deep-sea in our ecosystem is still largely unknown. Recent studies show that the oceans, including the deep-sea, can be considered as CO^2 storage and stabilisators of our ecosystem [22]. In other words, with respect to future developments caution should be exercised.

3

Proposed Mining Method

As explained in Chapter 2, vertical transportation of collected nodules can be accomplished in a variety of manners. The proposed mining method in this study is vertical transportion of the nodules by means of mechanical lifting. Transportation in this manner can be considered as a method that hasn't had a lot of attention of research yet [33]. Therefore some basic insight in the system and procedure is wishful. Within this chapter the method of production is introduced, declared and some specific initial details are presented. Furthermore, the potential challenges and showstoppers are identified based on the detailed method description. Conclusively, conceivable comparable alternatives are introduced.

3.1. Method of Production

3.2. System Description

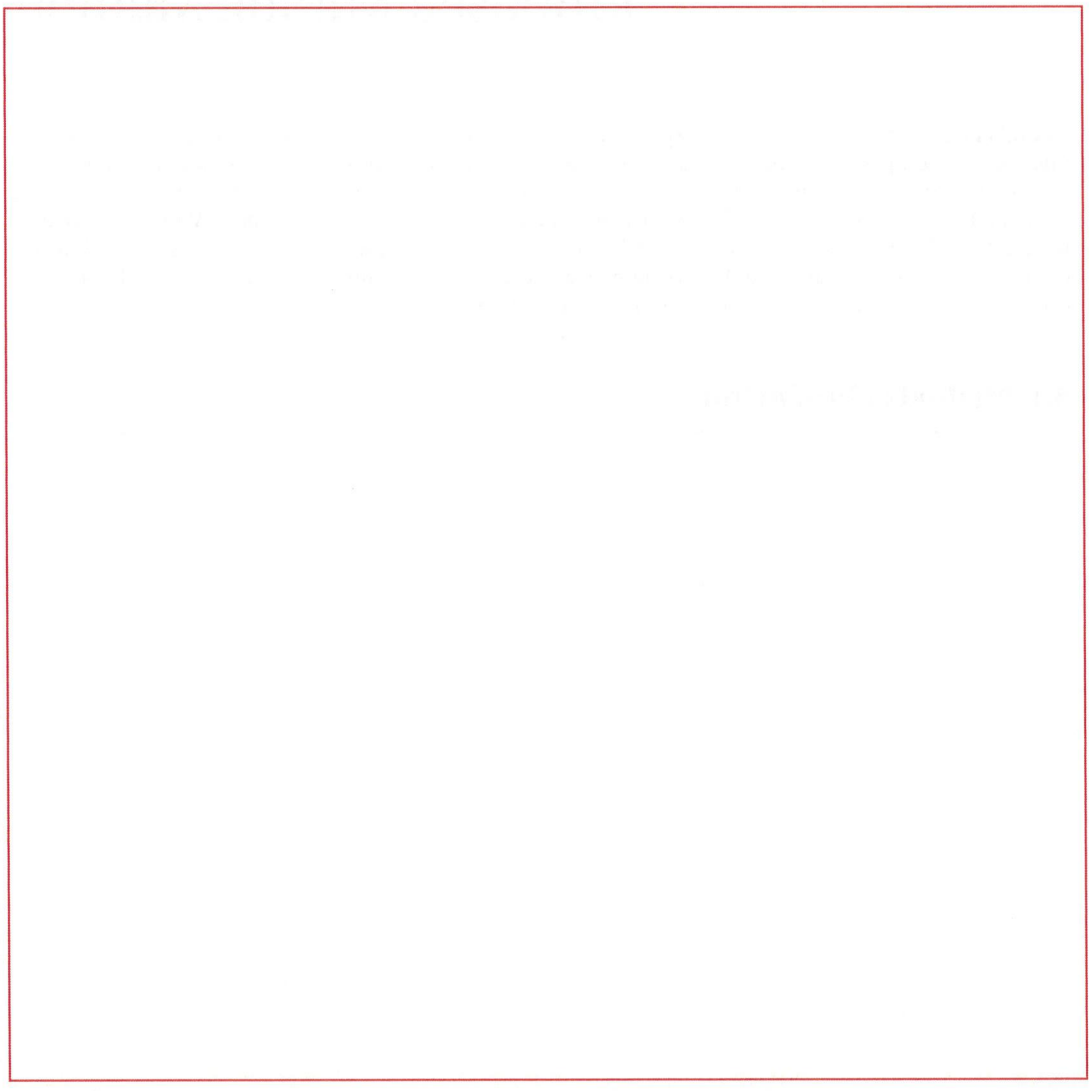

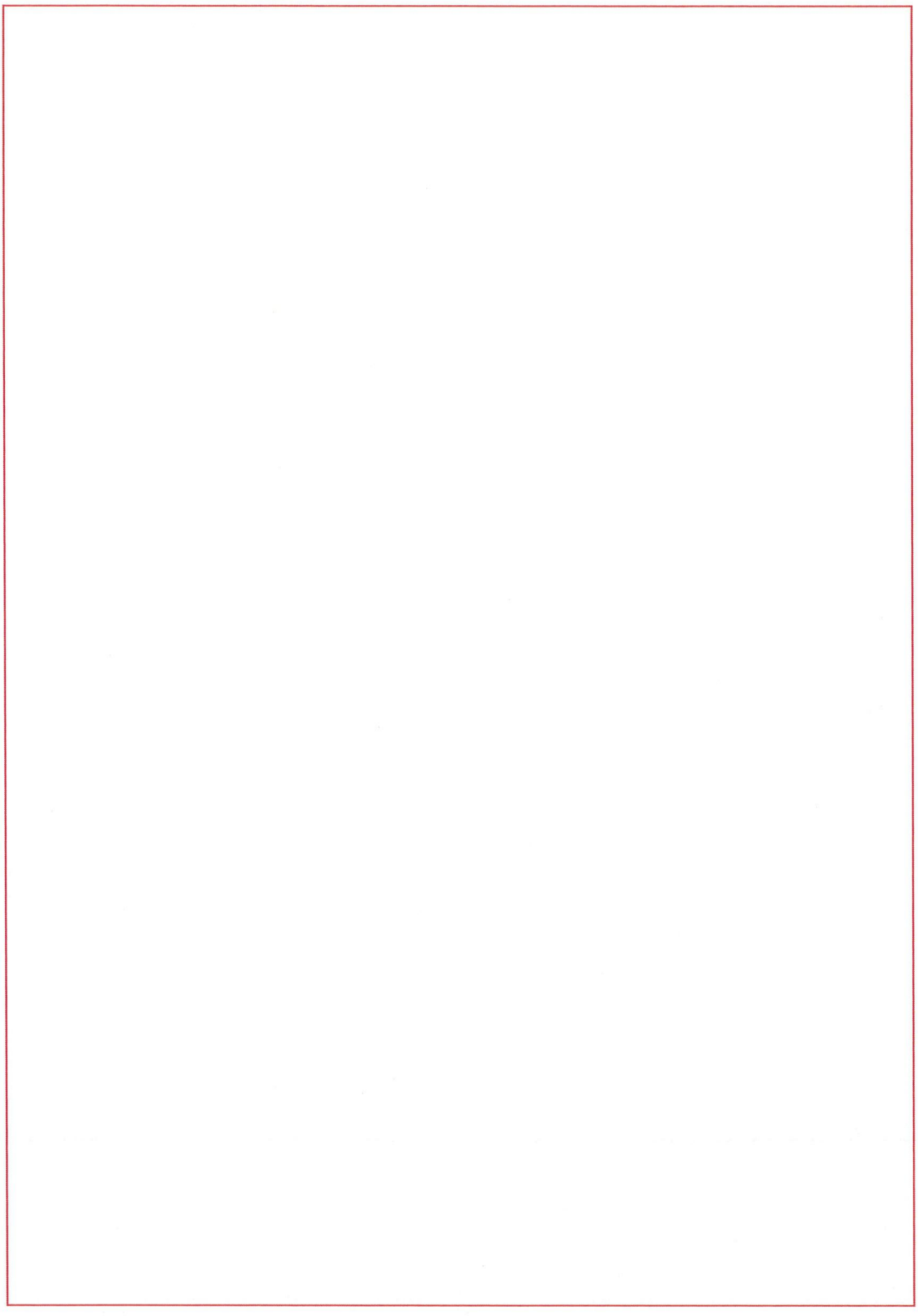

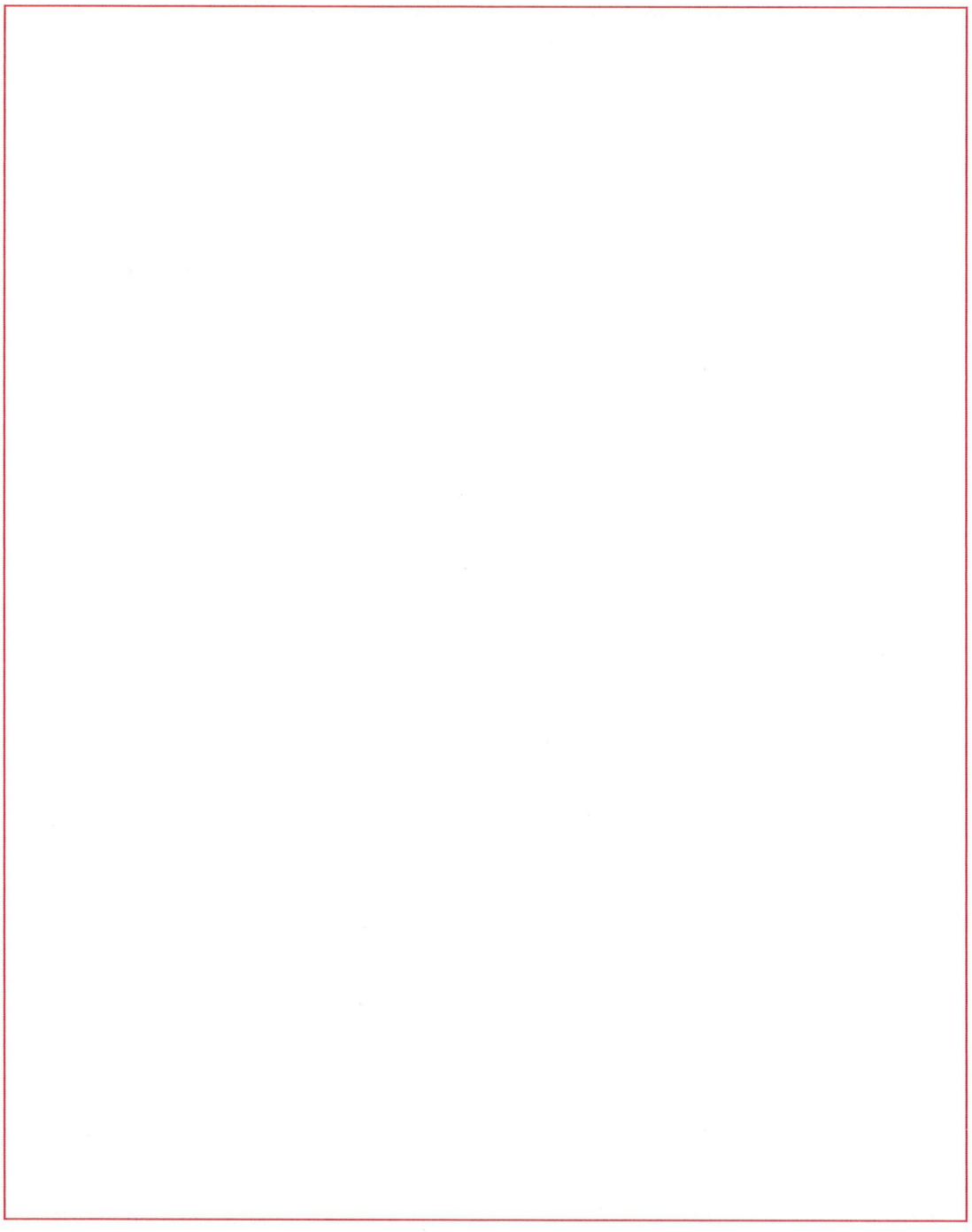

3.4. Production Cycle

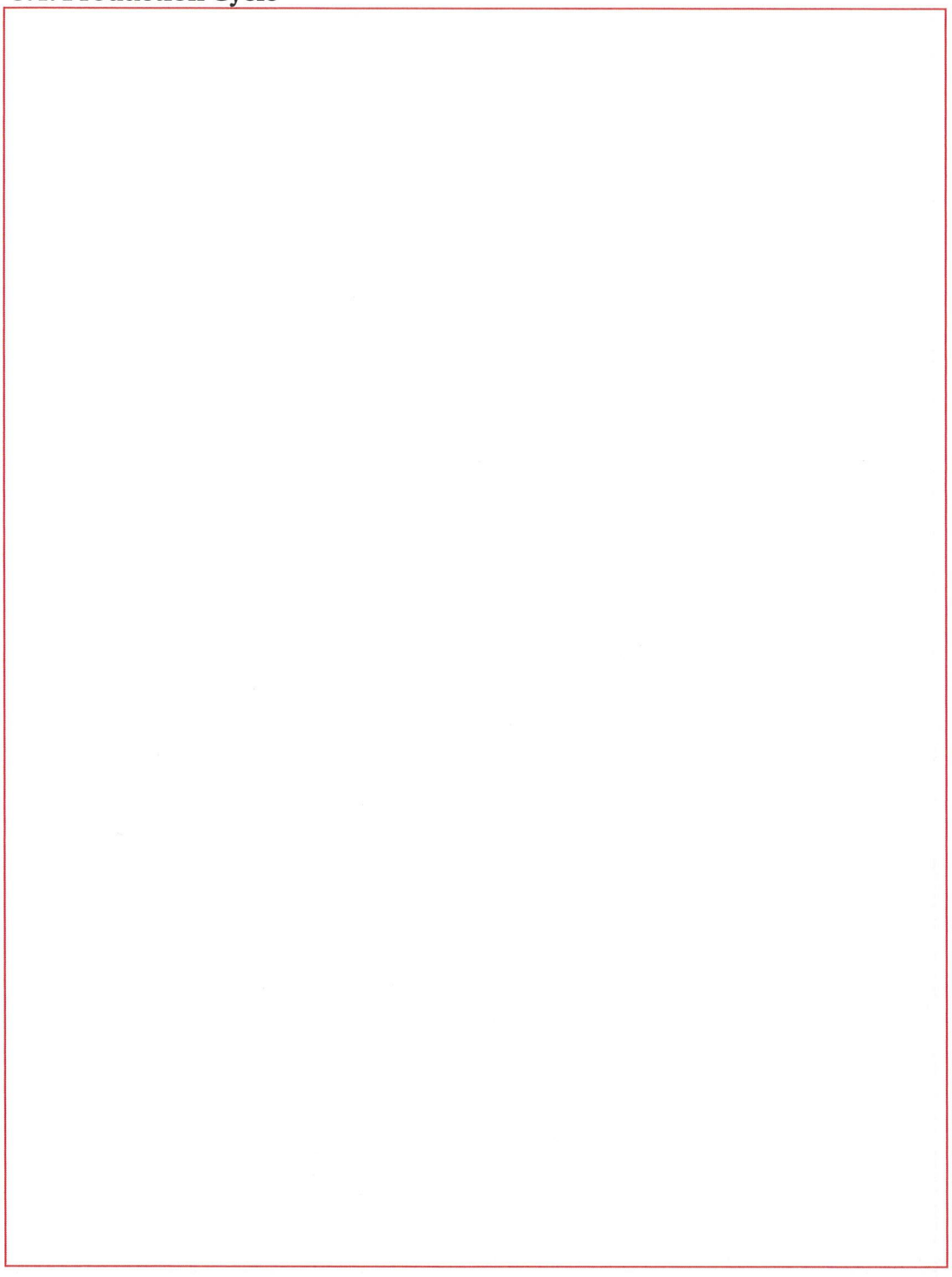

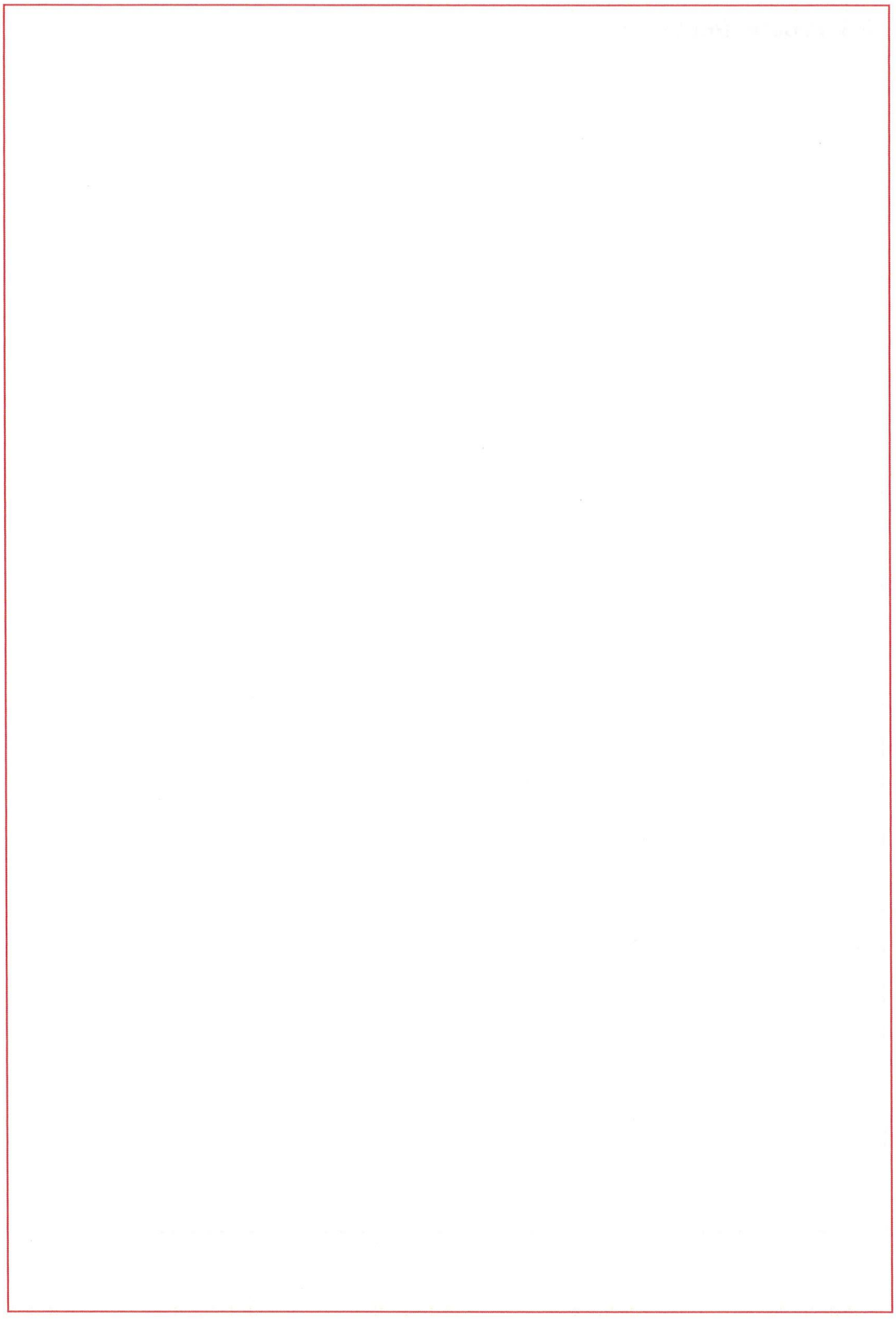

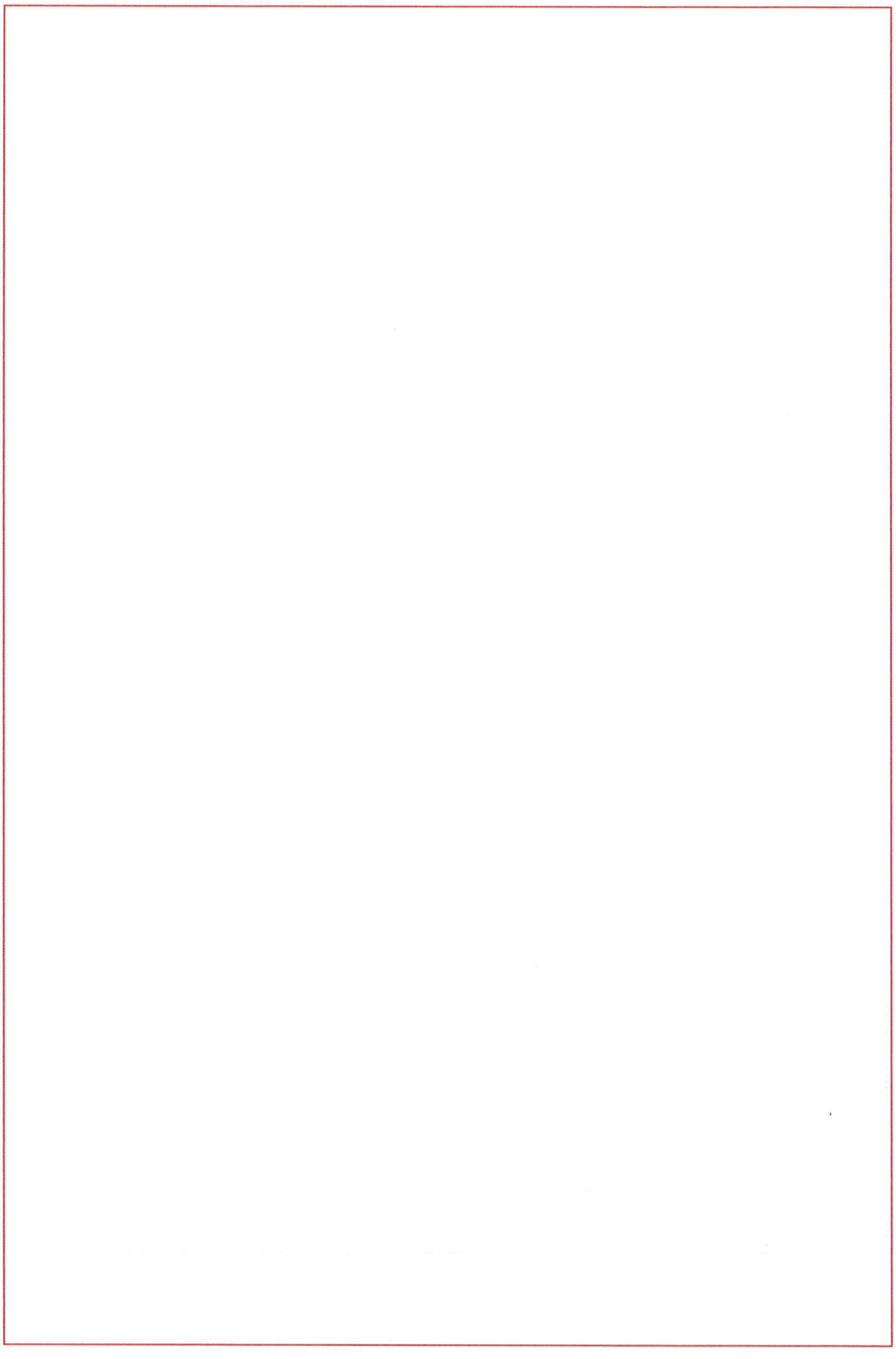

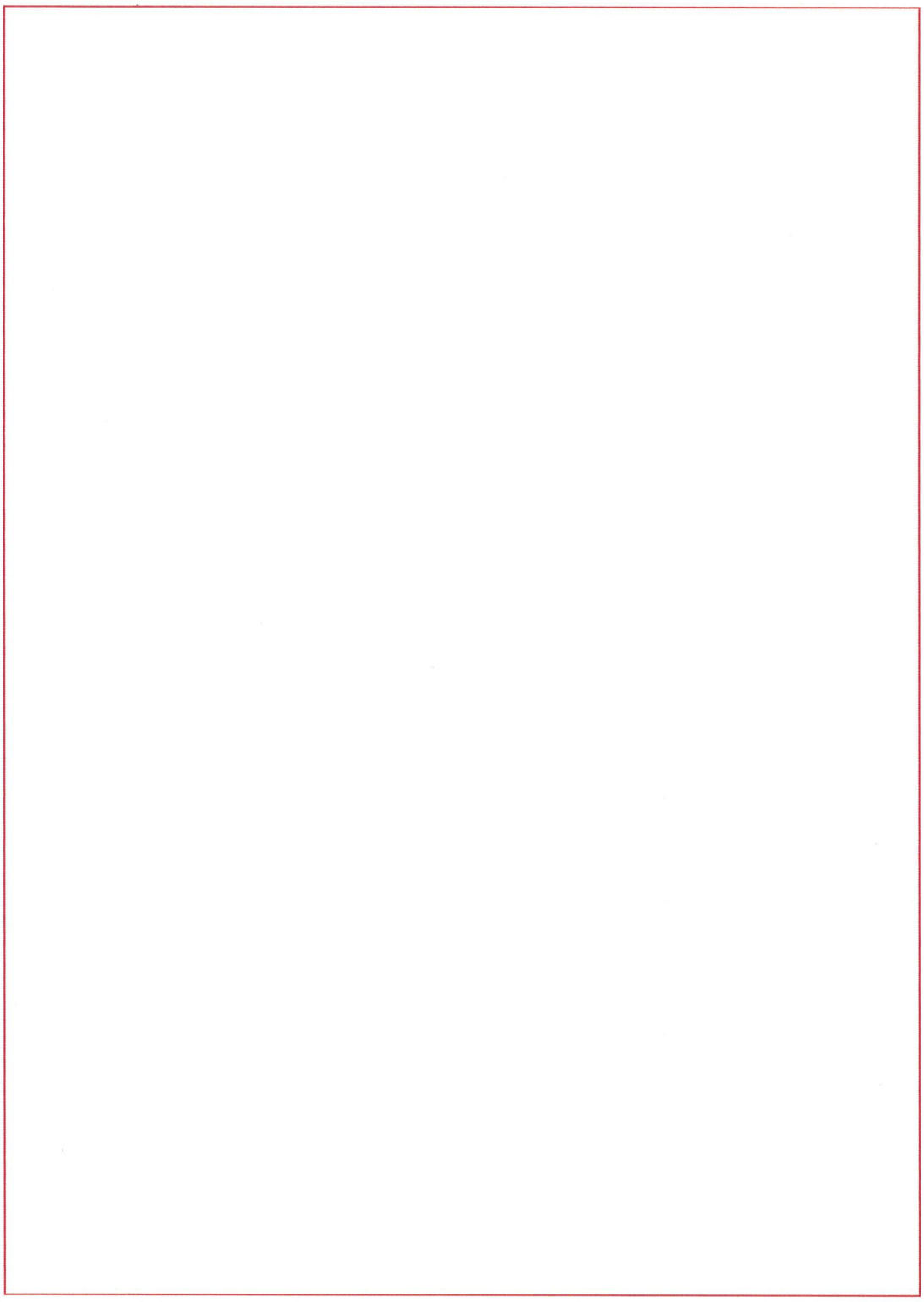

3.5. Identification of Challenges and Showstoppers

3.6. Alternatives

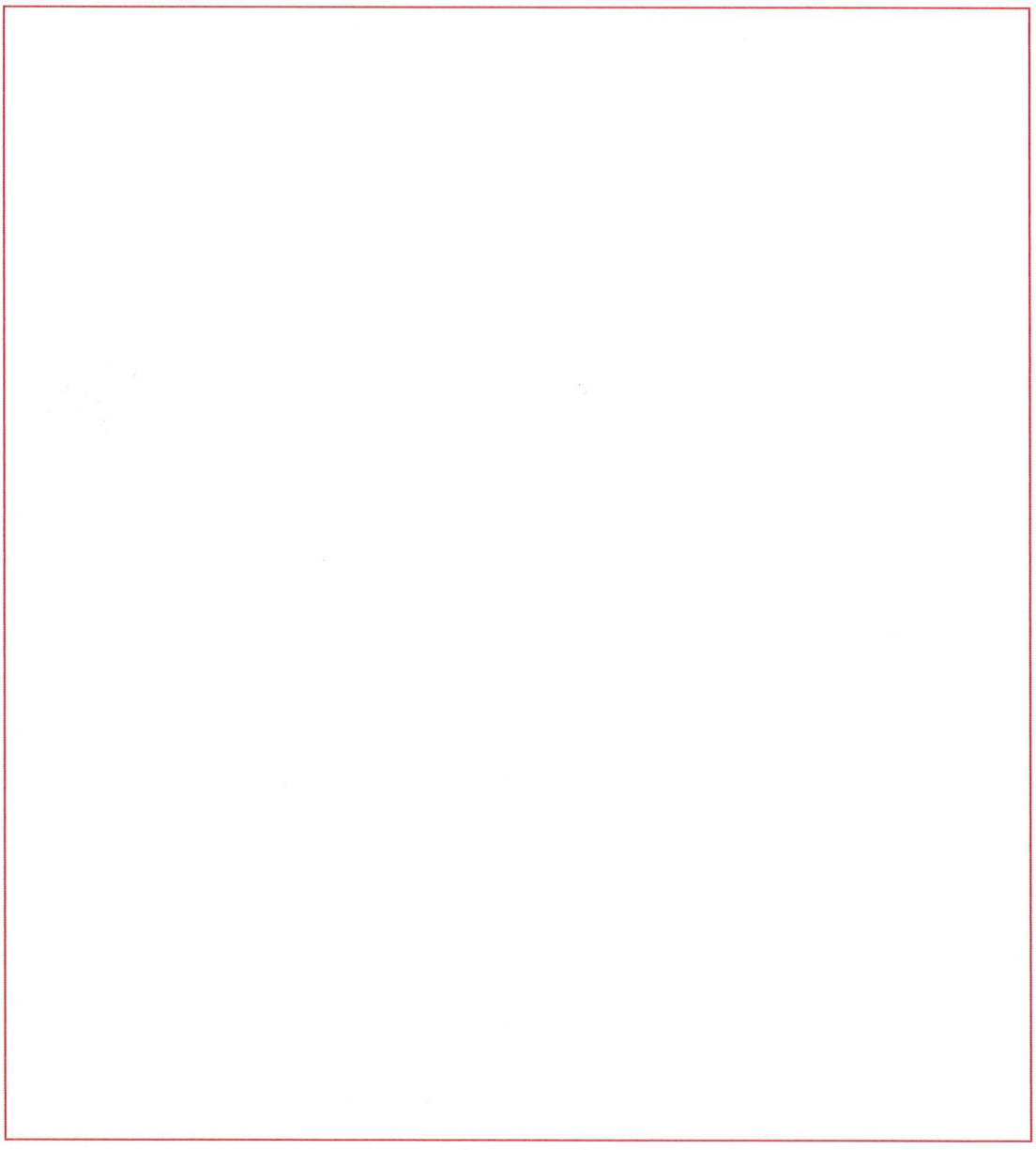

4

Location and Conditions

4.1. Location and Characteristics

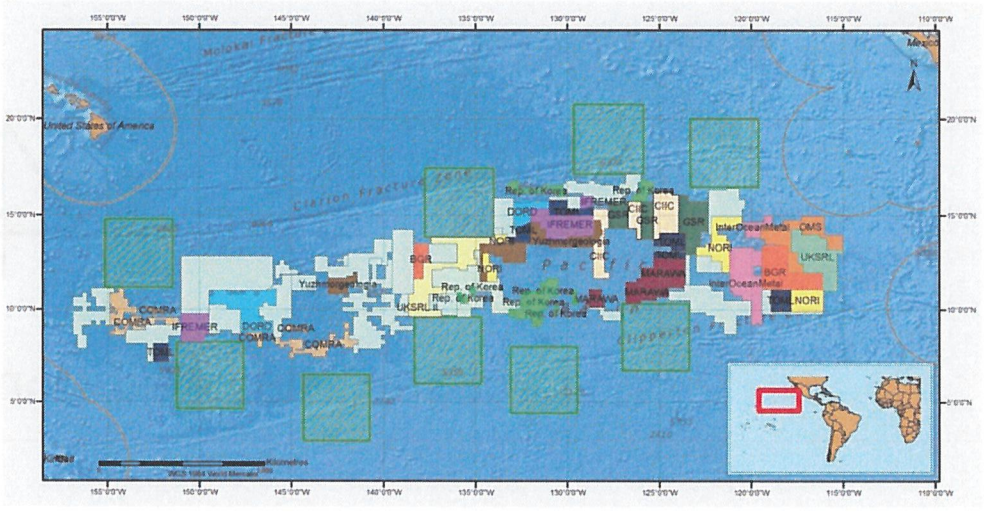

Figure 4.2: Location CCZ and license blocks

4.2. Environmental Data

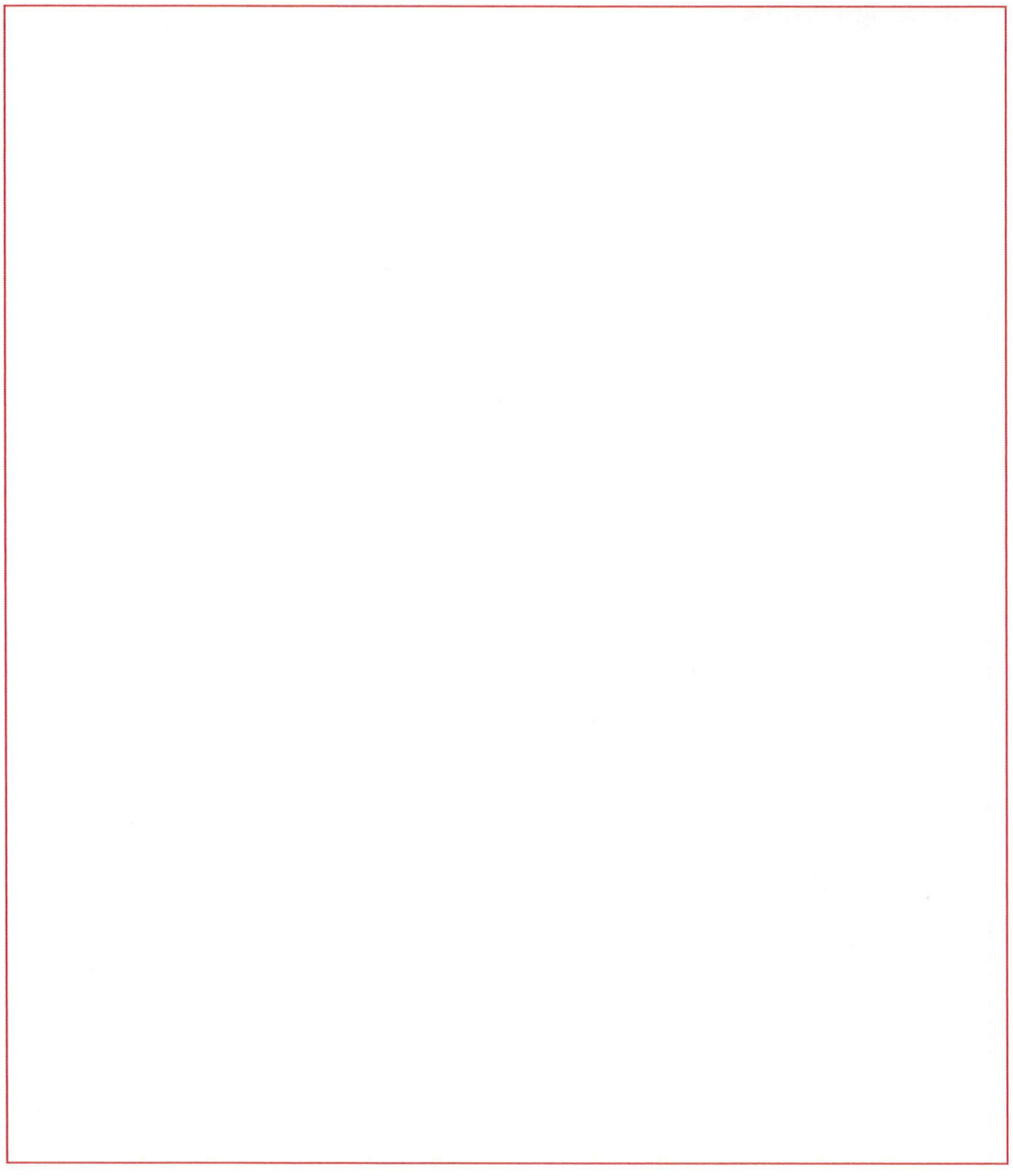

4.3. Design Profile

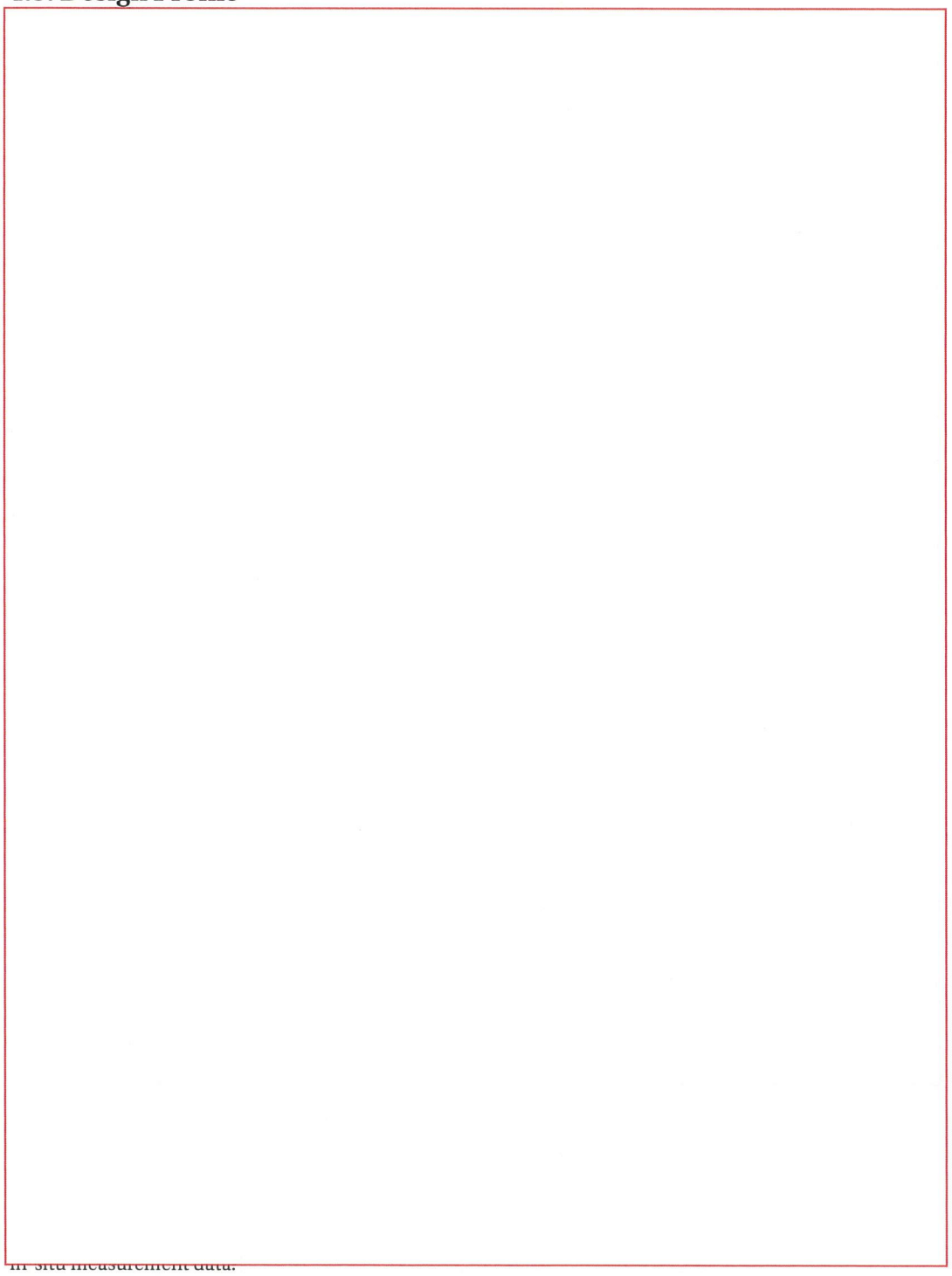

in situ measurement data.

5

Initial Setup and Loading

In order to compose an initial design of the proposed mining system, a start is made with a static study. The main goal of this chapter is to introduce a system of reference and determine initial dimensions and magnitudes of system components. These obtained results are the basis for the static and dynamic analysis in following chapters.

5.1. Coordinate and Reference System

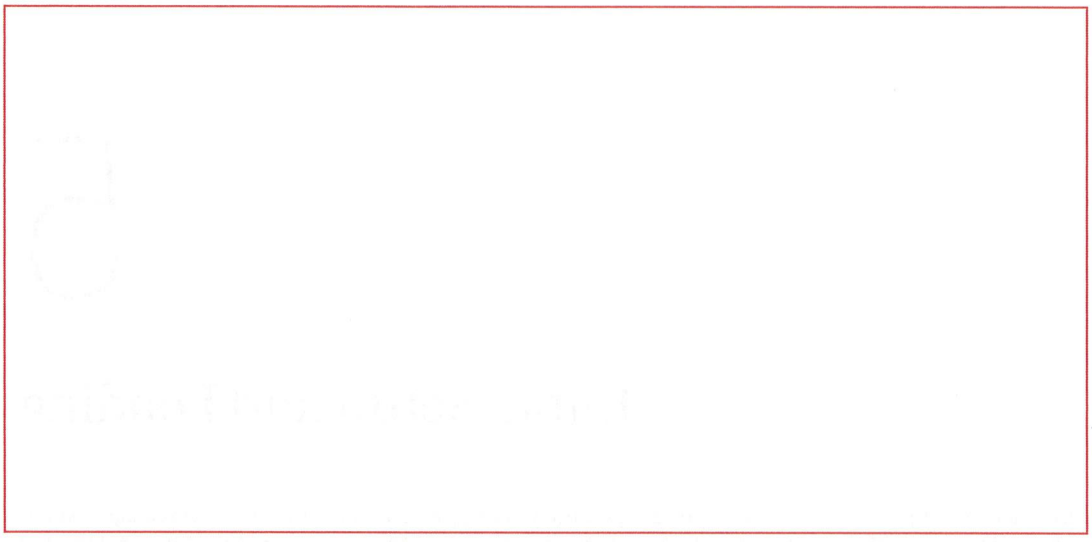

5.2. Loads and Load Combinations

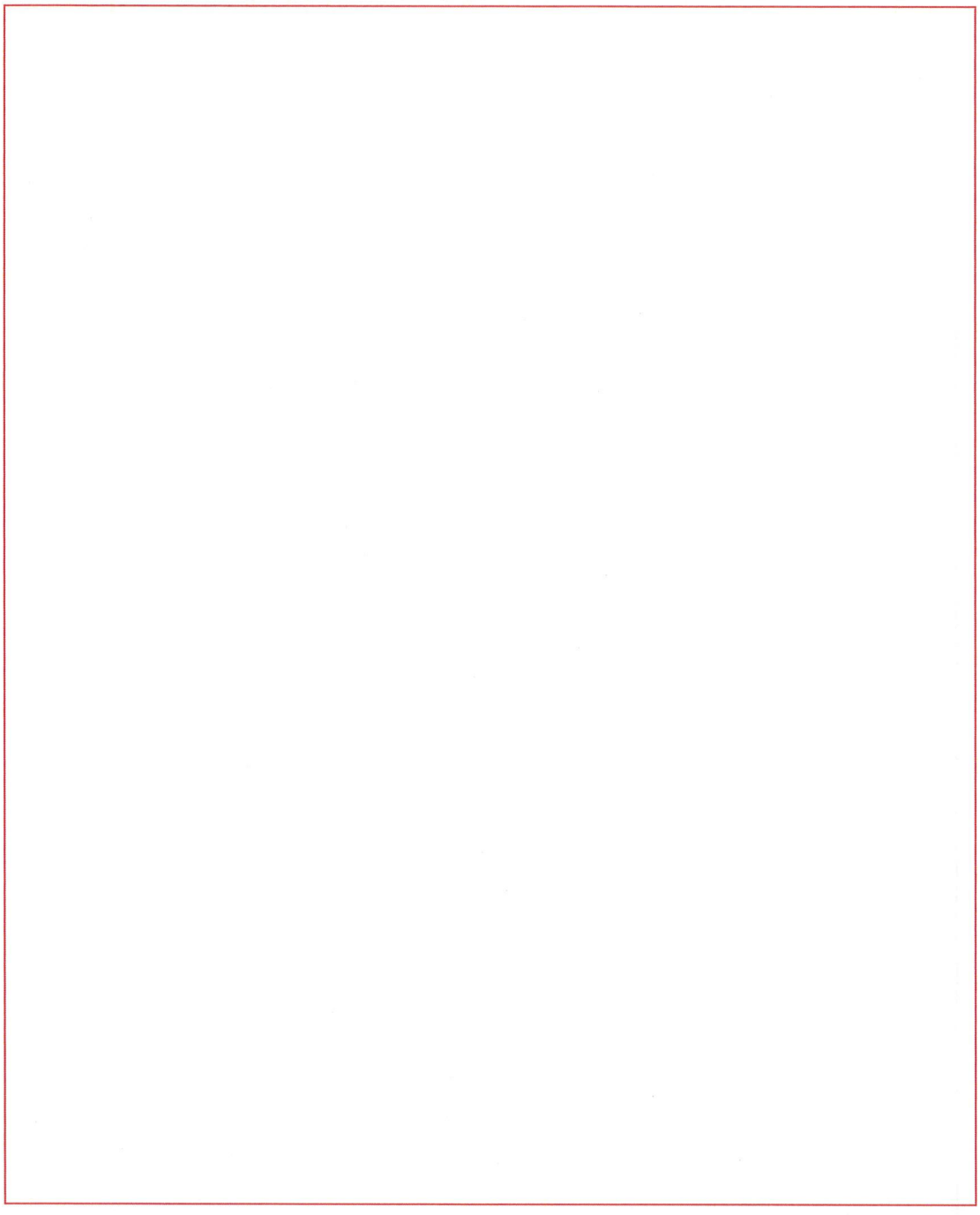

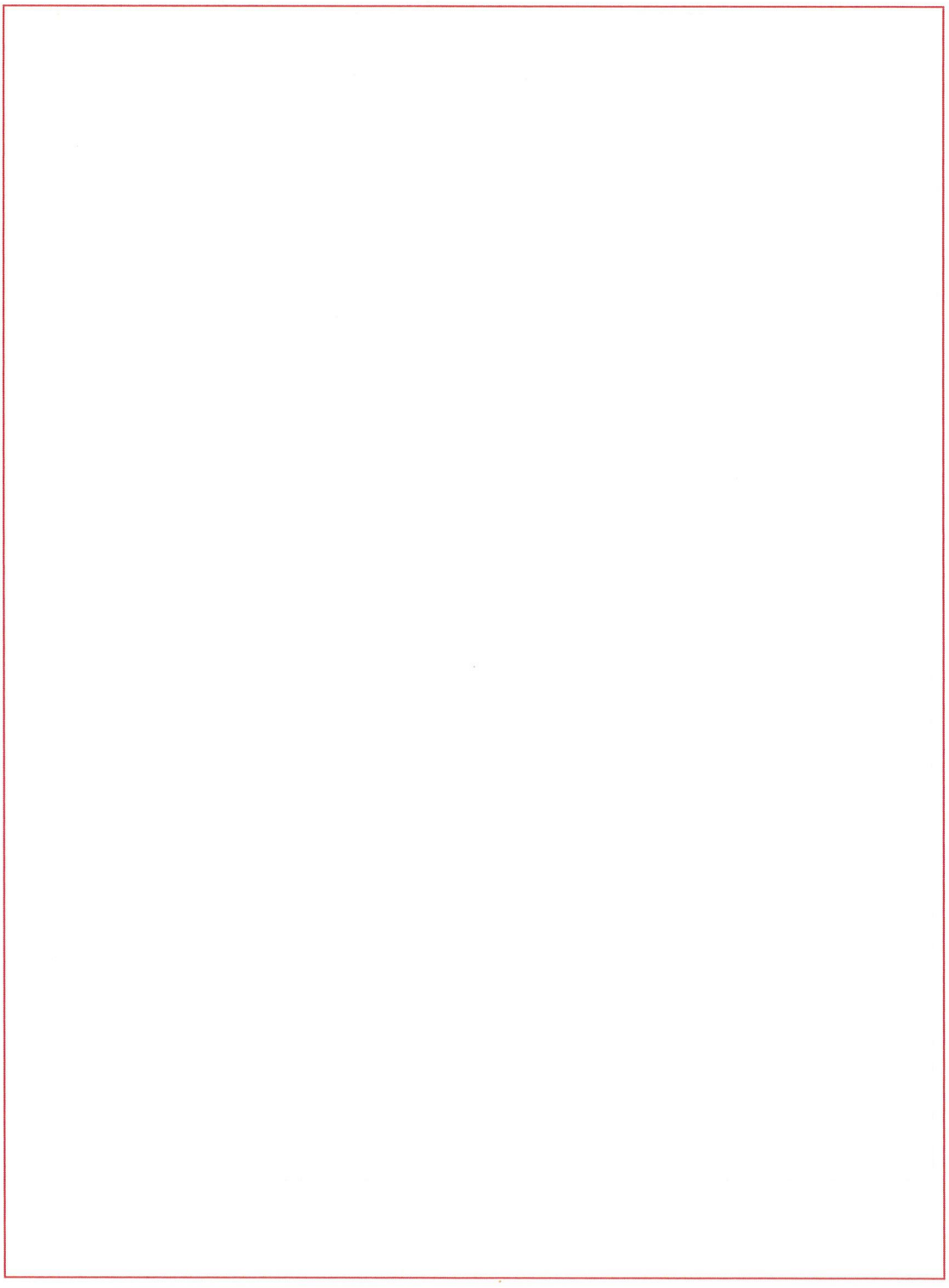

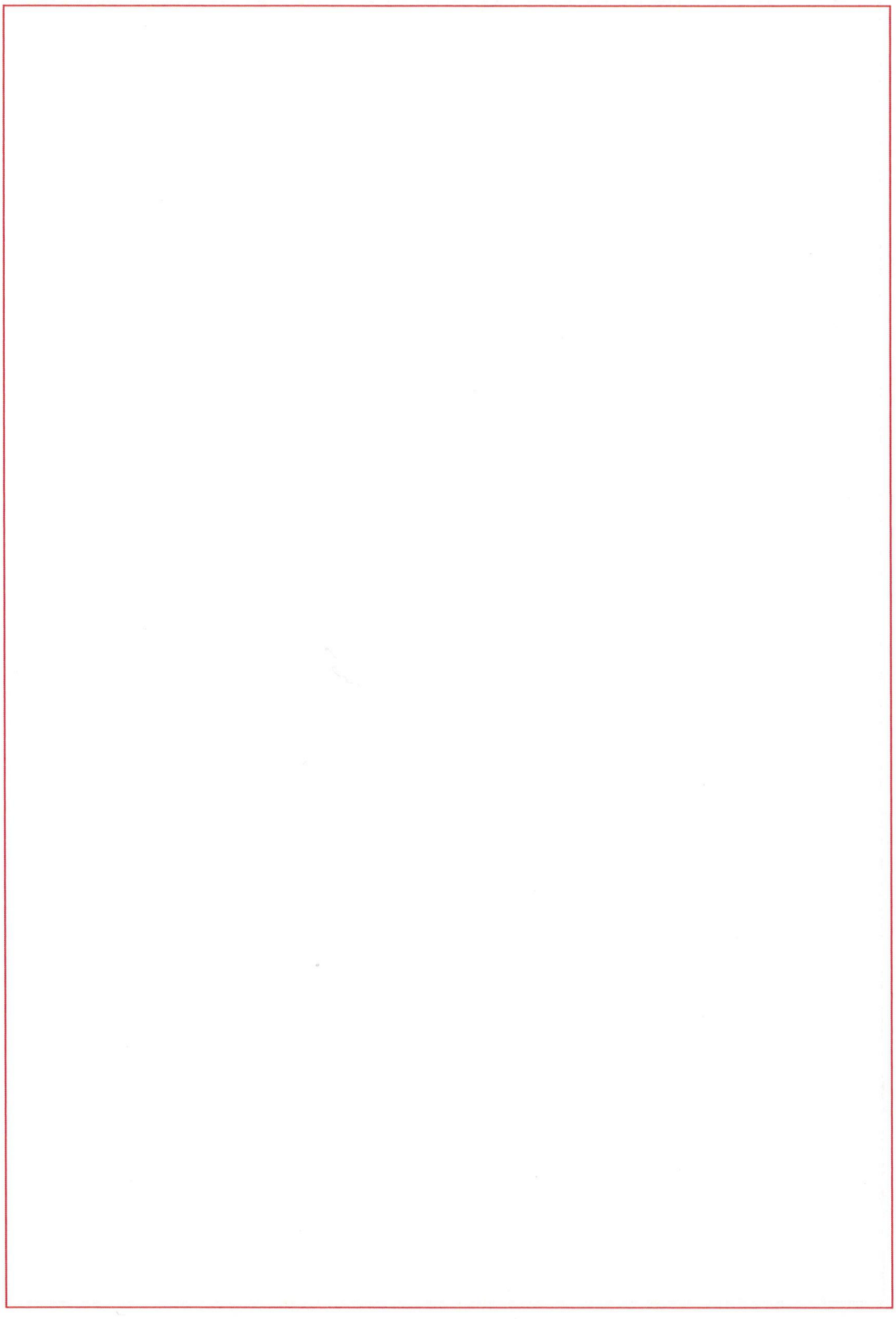

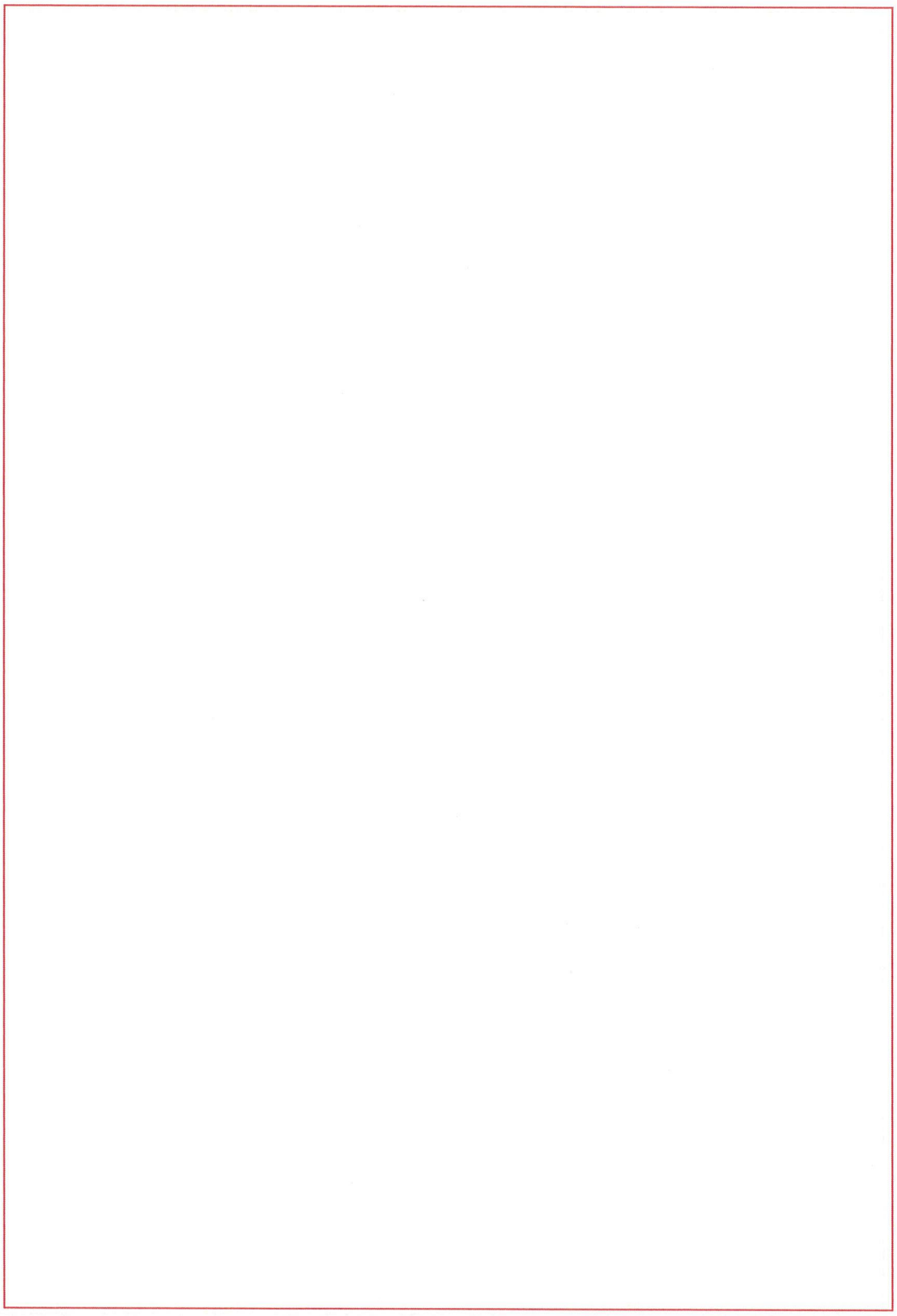

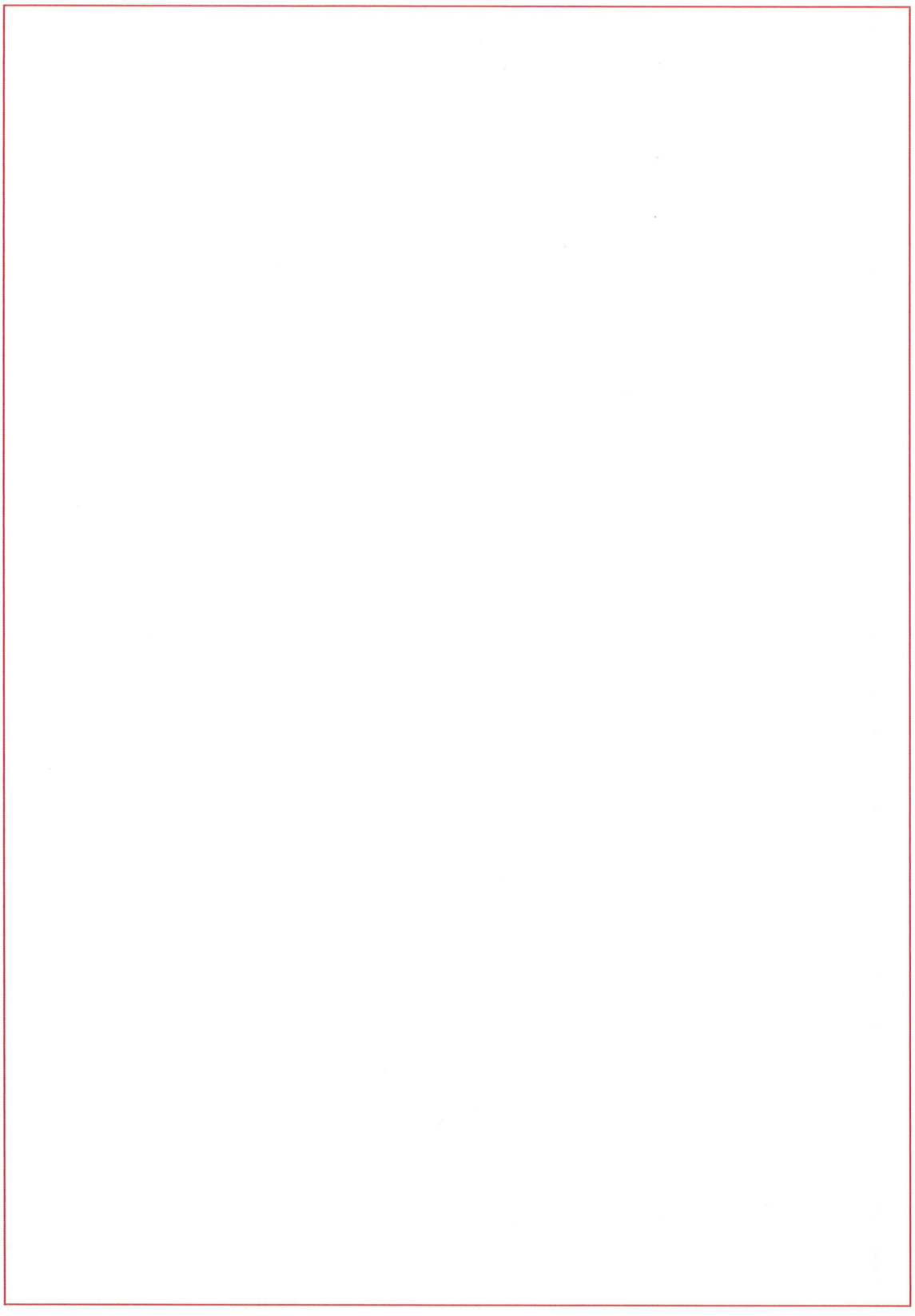

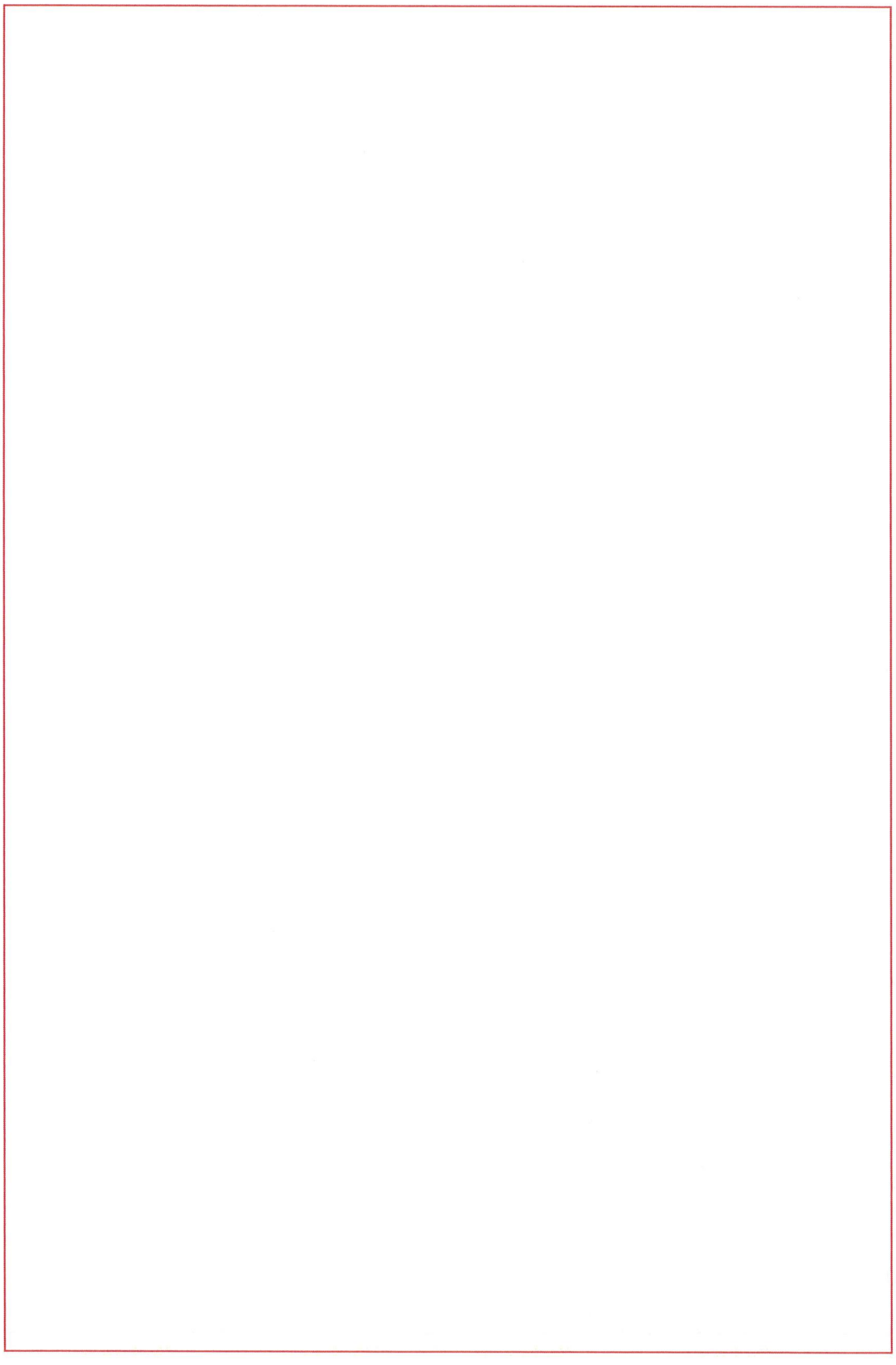

5.4. Wire Elongation

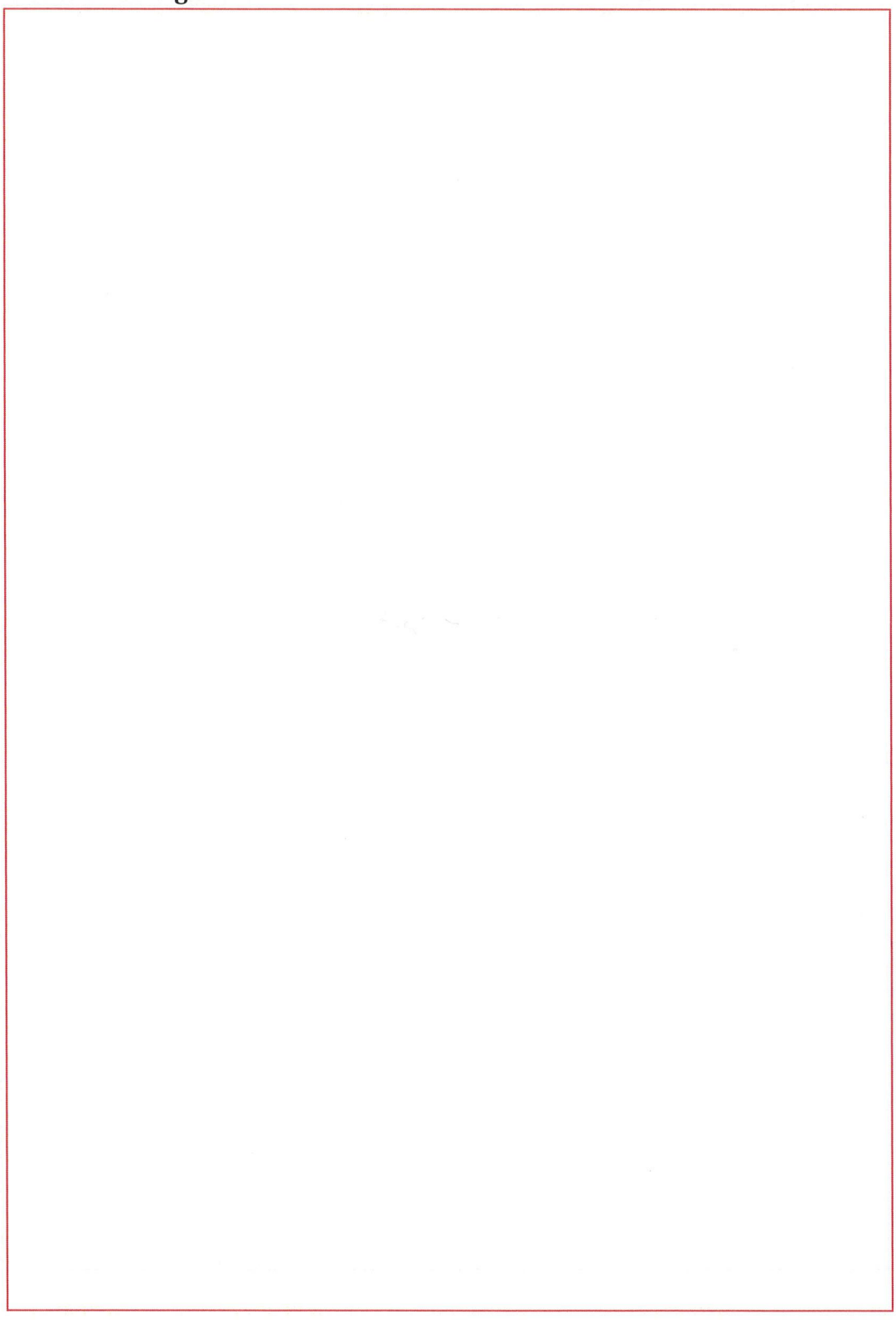

5.5. Required Lifting Power

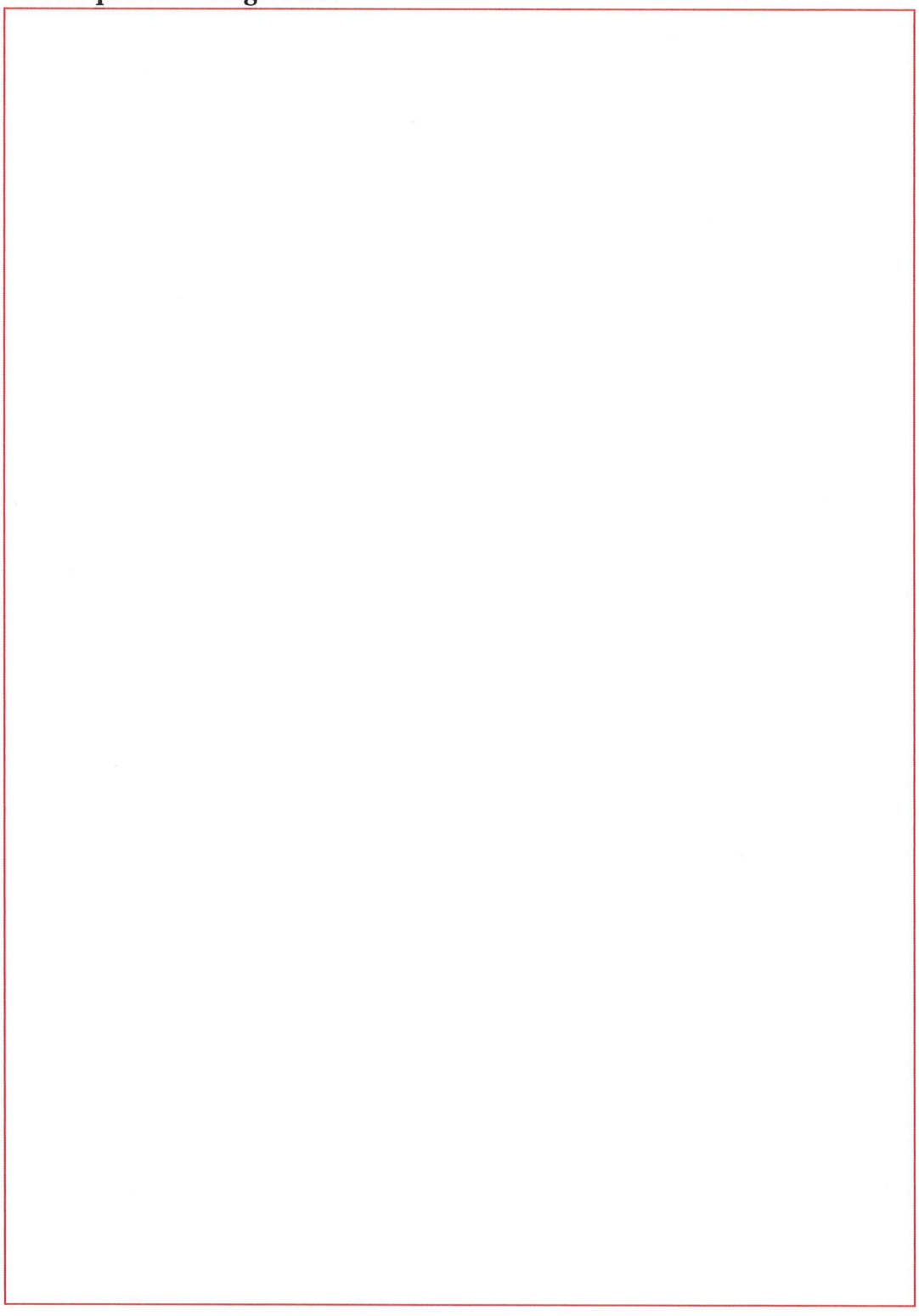

6

Static Analysis

6.1. Model Setup

In order to compute the static configuration and resulting forces, a static model is made. The model describes the natural shape of a suspended wire in a fluid flow (current profile and/or forward motion of the mining system). In this section the basis of the model is briefly explained. For a more extended explanation, Appendix D can be consulted.

6.1.1. Description

As already mentioned, the model describes the shape of a wire suspended in a flow. The flow could be a current profile or the result of the forward motion of the system. First the wire is discretized into a finite number of nodes and elements. The forces acting on the elements as result of current and forward motion is transferred in the nodes of the wire. The ratio of magnitude of the forces in horizontal and vertical direction, can be expressed as an angle by Pythagoras' theorem. The angle of the element is determined at the mid-point, i.e. taking into account both its nodes. By means of this angle, the local coordinates of the nodes can be determined. Using this approach, the geometry of the entire wire can be obtained as shown in Figure 6.1.

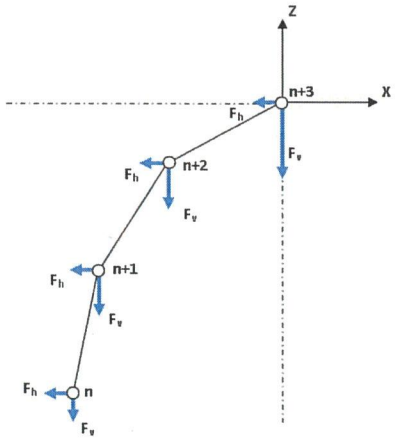

Figure 6.1: Nodes and elements

6.1.2. Parameters and Input

The forces acting on the elements of the wire determine its shape. These forces are defined by the weight of the wire and the acting drag as function of the velocity of the fluid. The common denominator here is the diameter of the wire, influencing both the weight and the drag. In this chapter a single type of wire is used; $90mm$ wire rope, with quality $1960N/mm^2$. The wire elongation plays a role in the geometry as well. The total wire elongation is calculated as the sum of the elongation per element. As the tension differs per location (due to self-weight and sheared current) the stretch per element varies as well. For more details concerning wire characteristics, Section 5.2.1 can be consulted.
As input for the velocity, the sheared current profile from Section 4.2.3 is used. On top of that a forward system motion is added.

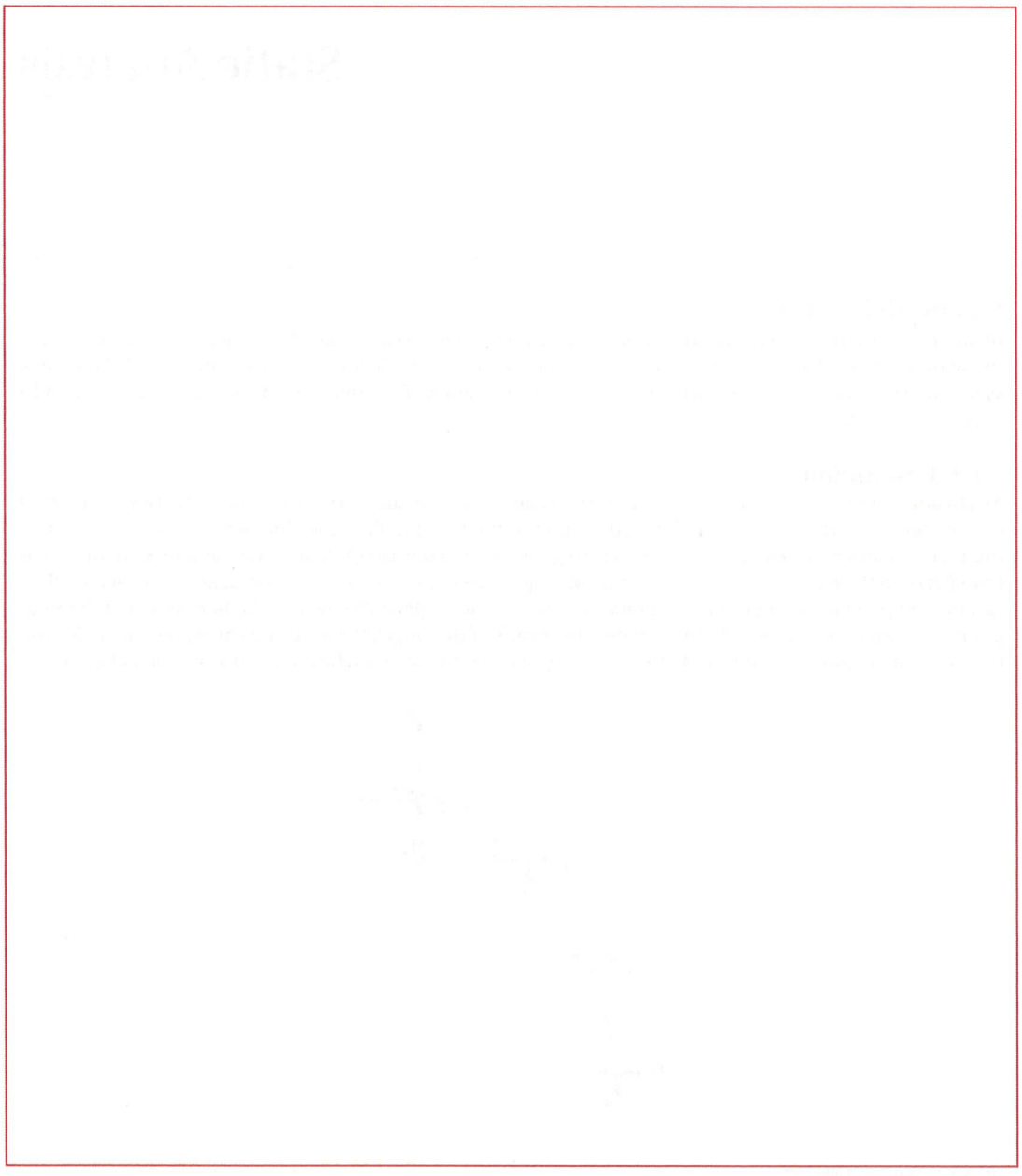

6.2. Analysis Method I - Proposed Mining Method

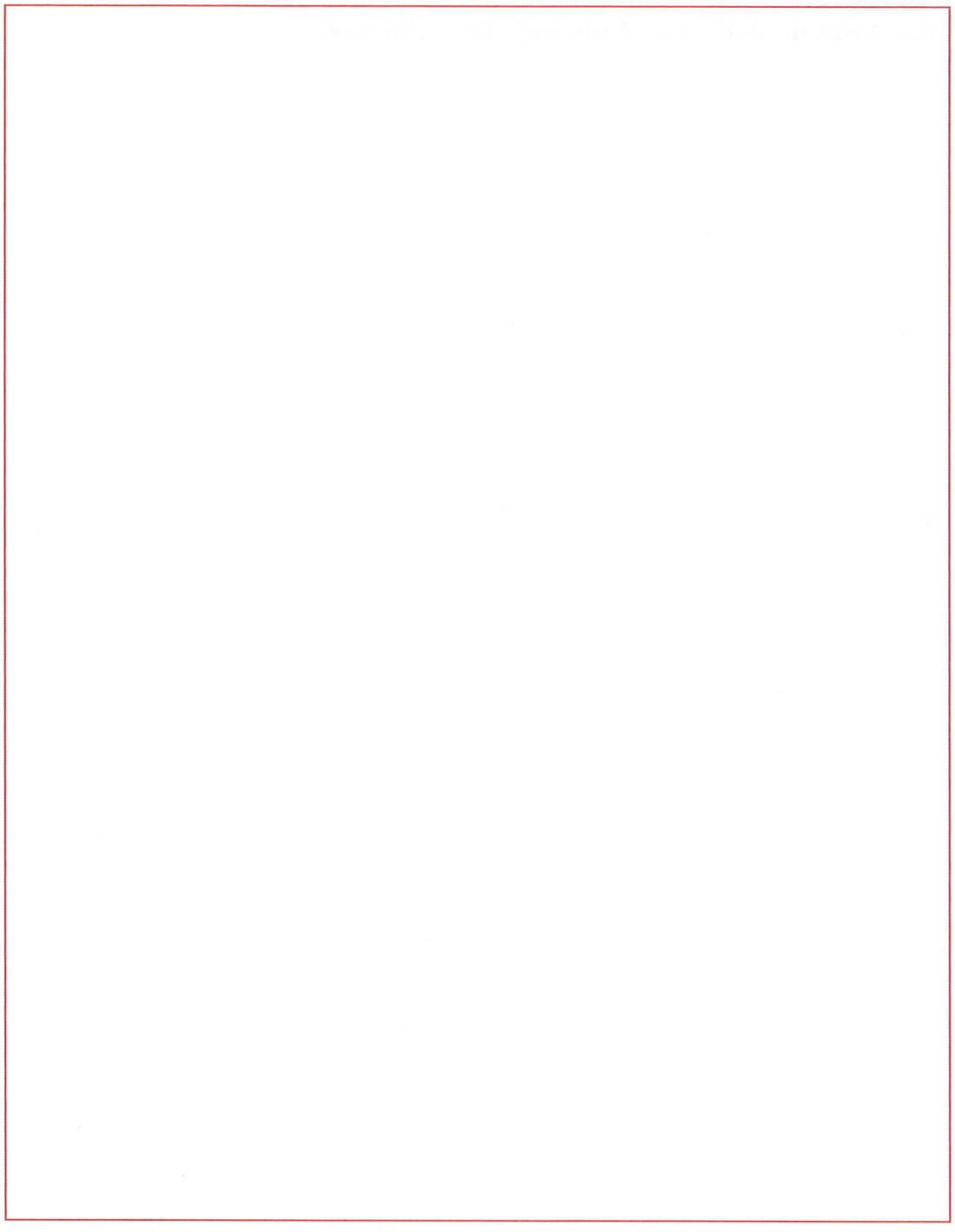

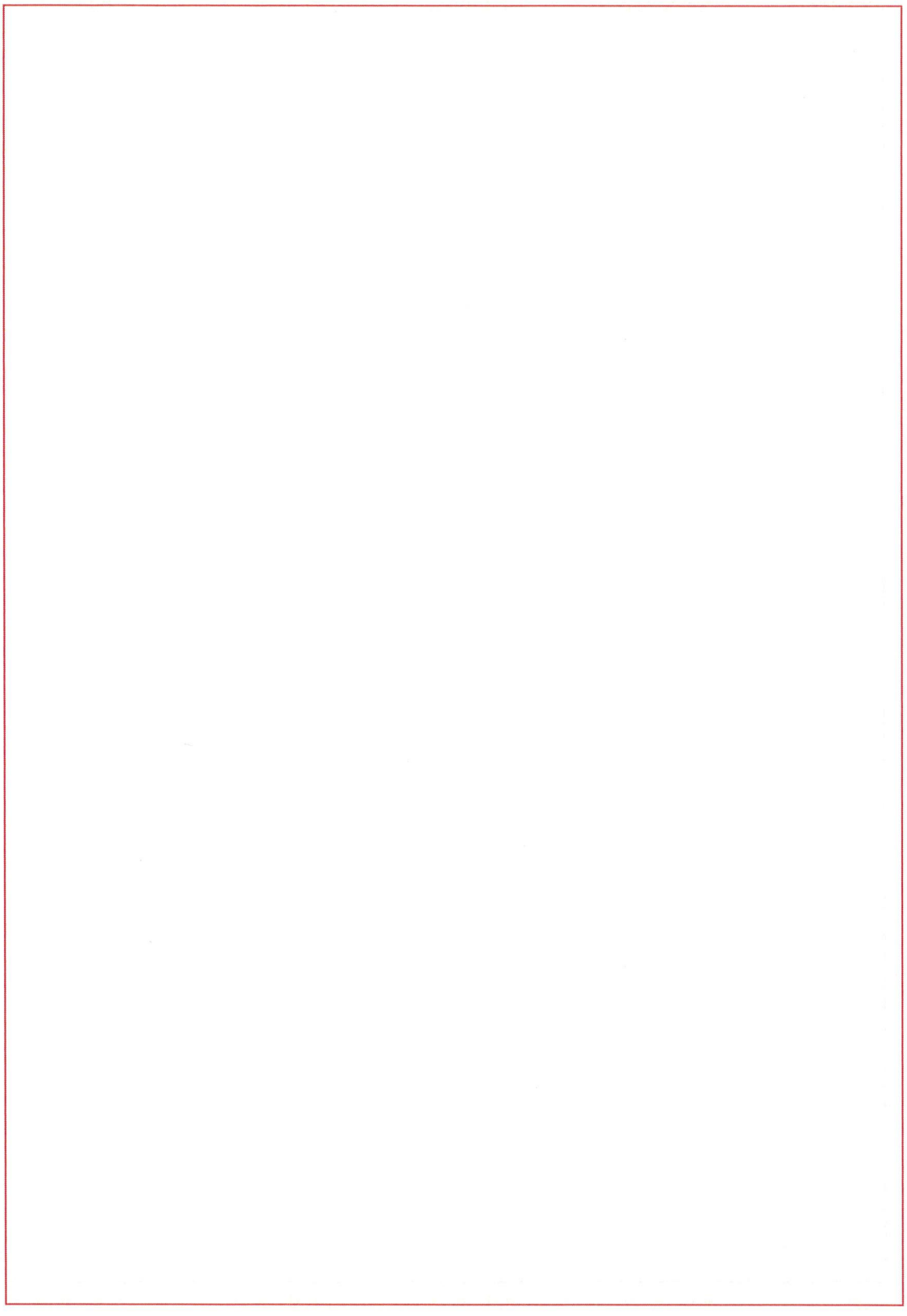

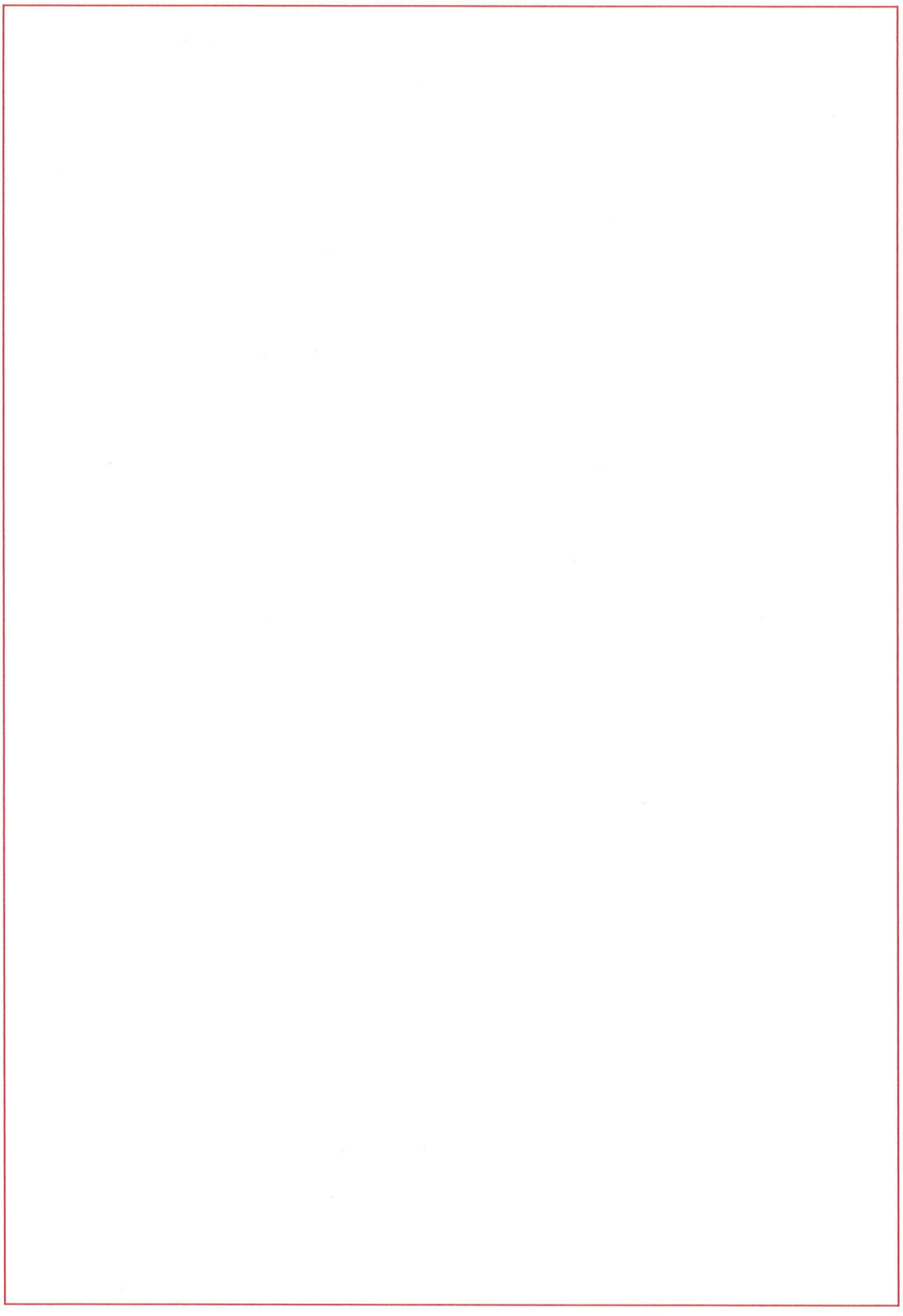

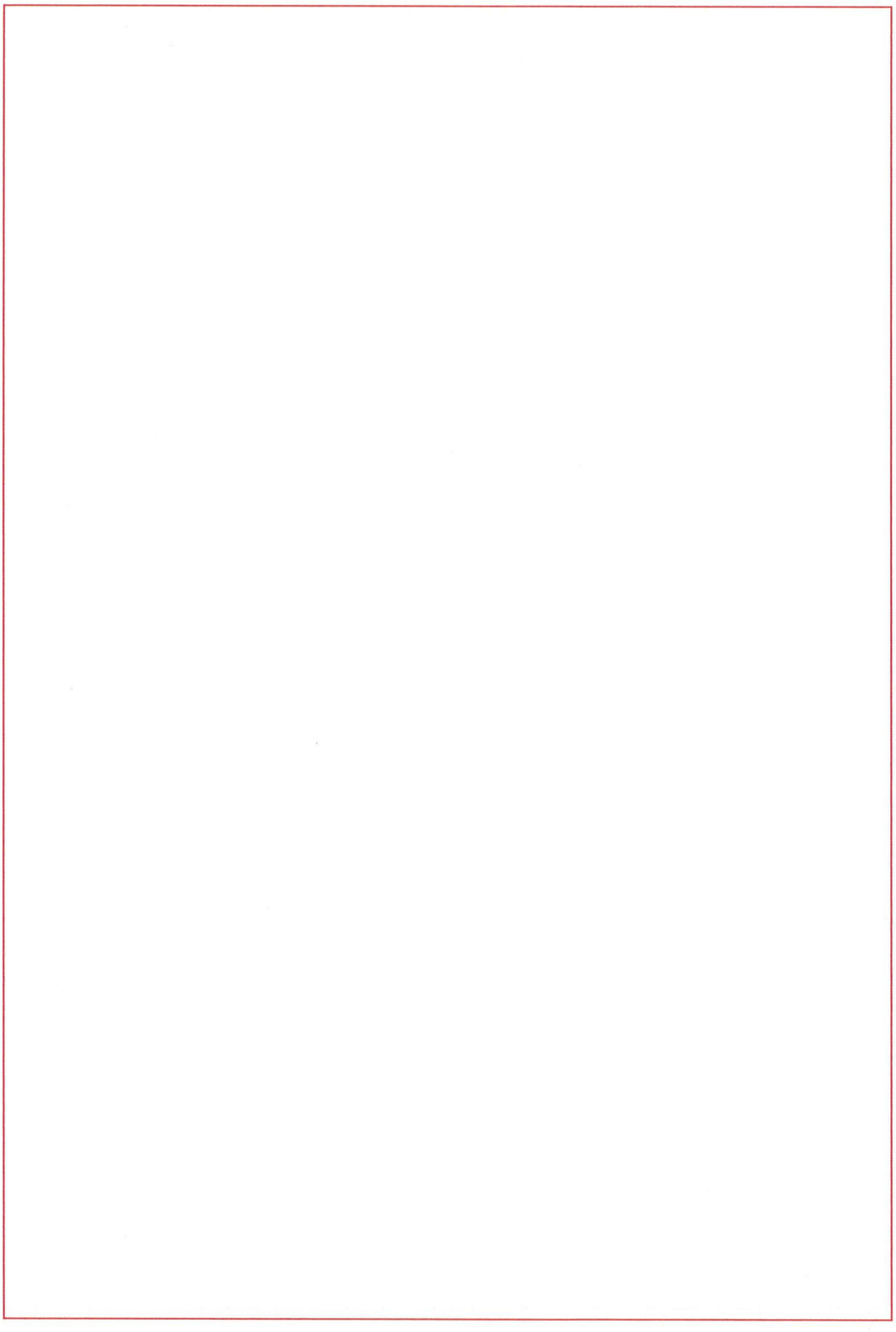

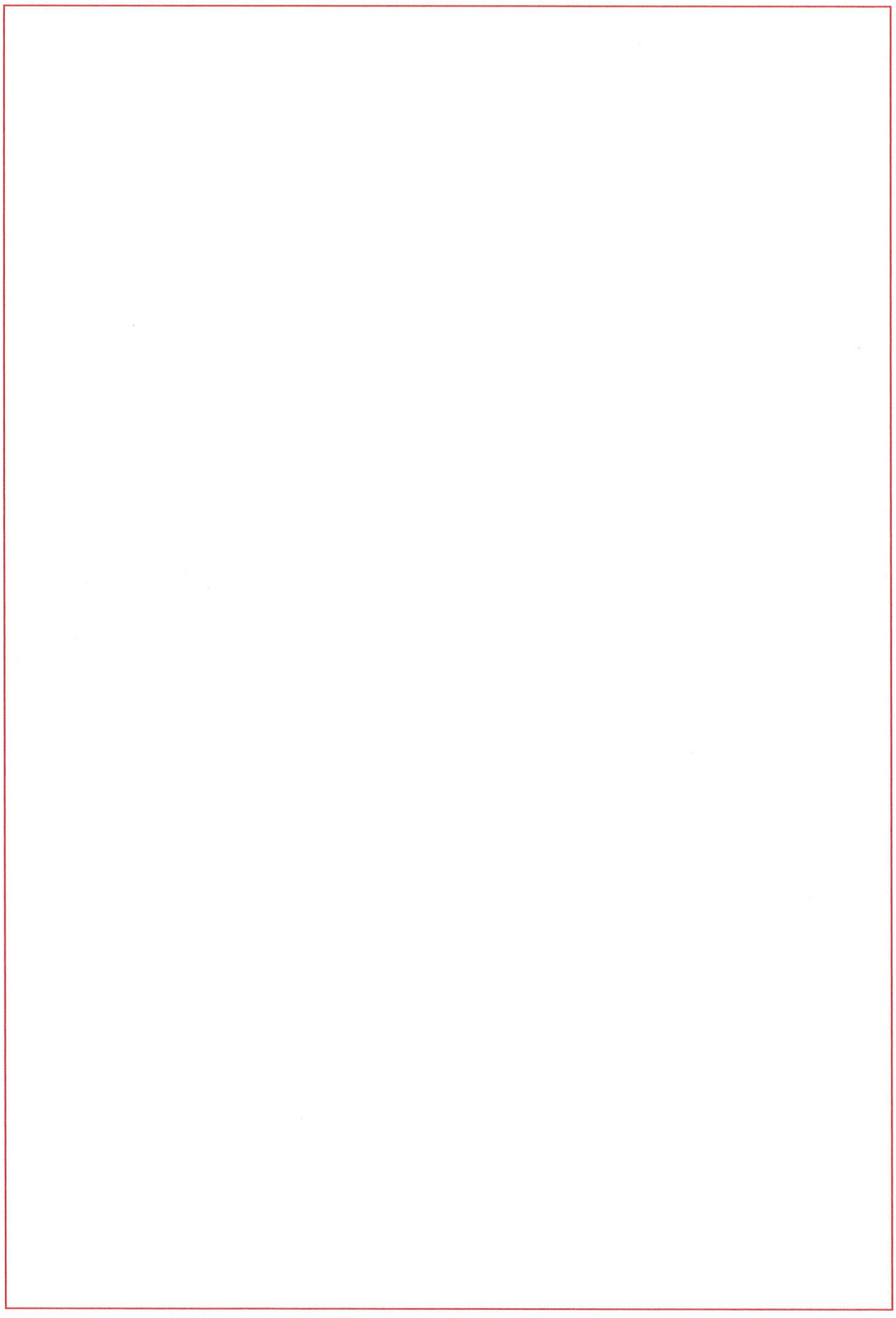

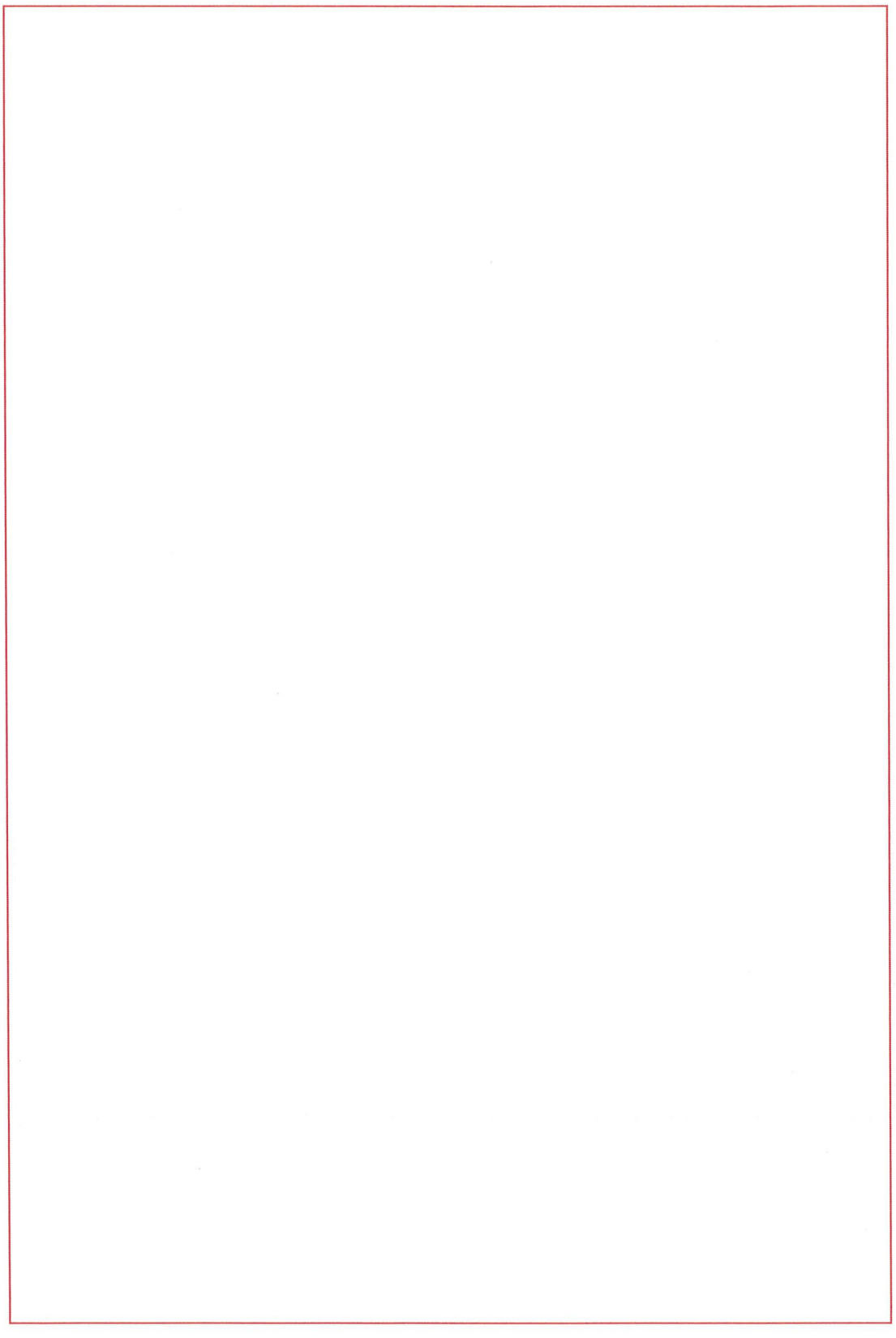

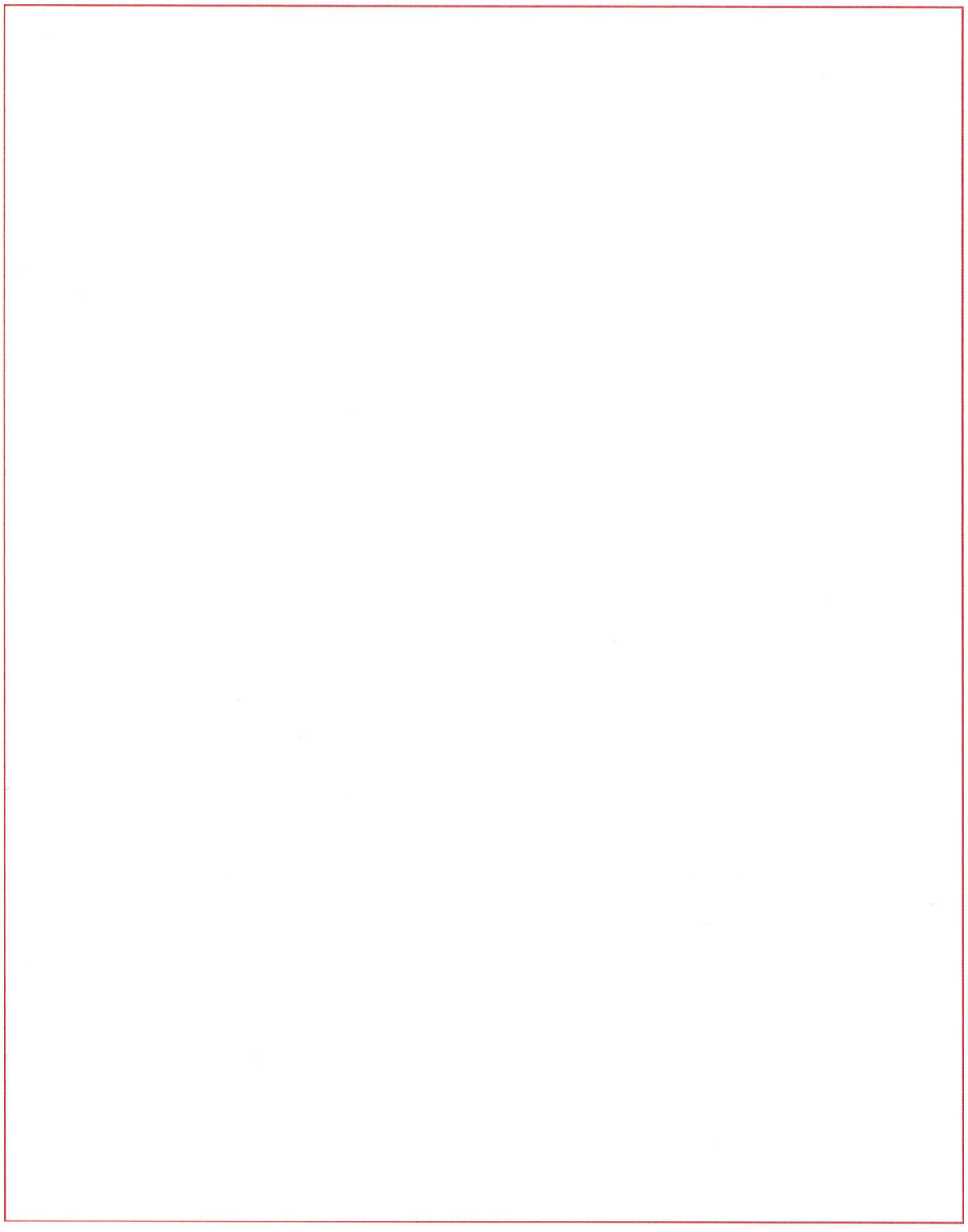

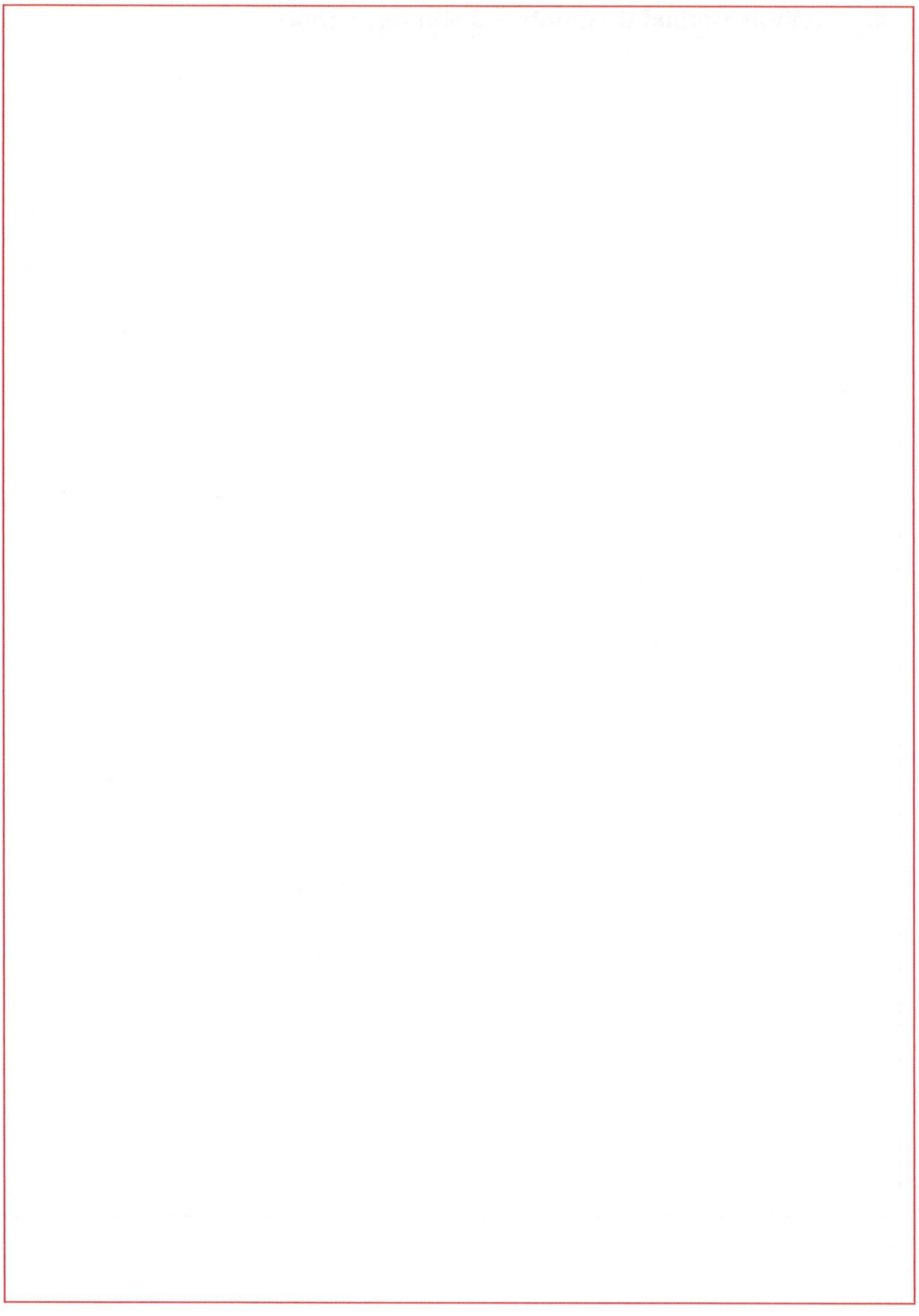

6.3. Analysis Method II - Combined Mining Method

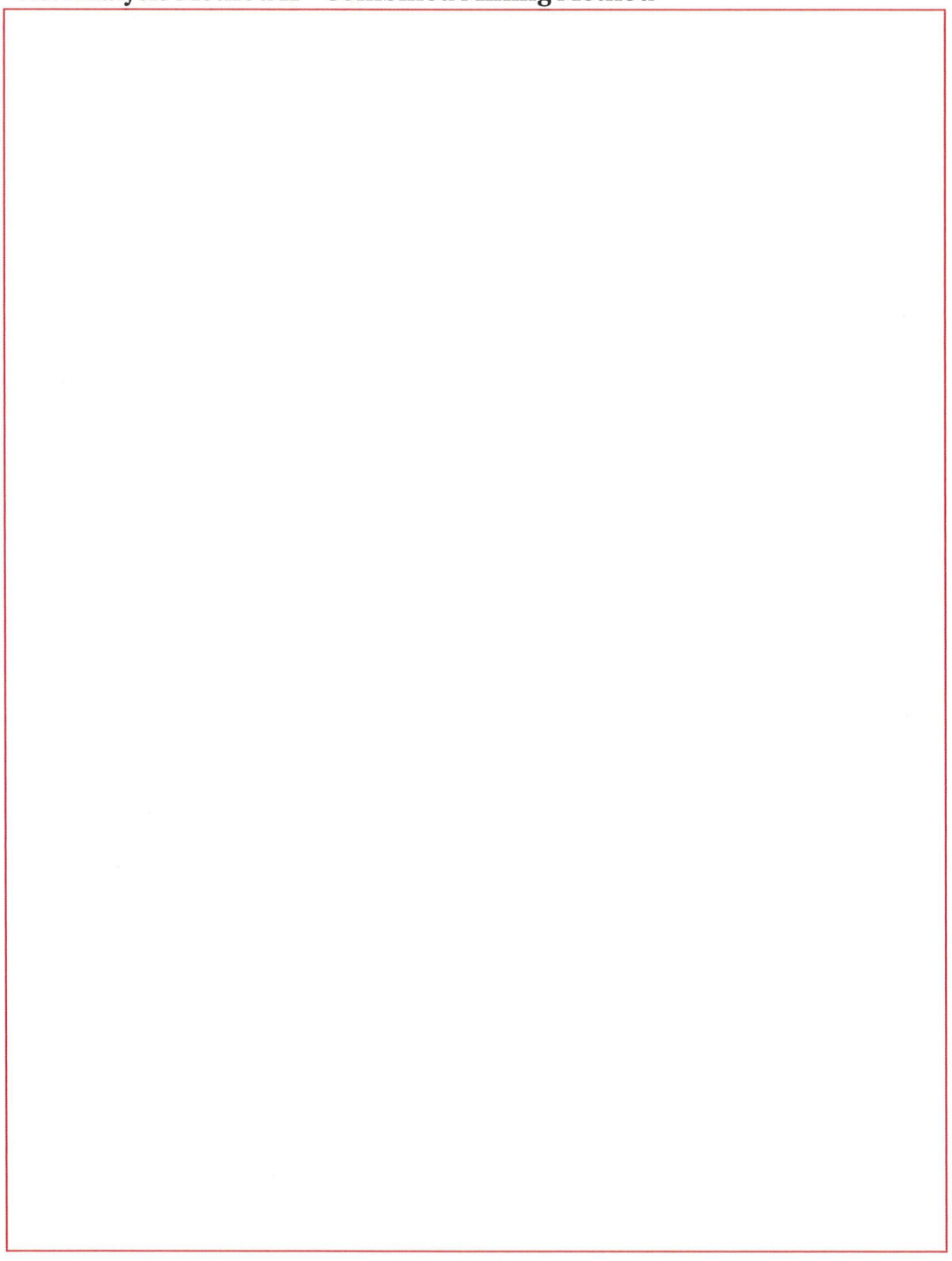

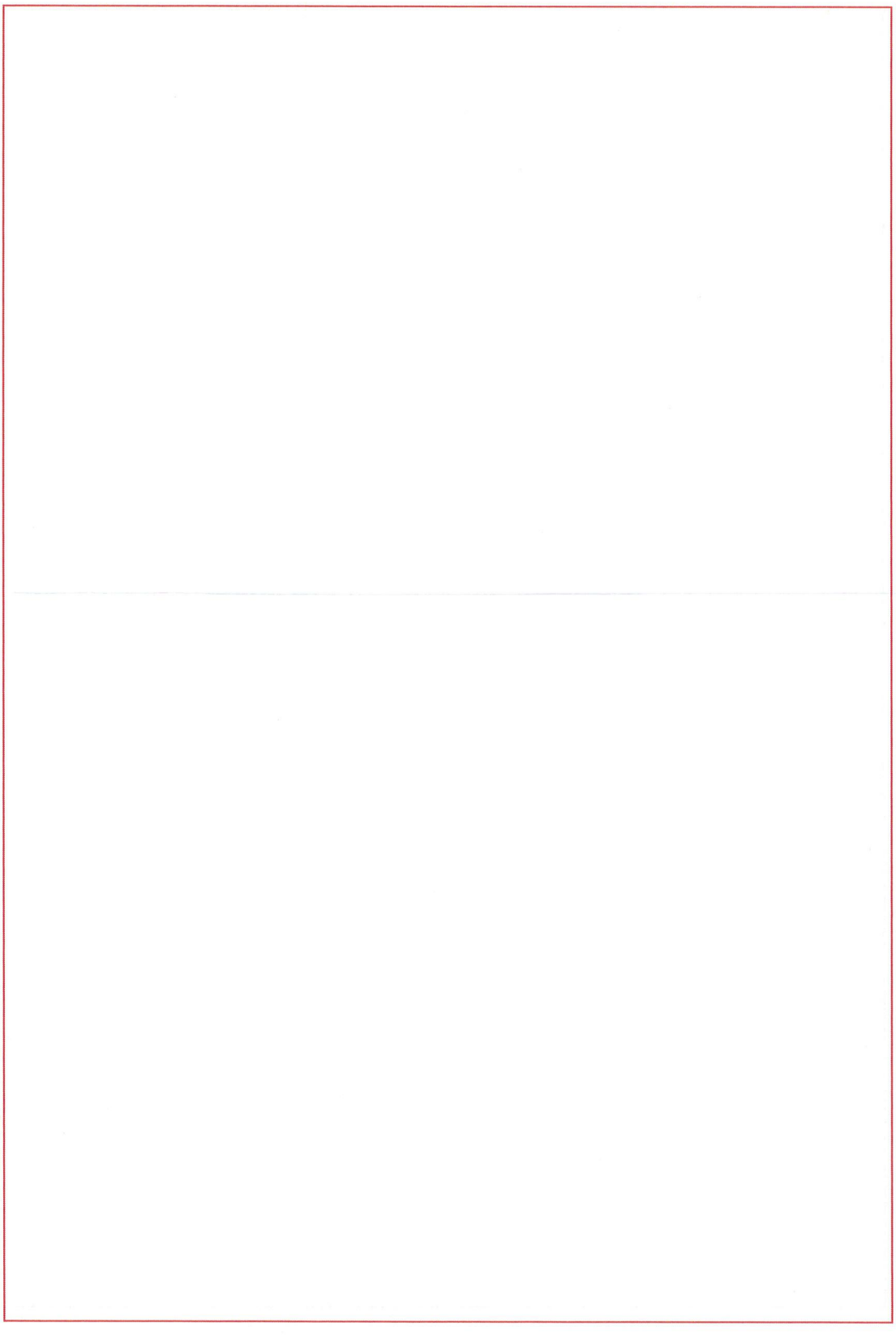

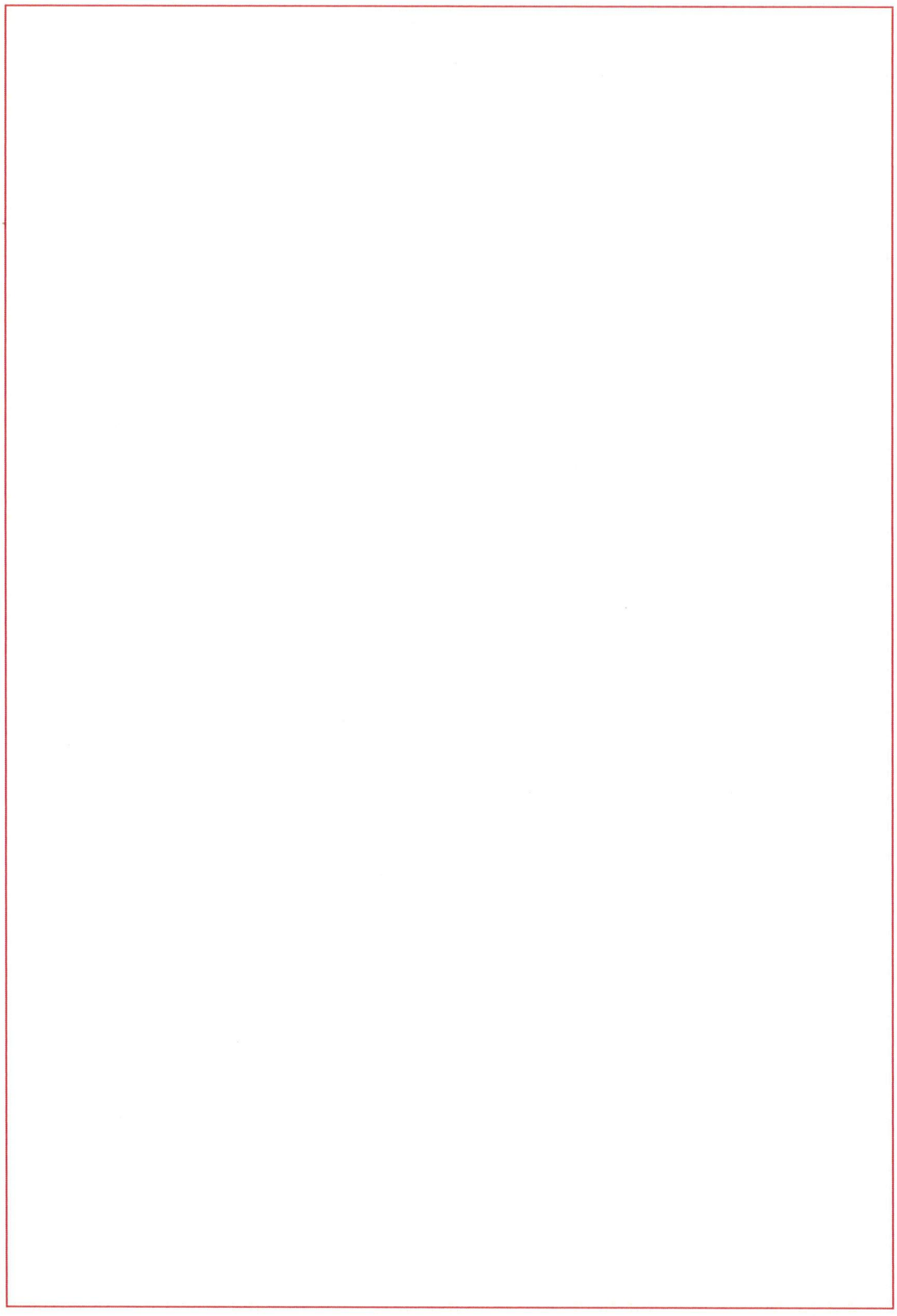

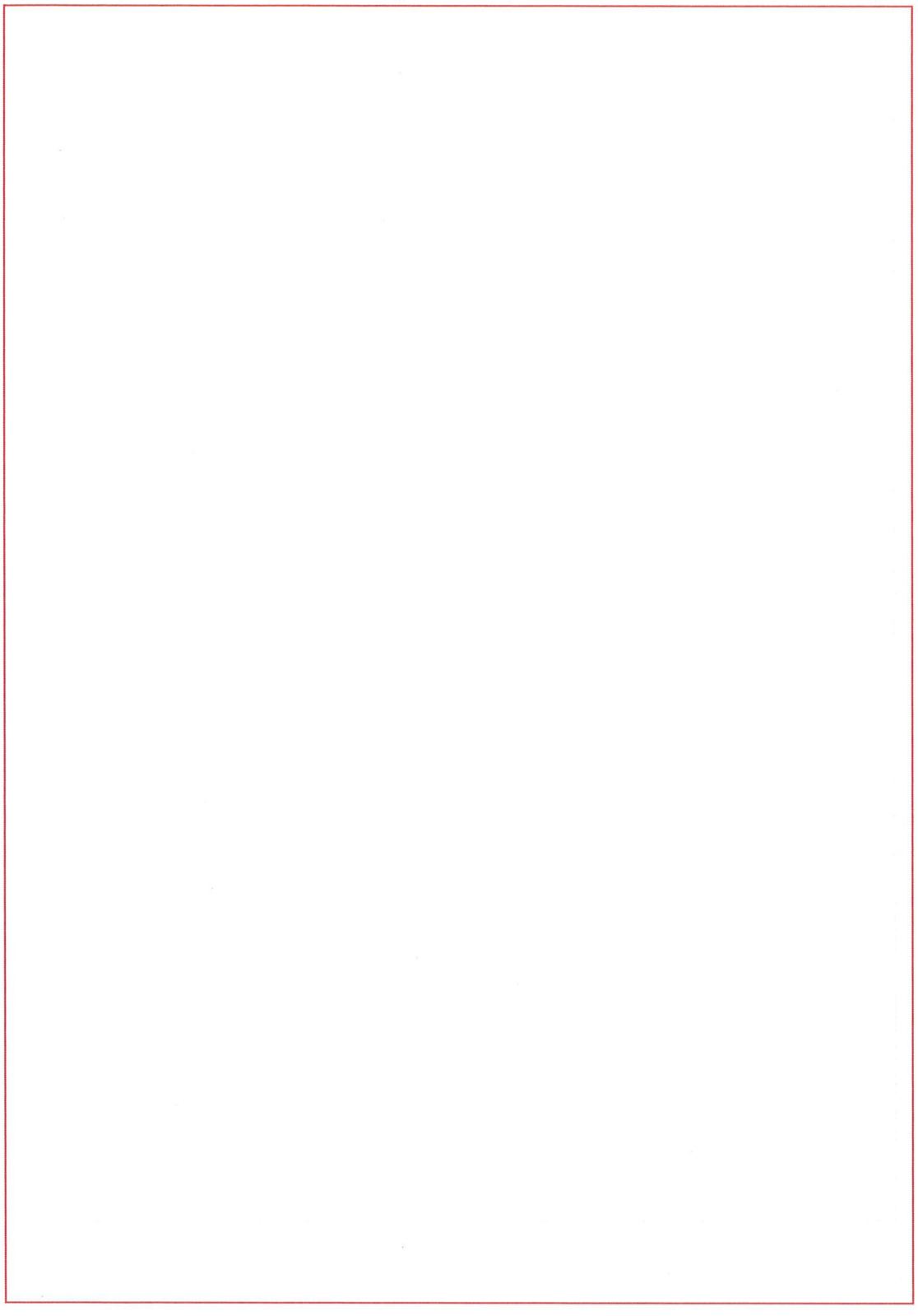

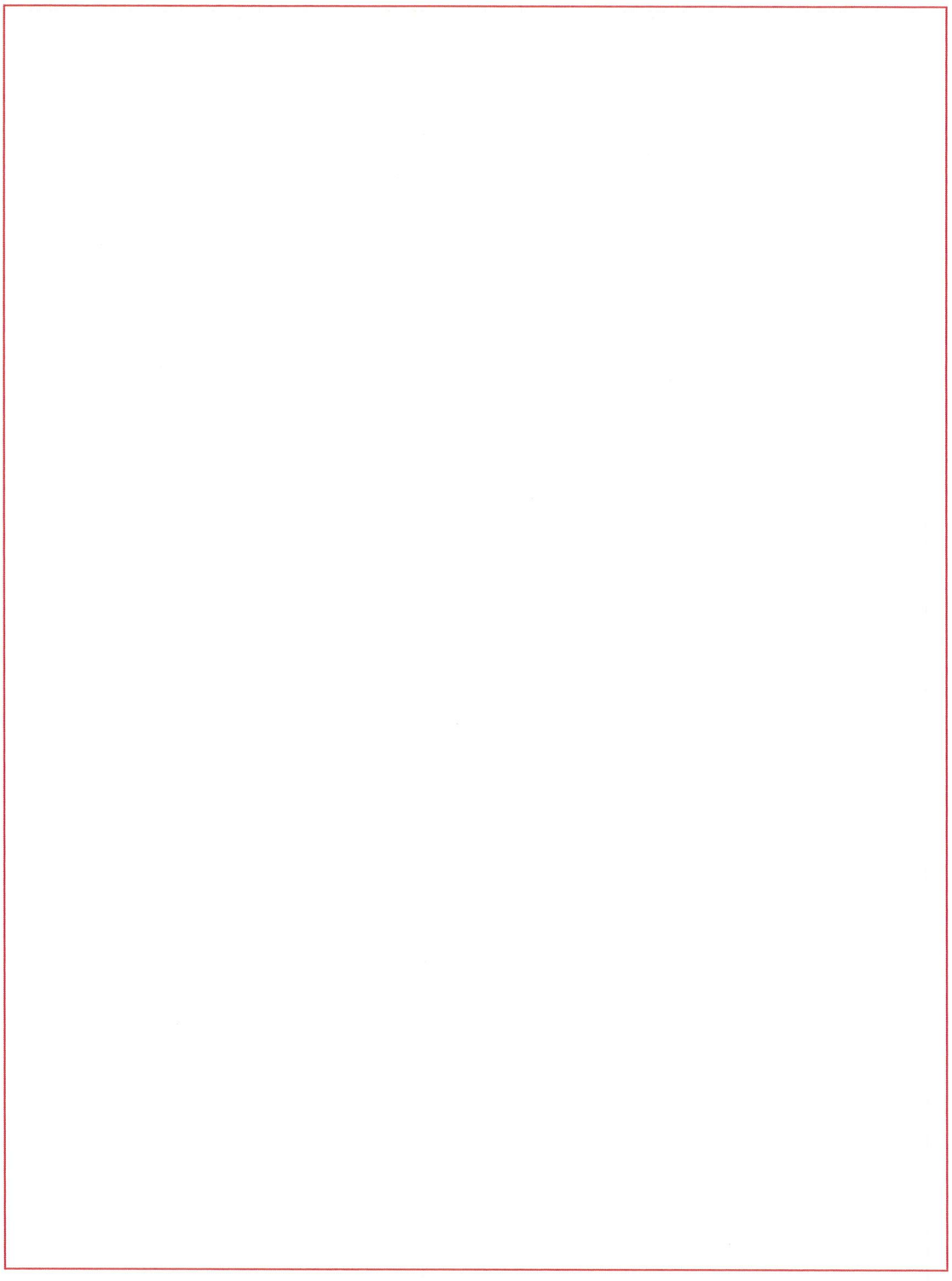

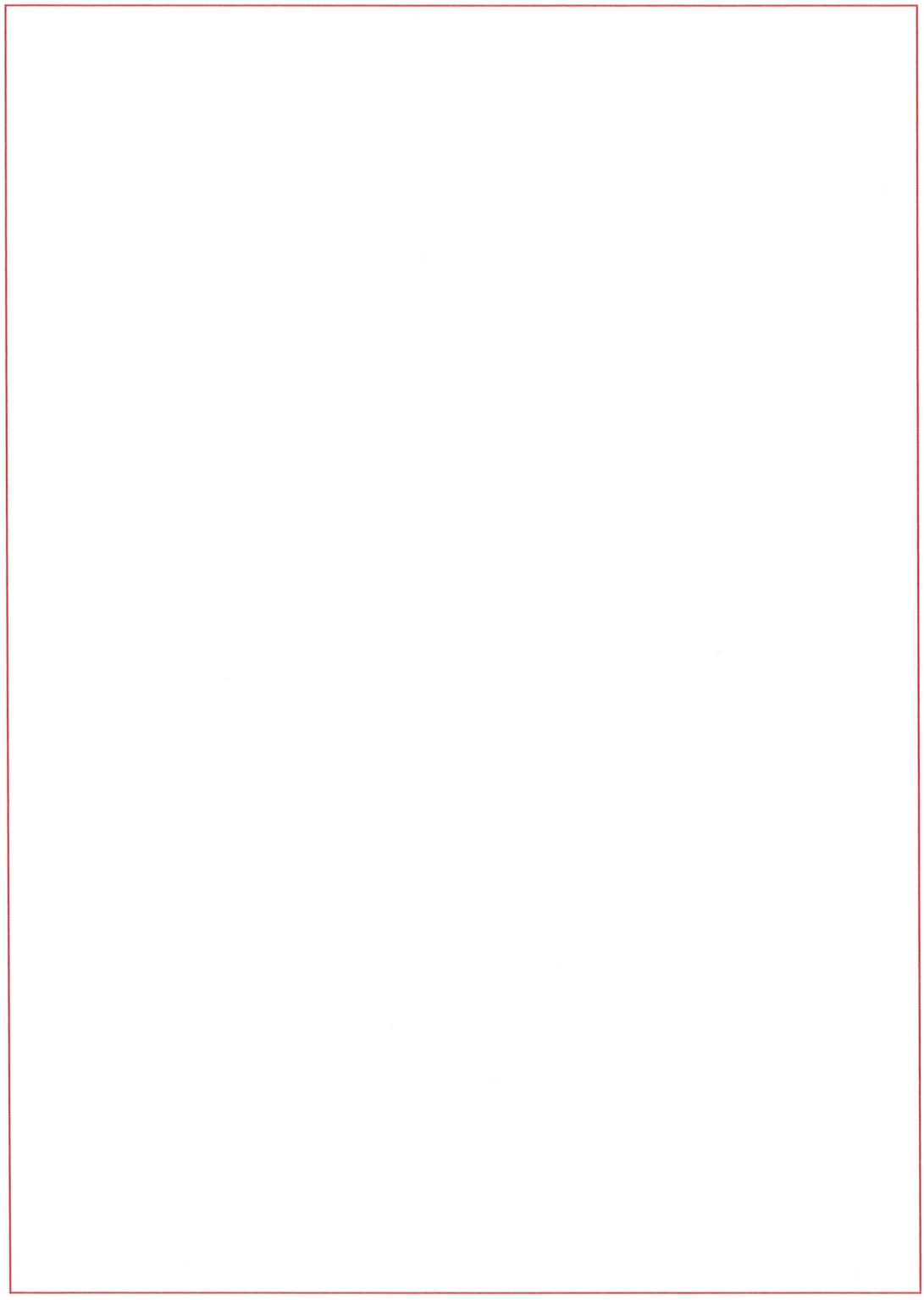

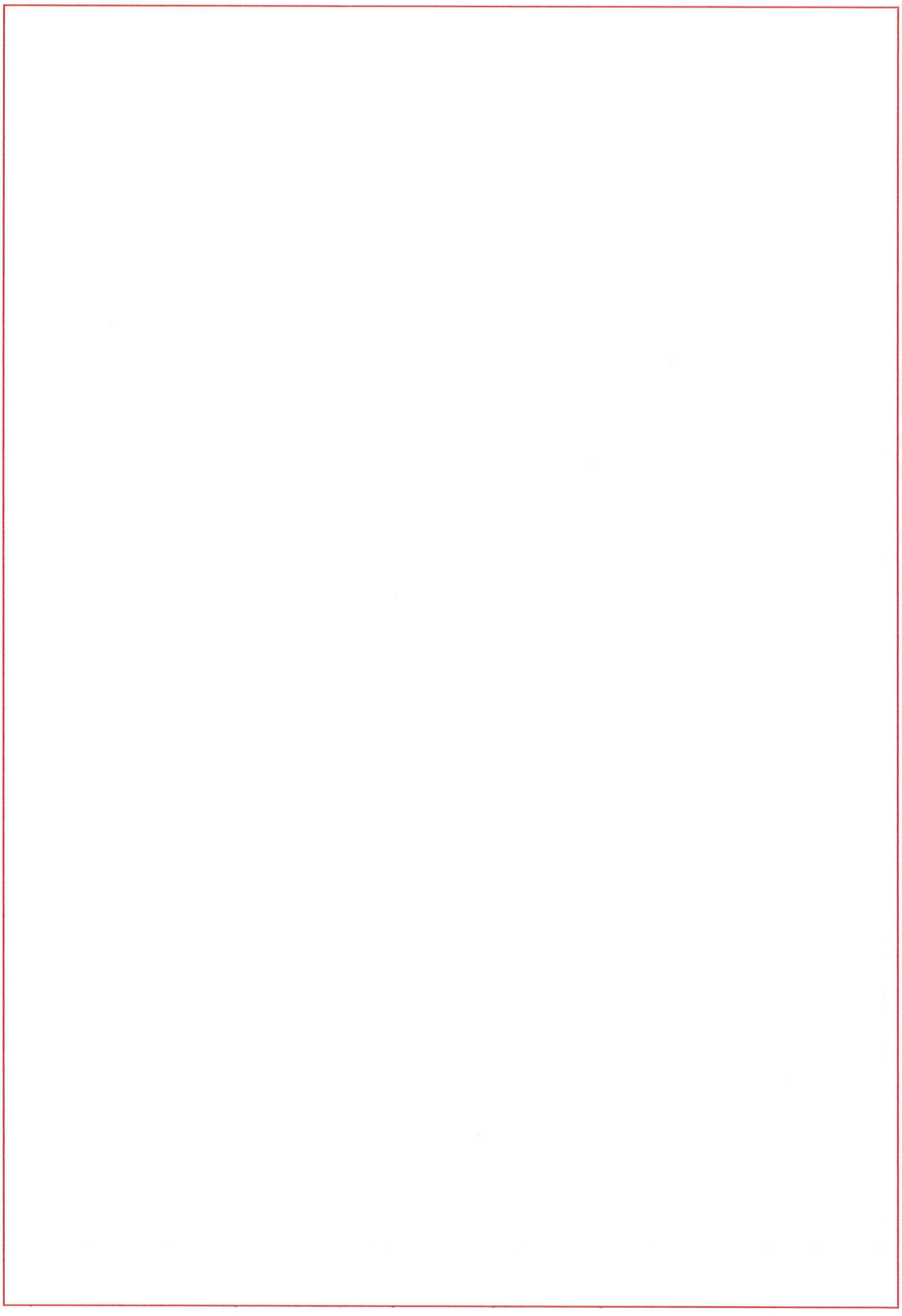

6.4. Nodule Collector Characteristics

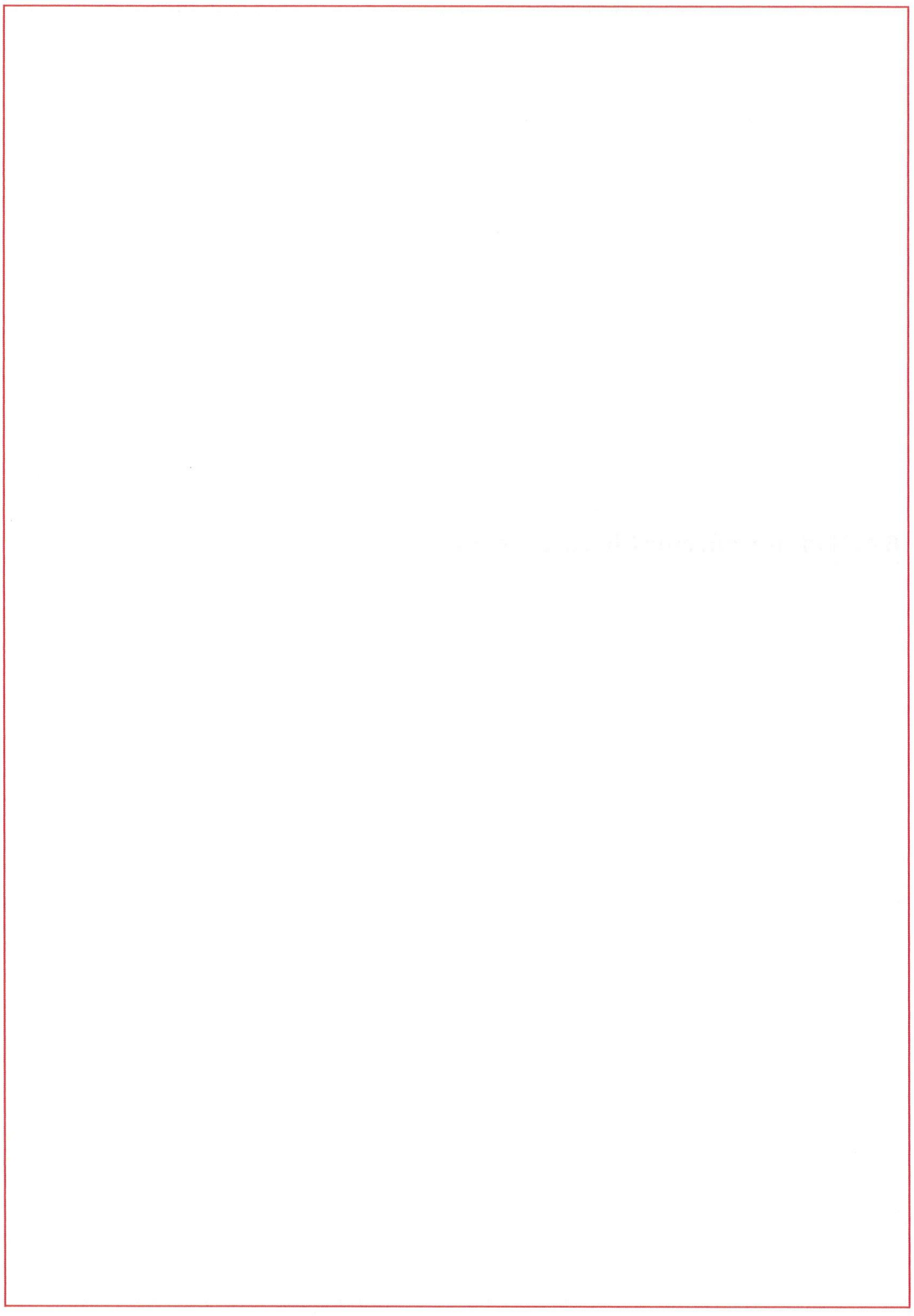

6.5. Method Recommendation

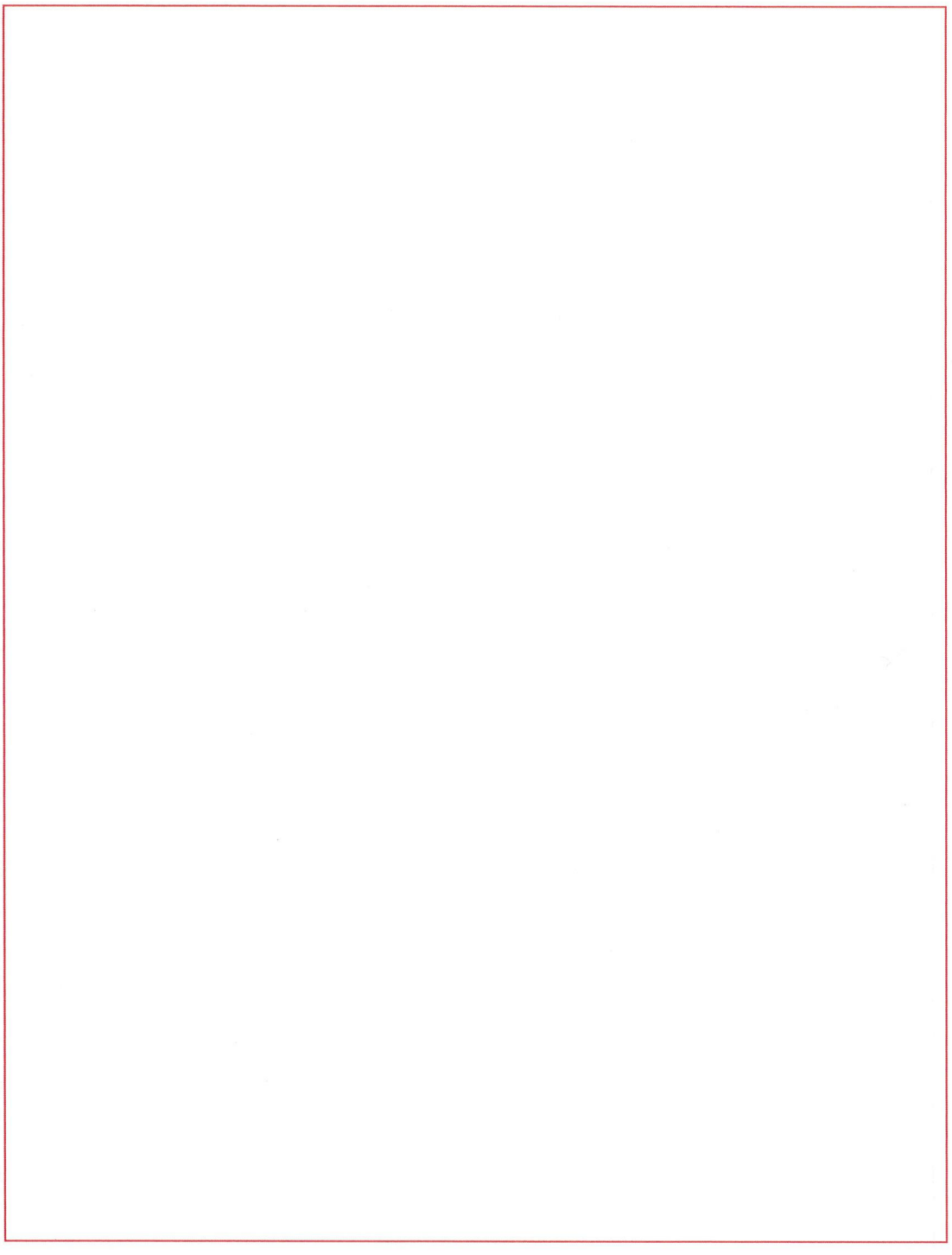

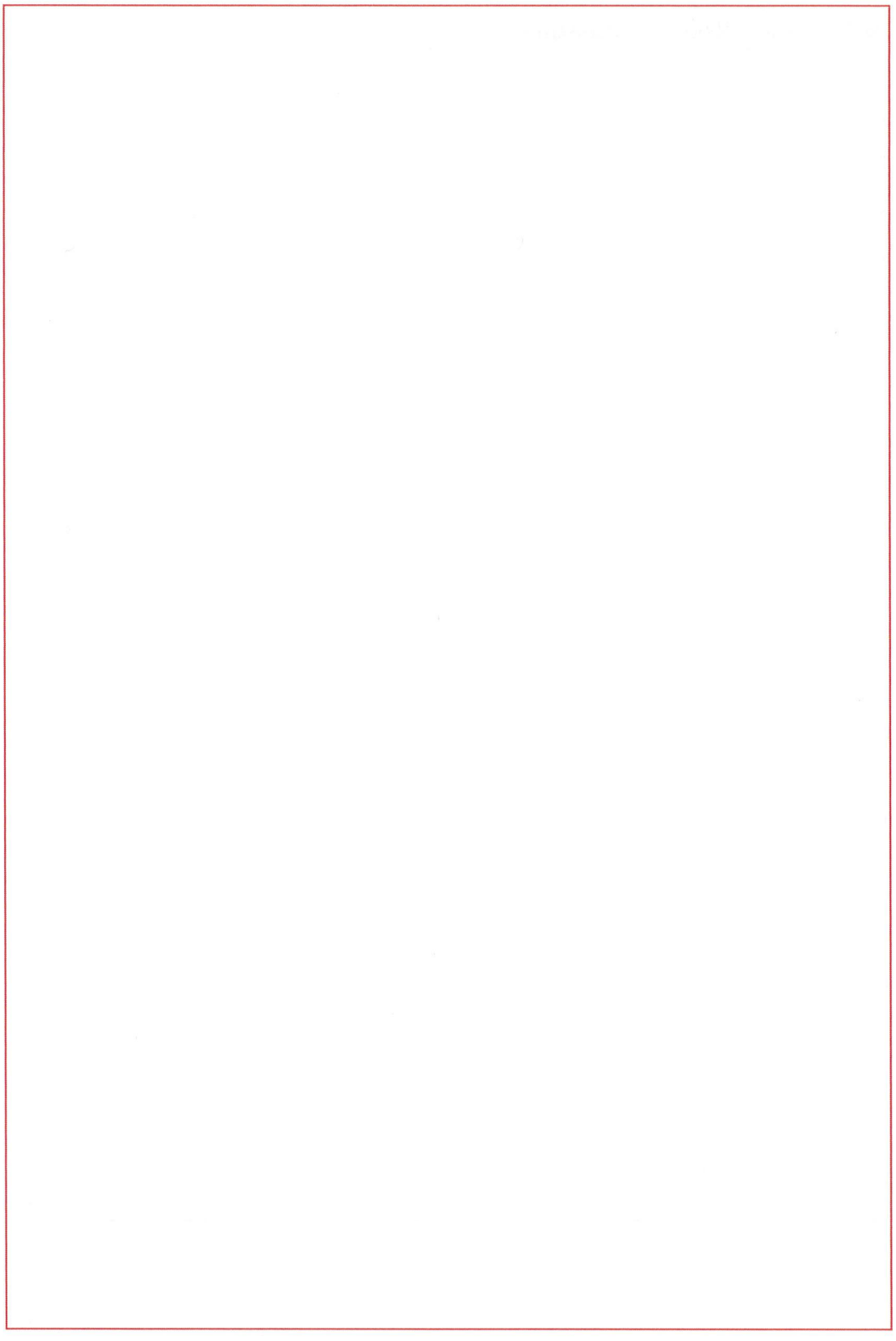

7

Mining Vessel

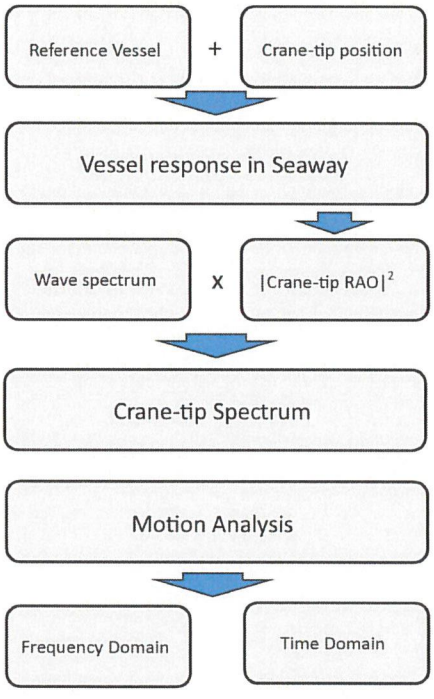

Figure 7.1: Plan of approach - Crane-tip response

7.1. Reference Vessel

The first step to be made is the introduction of a suitable mining vessel. The requirements for this vessel in terms of capacity and dimensions are already introduced in Section 3.2.1 and further specified in Appendix B. In order to determine the response of the vessel, the software package Seaway is applied. This program requires hull data of the mining vessel to perform its calculations. Whereas vessel design will not be within the scope of this study an appropriate hull is chosen and applied using pre-dimensioned hull forms [38]. This hull shape approaches the desirable dimensions and shape of the mining vessel and is therefore considered to be suitable in this stage. Specifications of the hull form can be found in Figure 7.2 and Appendix E.

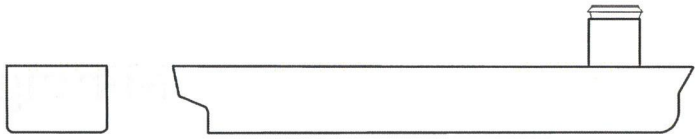

Figure 7.2: Mining vessel

Length	280	$[m]$	Volume	173243	$[m^3]$
Breadth	44,8	$[m]$	Mass	177574	$[t]$
Draft	16,6	$[m]$	Depth	NA	$[m]$

7.2. Crane-tip Options

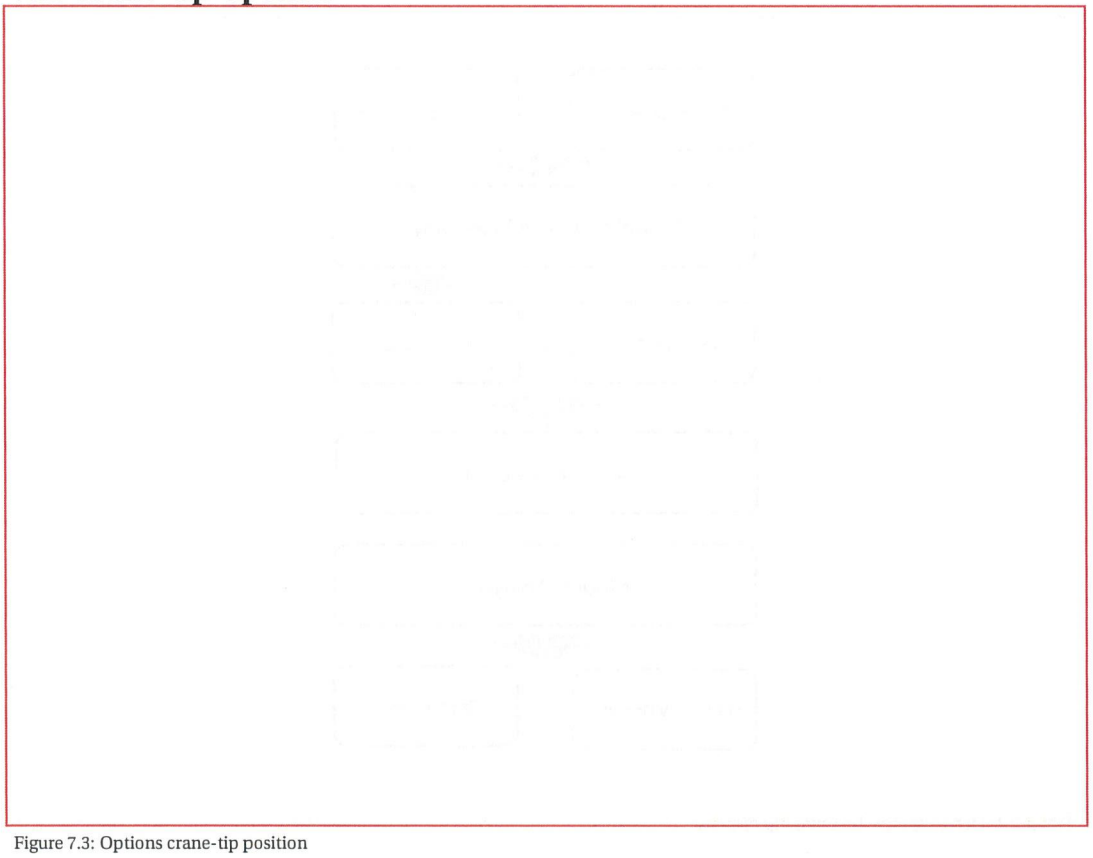

Figure 7.3: Options crane-tip position

7.3. Seaway

To determine the response of the vessel in a seastate, Seaway [17] is used. Seaway is a software package that calculates the ship response in the frequency-domain. It is based on both the ordinary and modified strip theory and calculates the motions of the mining vessel with six degrees of freedom in our seastate of interest. The reason for the choice of Seaway is founded in its user friendliness and the ability to include a constant vessel progress speed (which is the case during this mining operation).

Input files

The package requires two separate input data files: a hull form data file and a variable input data file. As described in Section 7.1 a preliminary design vessel was chosen from a set of hull form data files [38]. Both the hull form and variable input data are added to Appendix E.

Crane-Tip

The vessel motions calculated with Seaway (amplitudes and phases for all headings) are transformed into motions of the crane-tip in x,y and z direction. These calculations have been done for the crane-tip at the aft and side of the vessel, as shown in Figure 7.3. The transformation from vessel to crane-tip motions is done by the principle of superposition [18]. This procedure is added as Appendix F and results in RAO's [m/m] and phases [degr.] of the crane-tip.

7.4. Transfer Function and Response

The goal is to obtain plots, which we can use to compare the results of both crane-tip options in order to choose an appropriate location for the crane-tip. By using the calculated RAO's for the crane-tip and the wave-spectrum, we can obtain the energy response spectrum of the crane-tip. This spectrum already contains a lot of useful information for the crane-tip comparison. The spectrum is obtained using the following transfer function of the motion:

$$S_{ct}(\omega) = S_{\eta}(\omega)|H(\omega)|^2 \qquad [m^2 s] \tag{7.1}$$

In which:

$S_{ct}(\omega)$	Response spectrum of the crane-tip	$[m^2 s]$
$S_w(\omega)$	Energy density spectrum of wave surface elevation	$[m^2 s]$
$H(\omega)$	Transfer function of Response Amplitude Operator (RAO) of crane-tip	$[m/m]$

Now the wave energy is transposed into crane-tip response energy. By using this response spectrum we can obtain the first spectral moment of the crane-tip which will serve as input in calculating the significant response amplitude. The significant response amplitude, defined as the mean value of the highest one-third of the amplitudes, are used to compare the crane-tip response for various heading.
First spectral moment m_0:

$$m_0 = \int_0^{\infty} S_{ct}(\omega) \cdot \omega^0 \, d\omega \qquad [-] \tag{7.2}$$

Serving as input in obtaining the significant amplitude in for example z-direction:

$$z_{a1/3} = 2 \cdot RMS = 2\sqrt{m_{0z}} \qquad [m] \tag{7.3}$$

The results and comparison of the significant amplitude for various heading is given in Section 7.5.

7.5. Results

The results of the calculations performed in previous section are given in Figure 7.4 and 7.5. These graphs represent the significant amplitude in surge-,sway- and heave direction as a function of the wave heading (0-360 Degr.). Figure 7.4 represents the aft situation and Figure 7.5 the starboard option.

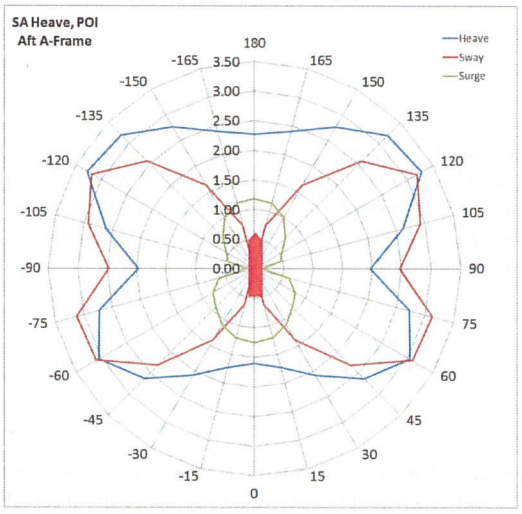

Figure 7.4: Aft crane-tip

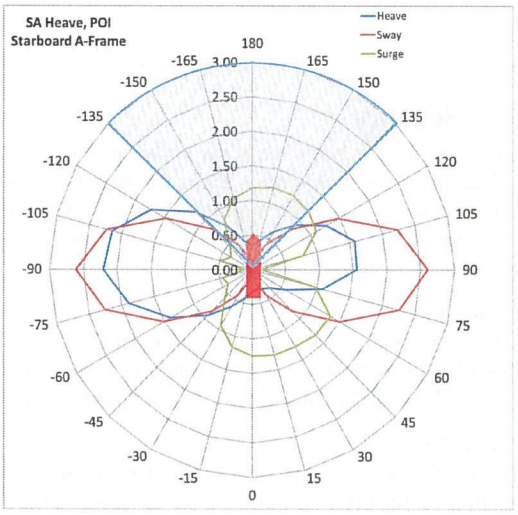

Figure 7.5: Starboard crane-tip

As can be clearly seen, the preferable position of the crane-tip is the starboard location. With the exception for waves coming from portside (270 °), all the amplitudes are significantly smaller when compared to the aft position. With current knowledge, we assume the heave motion to have the highest priority. In that case bow waves (heading of 180 °) are the ideal working condition. A conservative approach would be to consider all the waves within the range 135 °till and 225 °and choose the largest significant amplitude. For that scenario the waves with a heading of 225 °are the conservative ones. These waves, called bow-quartering, are applied in further calculations. For information purposes the heave RAO's and obtained spectra for both outermost headings within the wave range are given in respectively Figure 7.6 and 7.7.

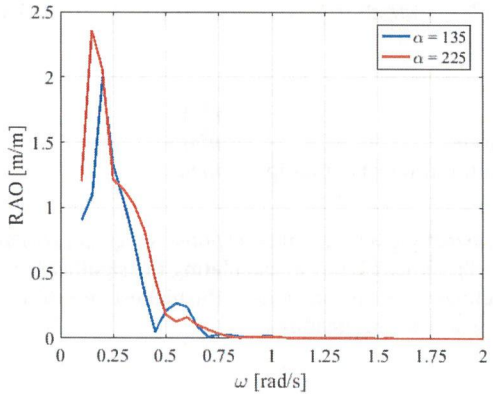

Figure 7.6: RAO crane-tip heave direction

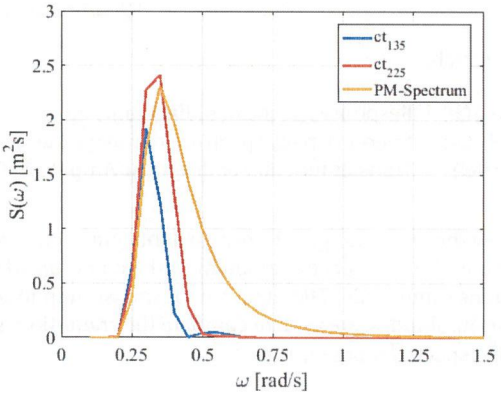

Figure 7.7: Crane-tip heave spectrum comparison

7.6. Motion Analysis: Time domain

Previous obtained results are all in the frequency domain and therefore not sufficient in case of non-linear behavior. To create the ability to incorporate non-linear behaviour in the dynamic part of this study, a transformation to the time-domain is required. The goal of this transformation is to obtain a deterministic time

record of the crane-tip motion which has the statistical properties of the obtained crane-tip spectrum. This means that the created time signal, once transformed back into frequency domain, must have the same energy density spectrum as the original spectrum [18]. First, a time-series of the the irregular sea-sate is created by modelling the waves as a summation of many sinusoidal wave components. The wave statistics were described using the Modified Pierson-Moskowitz spectrum, see Figure 7.8. The transformation is done by implementing the required constants into:

$$\zeta(t) = \sum_{n=1}^{N} \zeta_{a_n} \; cos(k_n x - \omega_n t + \varepsilon_n) \qquad [m] \tag{7.4}$$

Where:

$$\zeta_{a_n} = 2\sqrt{S_\zeta(\omega) \cdot \Delta\omega} \qquad [m] \tag{7.5}$$

The phase is uniform distributed and therefore chosen to be random to create a random time-series. In choosing an appropriate frequency step-size, repetition in the signal is avoided. The procedure results in the irregular time-series of the wave surface elevation, shown in Figure 7.9.

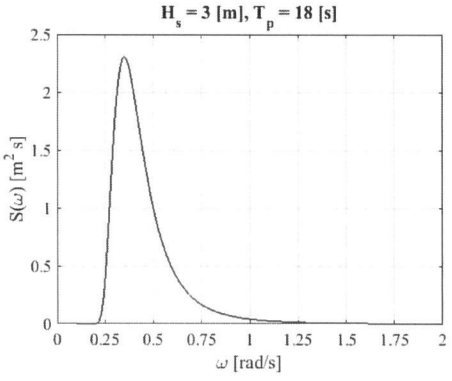

Figure 7.8: Pierson-Moskowitz spectrum

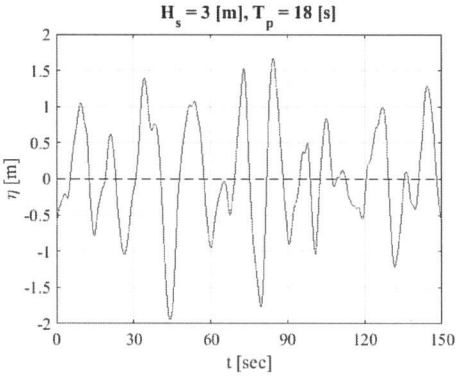

Figure 7.9: Time series surface elevation

Using the irregular time-series of the surface elevation, the obtained RAO's of the mining vessel and the crane-tip transfer function, an irregular time-series for the crane-tip is created. The created time-series has been validated by a fourier transformation using Matlab and the crane-tip spectrum. The results are shown in Figure 7.10.

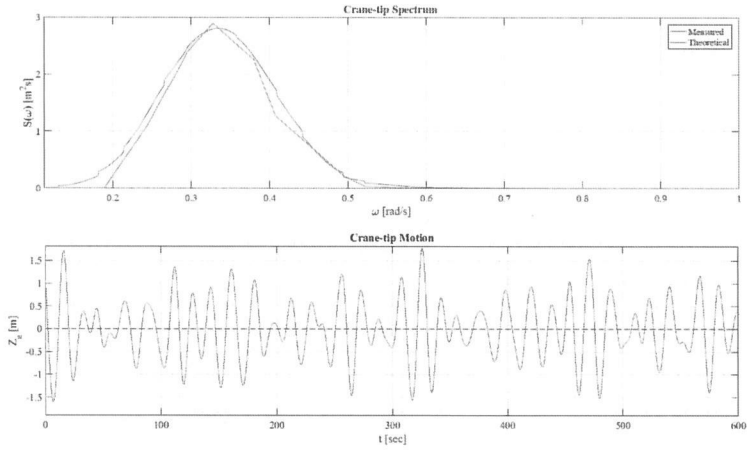

Figure 7.10: Time domain signal - Crane-tip in z-direction

8

Dynamic Analysis

8.1. Cases of Interest

8.2. Axial Analysis

In this section the analysis is done in one dimension, only axially. We are interested in the vertical response of the wire and attached object as result of the crane-tip motions. First the applied one-dimensional model is briefly introduced and derived. The derivation can be described as a transformation from a continuous model to a discretized numerical model, see Figure 8.2. Afterwards, both the resonance occurrence and skip response will be investigated. An elaboration with respect to the derivation can be consulted in Section G.1 of Appendix G. To simplify the problem, the following assumptions apply [29, 41]:

(1) The dual wire operation is calculated as a single wire operation under the assumption that; the payload can be equally divided and the response is symmetric
(2) Torsion in the wire is neglected
(3) The vertical motion of crane-tip and attached object dominate and therefore other motions can be disregarded
(4) Offset as a result of current forces is in the axial analysis disregarded
(5) The motion of the vessel is not affected by the motion of the attached object
(6) The motion of the crane-tip is identical with that of the support-vessel (considering the method of superposition), dynamic characteristics of the deck-crane or A-frame are neglected

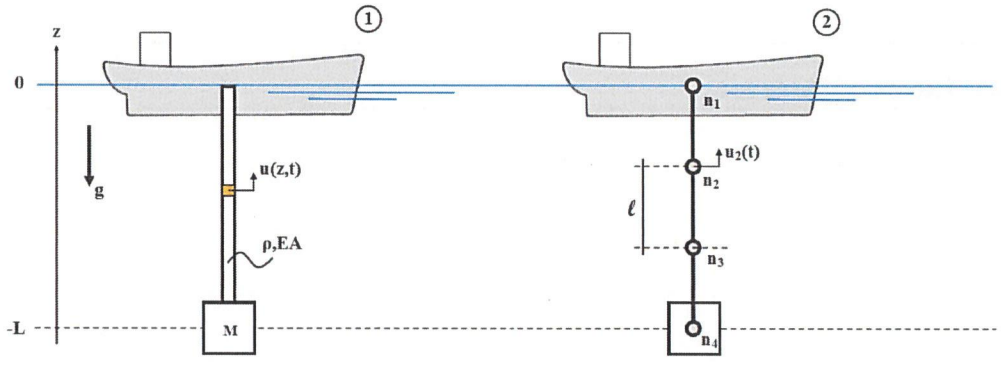

Figure 8.2: Continuous system (1) and discretized system (2)

8.2.1. Model

The axial equation of motion of a suspended wire in continuous form can be written according to the linear rod equation [26]. The suspended situation results into (submerged) gravitational terms on the right-hand-side of the equation. Per unit length the equation can be written as:

$$\rho A\frac{\partial^2 u(z,t)}{\partial t^2} - EA\frac{\partial^2 u(z,t)}{\partial z^2} = (\rho Ag)_s \qquad for \qquad -L<z<0 \tag{8.1}$$

where $u(z,t)$ is the displacement in the vertical plane, z the coordinate parallel to the wire, ρA the mass of the wire per unit length, EA the axial rigidity and g the gravitational acceleration. The subscript indicates the submerged situation. The initial displacement along the wire length is dependent on the elongation of the wire under its self-weight. The initial velocity is chosen to be 0. Both can expressed as:

$$u(z,0) = \frac{\rho g}{2E}z^2 + \left\{\frac{Mg}{EA} + \frac{\rho gl}{E}\right\}z \qquad and \qquad \dot{u}(z,0) = 0 \tag{8.2}$$

Where M represents the mass of the object attached to the tip of the wire, see Figure 8.2 The boundary conditions are dictated by the motions of the crane-tip and the presence of the load attached. At the tip of the wire, the submerged situation of the object results into added mass and non-linear drag. The drag force on the payload is considered to be proportional to the velocity squared with a constant drag term c dependent on the characteristics of the payload.

$$u(0,t) = u_{ct}(t) \qquad and \qquad -EA\left(\frac{\partial u(z,t)}{\partial z}\right)\Big|_{z=-L} = M_{obj}g - \{(M_{obj}+m_a)\ddot{u}_{obj} + c\dot{u}_{obj}|\dot{u}_{obj}|\} \tag{8.3}$$

With

$$c = \frac{1}{2}\rho_w C_{D;z} A \tag{8.4}$$

where ρ_w is the density of the surrounding water, $C_{D;z}$ is the drag coefficient in z-direction dependent on the shape of the object, A is the objects surface area. In order to solve these equations, a numerical method is applied.

Numerical Representation

The equation of motion of the suspended wire (Eq- 8.1) is written in continuous form. This form can be turned into a discretized form by applying the LaGrangian formalism [19]. By this approach, the suspended wire can be written in finite elements. This is done by the energy principle of:

$$\mathscr{L} = T - V = \int_l \int_A \left(\rho(z)V(z)^2 - E(z)\frac{du(z)}{dz}\frac{du(z)}{dz} = \rho g\right) dA\,dz \tag{8.5}$$

If we apply the LaGrangian formalism, using linear shape functions, we obtain the undamped equation of motion in the form;

$$\overline{M}\ddot{u} + \overline{K}u = \overline{F} \tag{8.6}$$

The full elaboration can be found in Appendix G When written in matrix form we obtain:

$$\frac{\rho Al}{6}\cdot\begin{pmatrix} 2 & 1 & \cdots & 0 & 0 \\ 1 & 4 & \cdots & 0 & 0 \\ \vdots & \vdots & \ddots & \vdots & \vdots \\ 0 & 0 & \cdots & 4 & 1 \\ 0 & 0 & \cdots & 1 & 2 \end{pmatrix}\cdot\begin{pmatrix} \ddot{u}_1 \\ \ddot{u}_2 \\ \vdots \\ \ddot{u}_{n-1} \\ \ddot{u}_n \end{pmatrix} + \frac{EA}{l}\begin{pmatrix} 1 & -1 & \cdots & 0 & 0 \\ -1 & 2 & \cdots & 0 & 0 \\ \vdots & \vdots & \ddots & \vdots & \vdots \\ 0 & 0 & \cdots & 2 & -1 \\ 0 & 0 & \cdots & -1 & 1 \end{pmatrix}\cdot\begin{pmatrix} u_1 \\ u_2 \\ \vdots \\ u_{n-1} \\ u_n \end{pmatrix} = \frac{\rho Agl}{2}\begin{pmatrix} 1 \\ 2 \\ \vdots \\ 2 \\ 1 \end{pmatrix} \tag{8.7}$$

The result is a system of equations of a size with a number of N elements and n nodes and can be best described as a lumped-mass method. The motions of the nodes, acceleration and displacement, are shown as vectors in Eq=8.7.

Boundary Conditions

The boundary conditions are related to the vessel and the attached object. At the top of the wire the crane-tip dictates the motion of the first node, which can be written as:

$$u(0,t) = u_1 = u_{ct}(t) \tag{8.8}$$

The object is attached (empty/ full skip or collector) at the tip of the wire. This boundary can be expressed as an additional equation of motion for the node u_n. This equation includes added mass and non-linear damping terms and a gravitational contribution as a result of the submerged self-weight of the object. The last equation of motion in the one-dimensional system is adjusted according to these contributions.

Initial Conditions

The initial conditions are dependent on the elongation of the suspended wire under its submerged self-weight. In order to calculate the initial displacement, the constraint of the crane-tip fixation is applied. This

results in a system of *(n-1)* · *(n-1)*, starting at the second node. The initial position of each node can now easily be determined by the following relation ship:

$$u(z,0) = \overline{K}^{-1} \cdot \overline{F} \tag{8.9}$$

The numerical values of elongation are compared with the analytical expression in Eq-8.2 and validated using the DNV-formula for elongation.

Number of Degrees of Freedom
The number of degrees of freedom is proportional to the accuracy. Especially when passing an interface (e.g. transition from air to fluid or penetrating a soil) the number of degrees can have a huge influence. However, in this axial situation the complete system is submerged. In practice this type of situation is often simplified into a single-degree of freedom system, neglecting the material- and skin friction damping terms. In order to take these influences into account, multiple degrees of freedom are applied until the results converge to acceptable values.

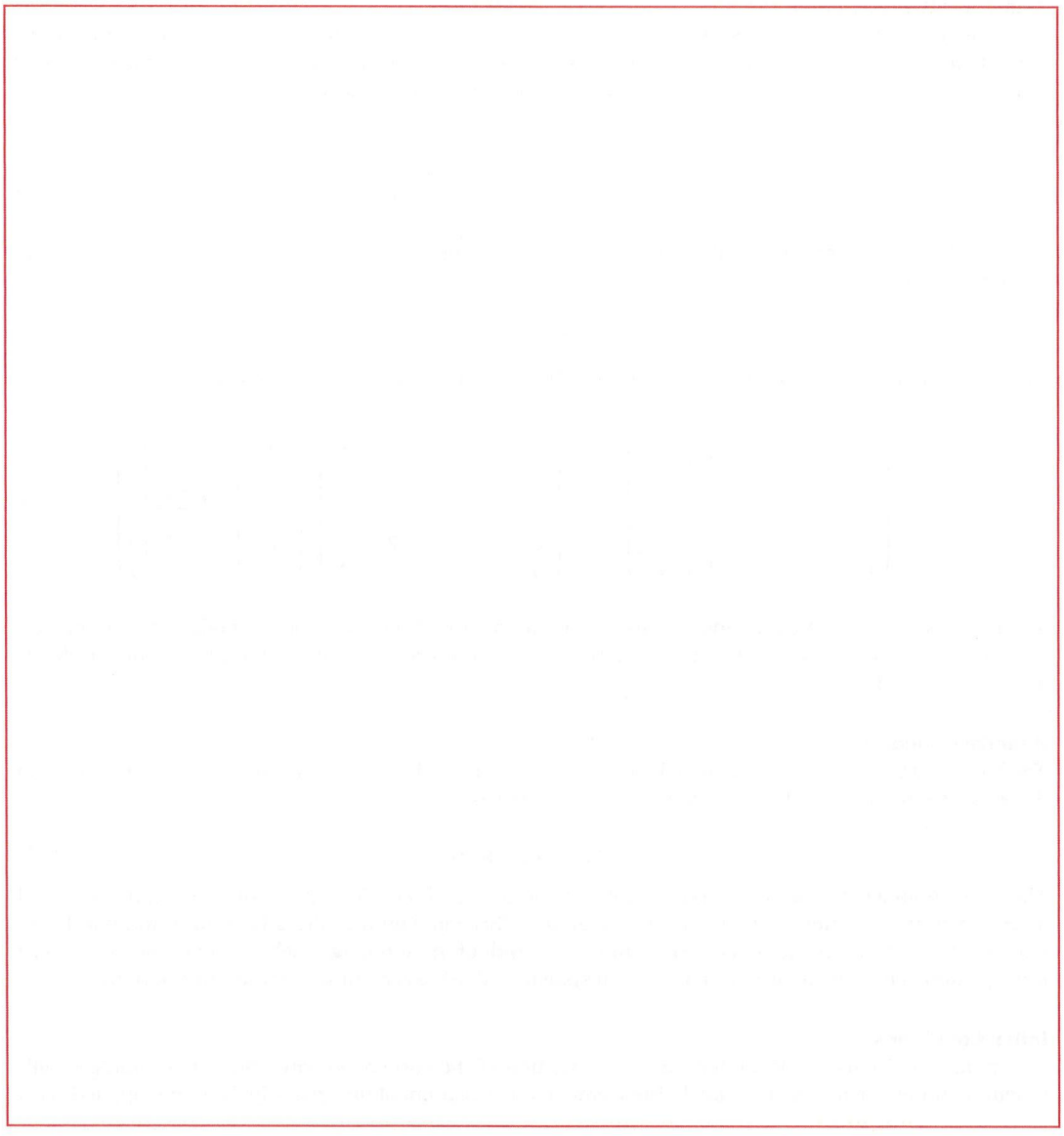

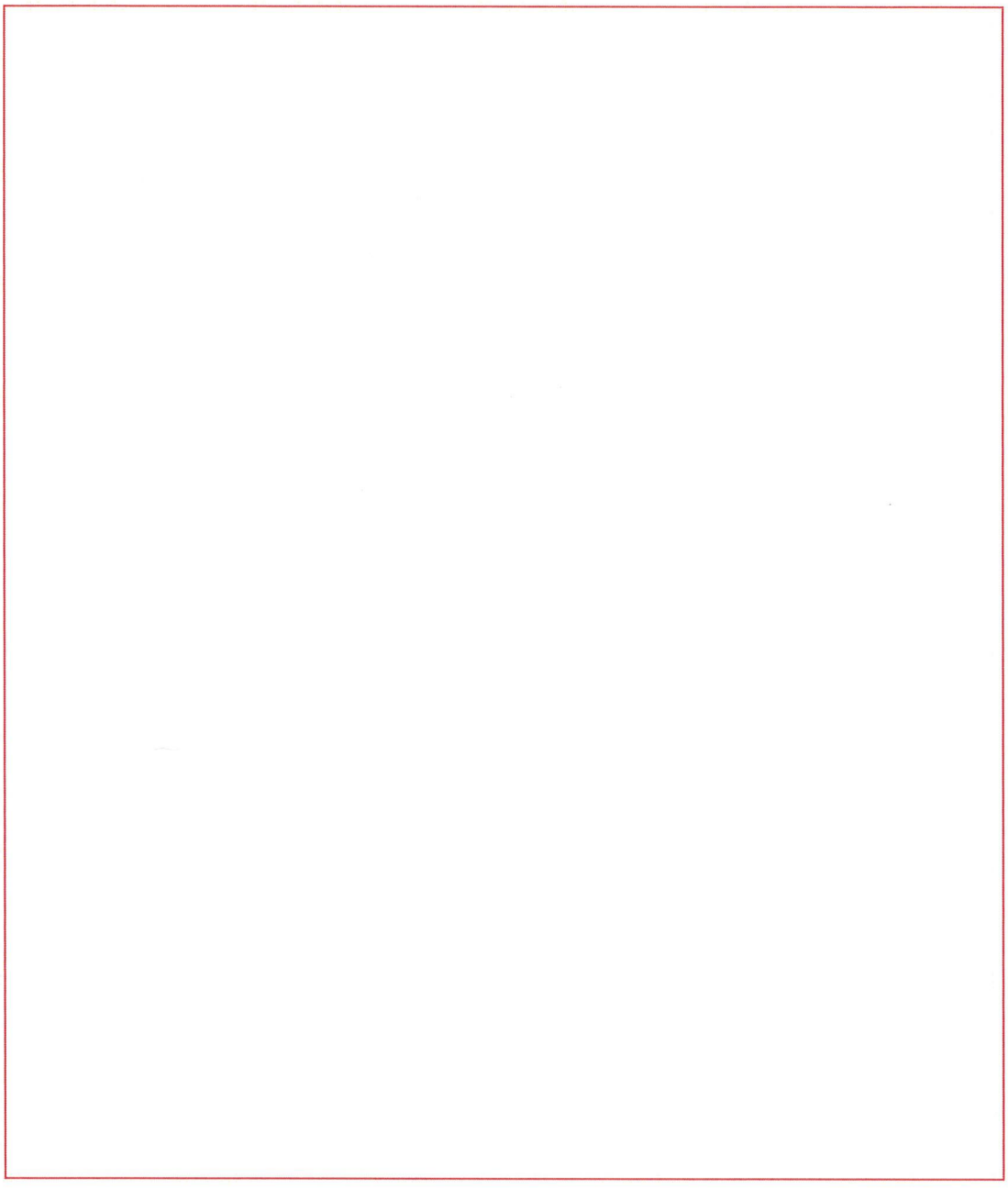

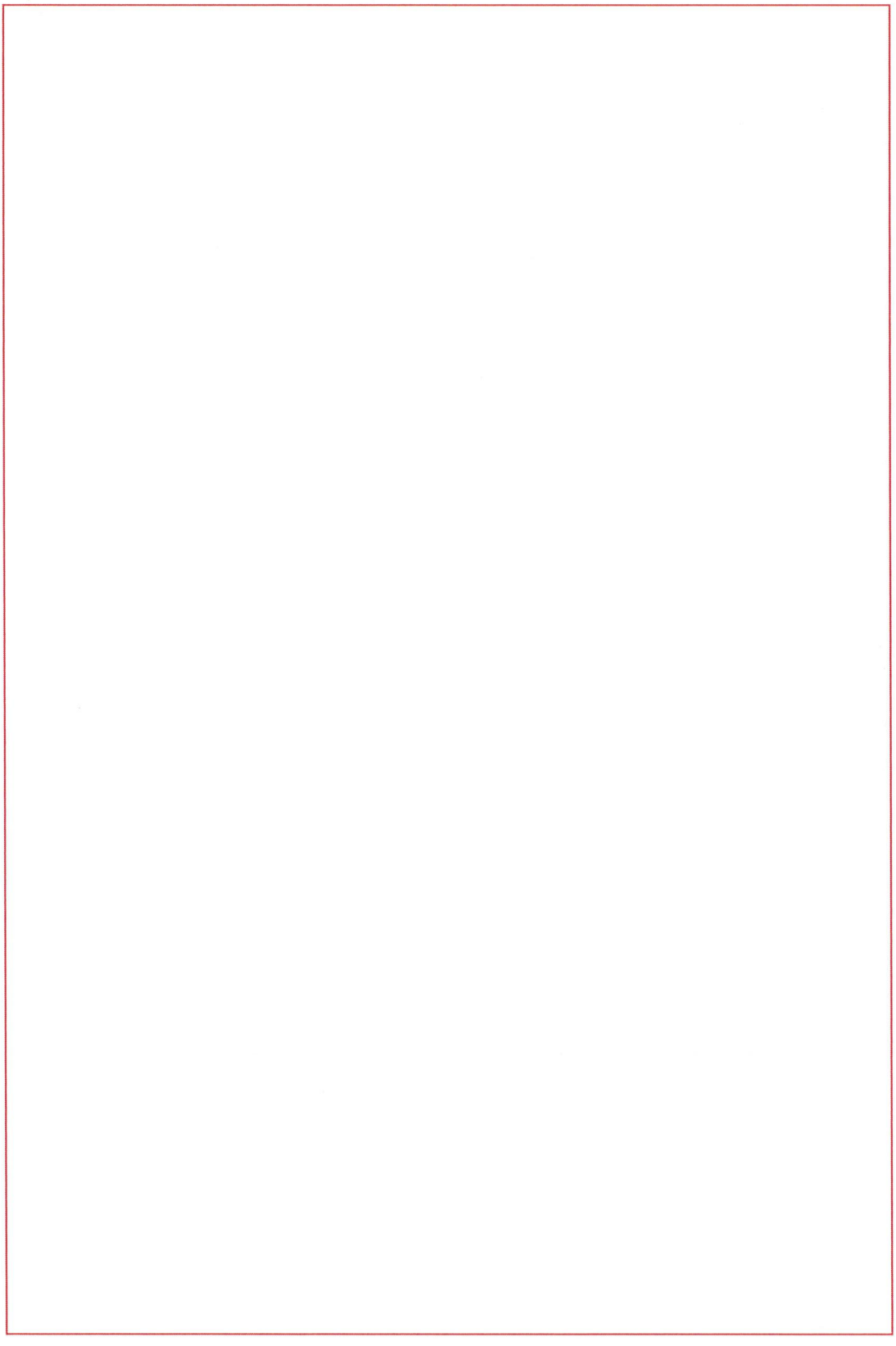

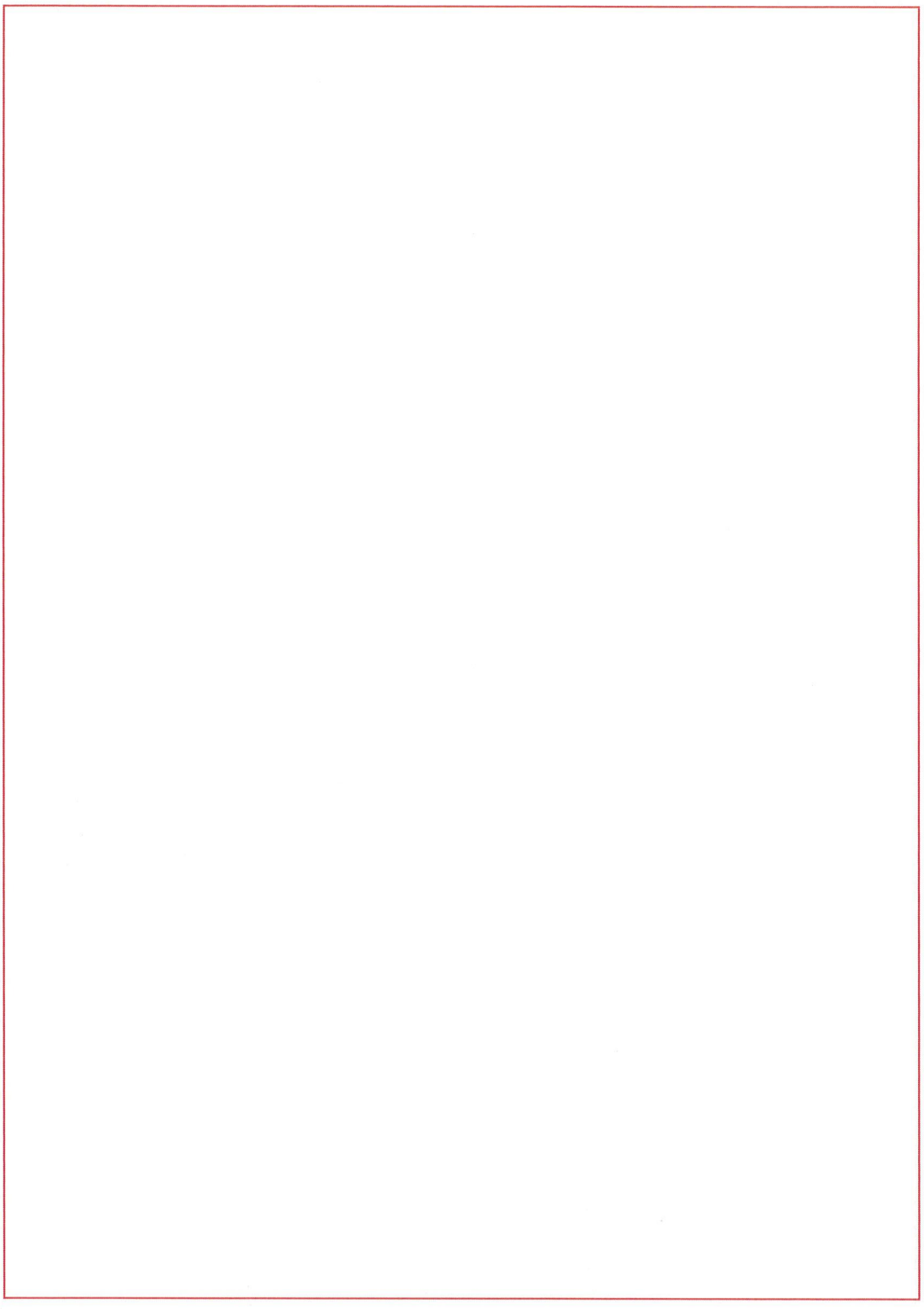

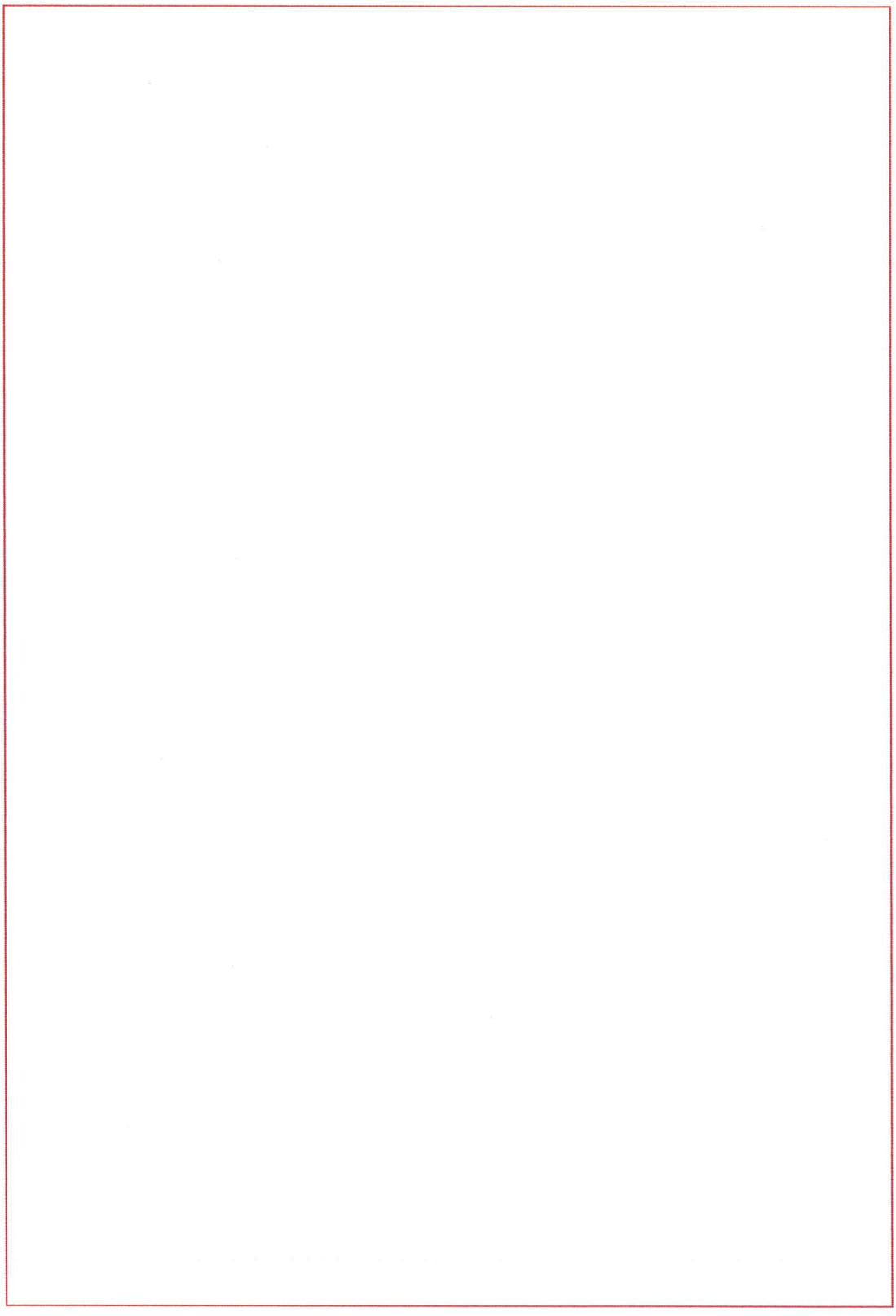

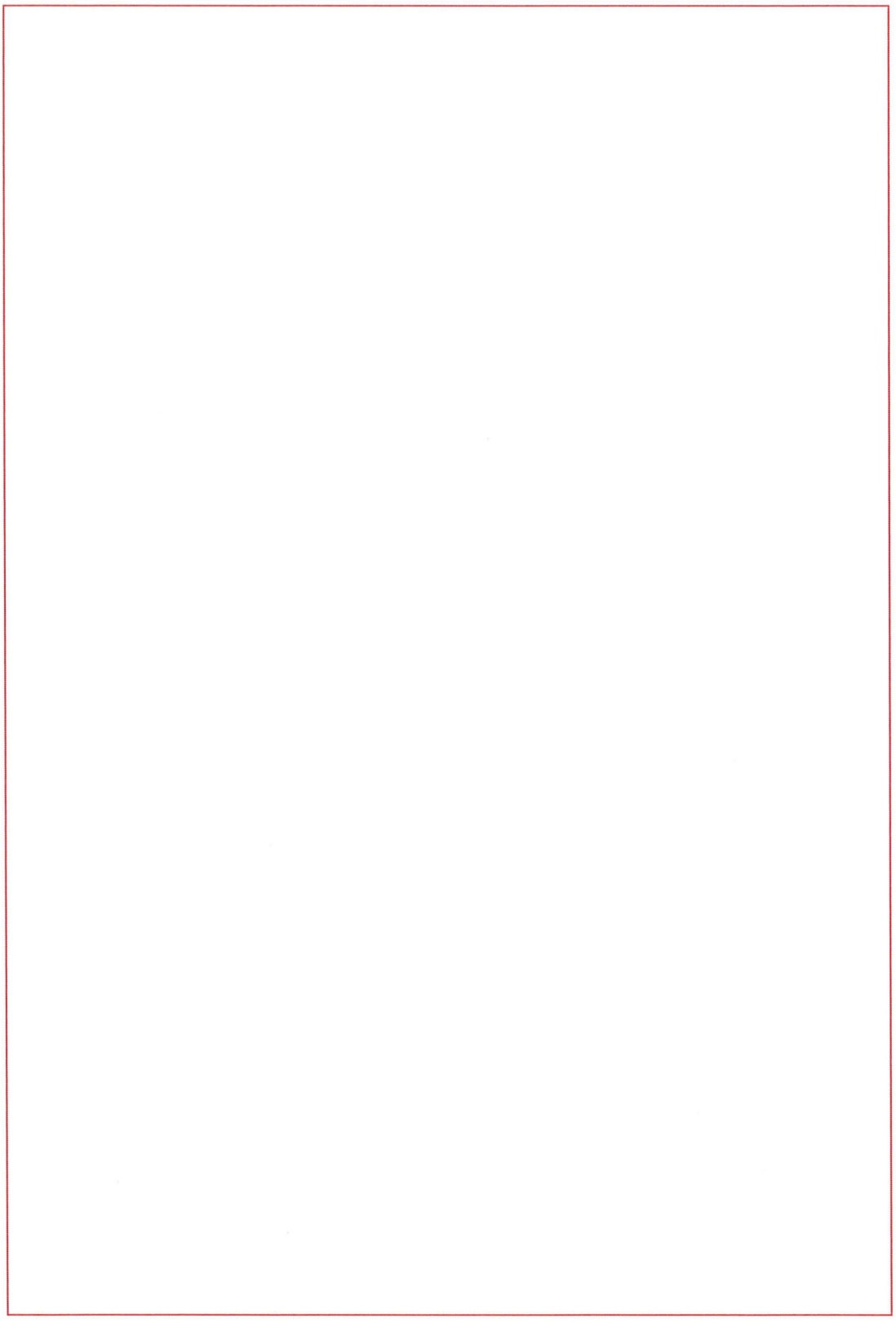

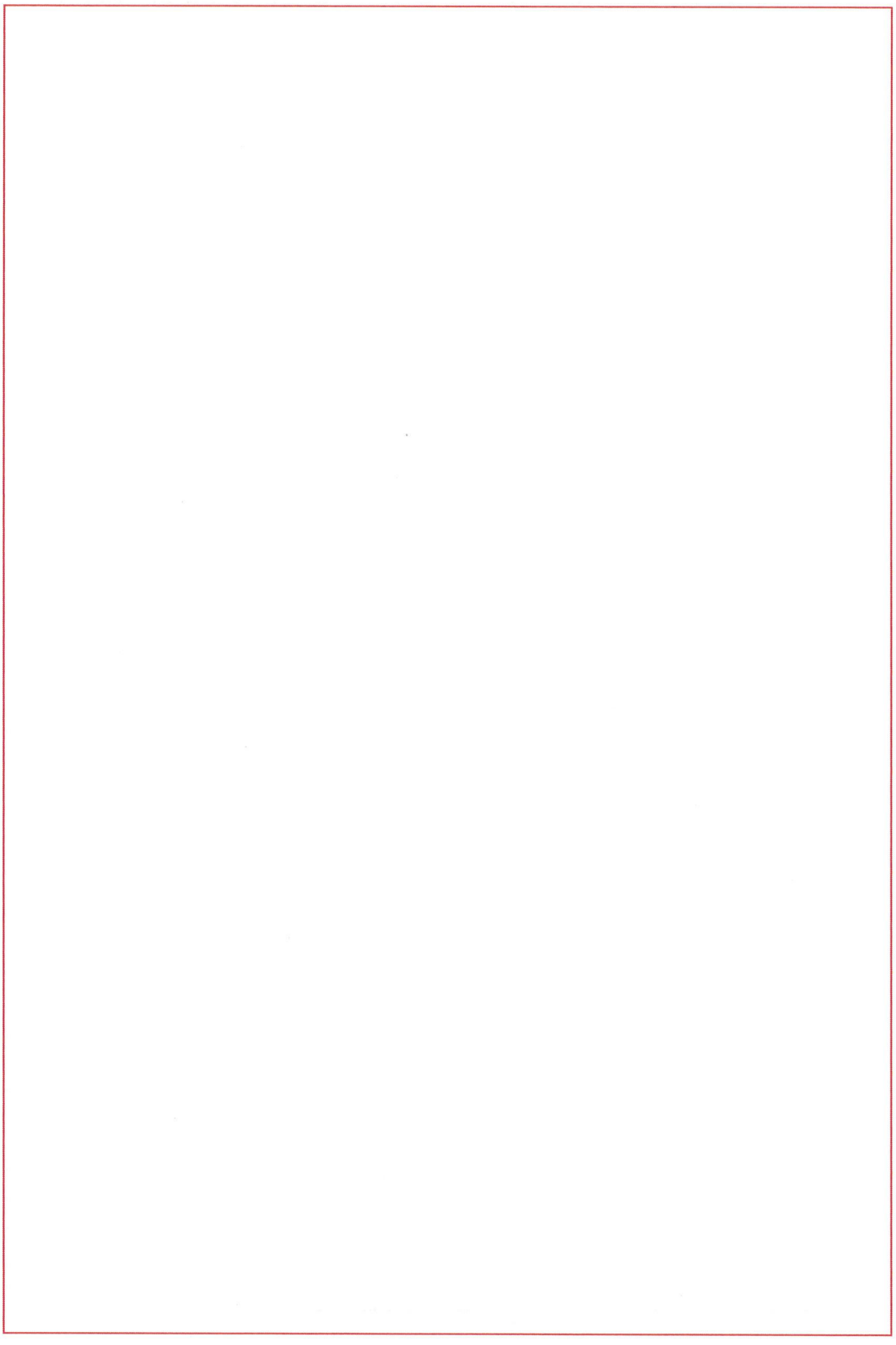

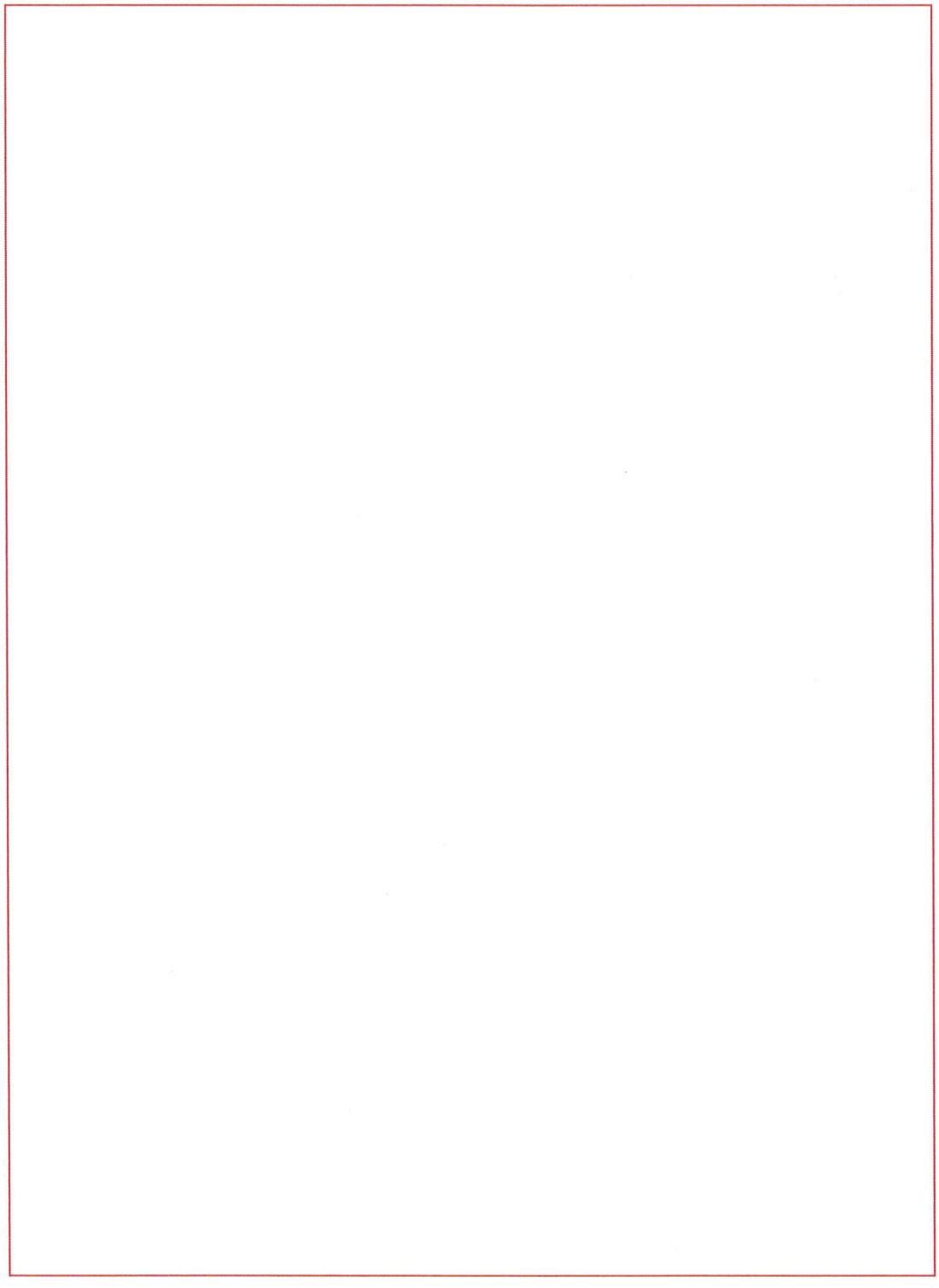

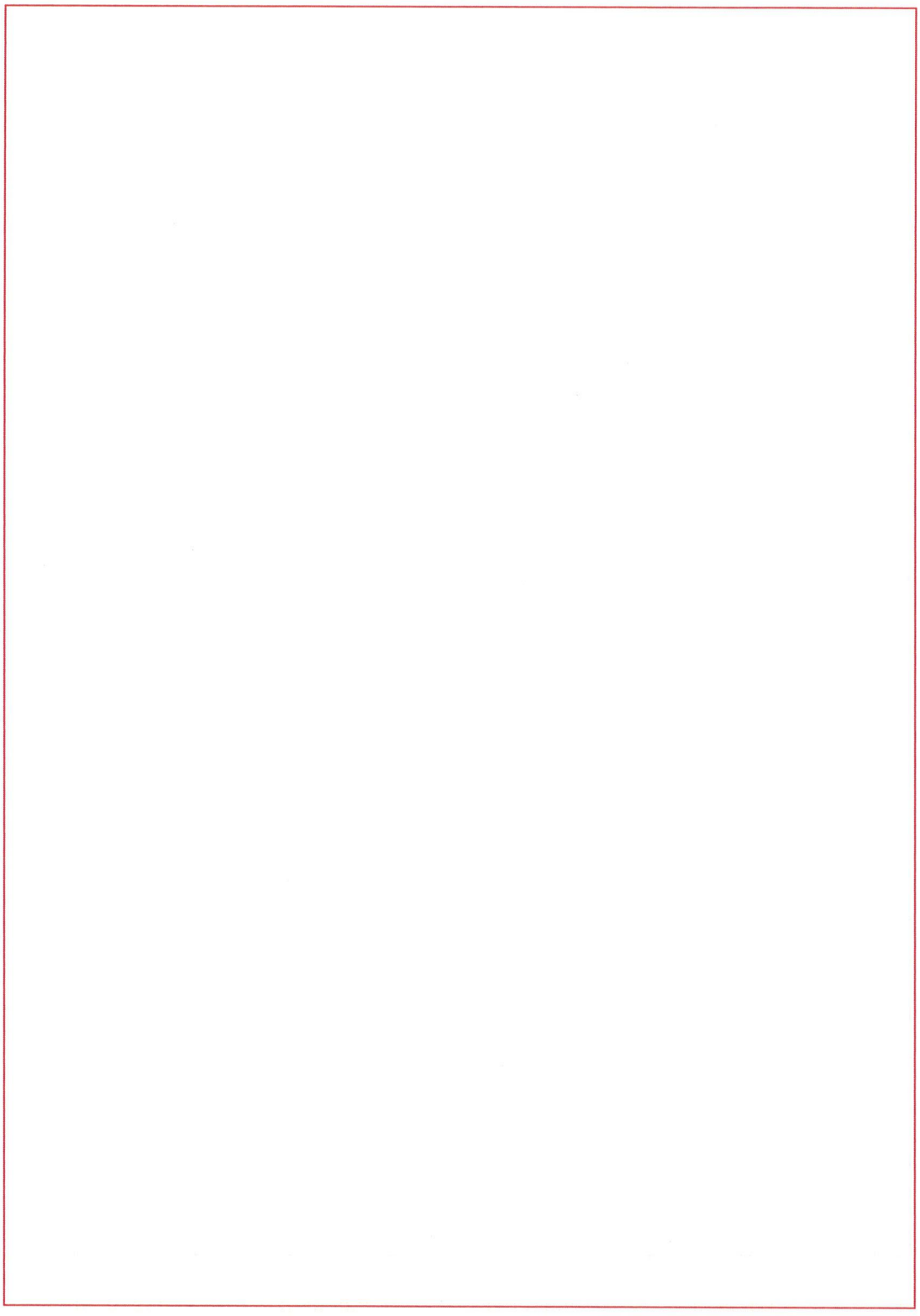

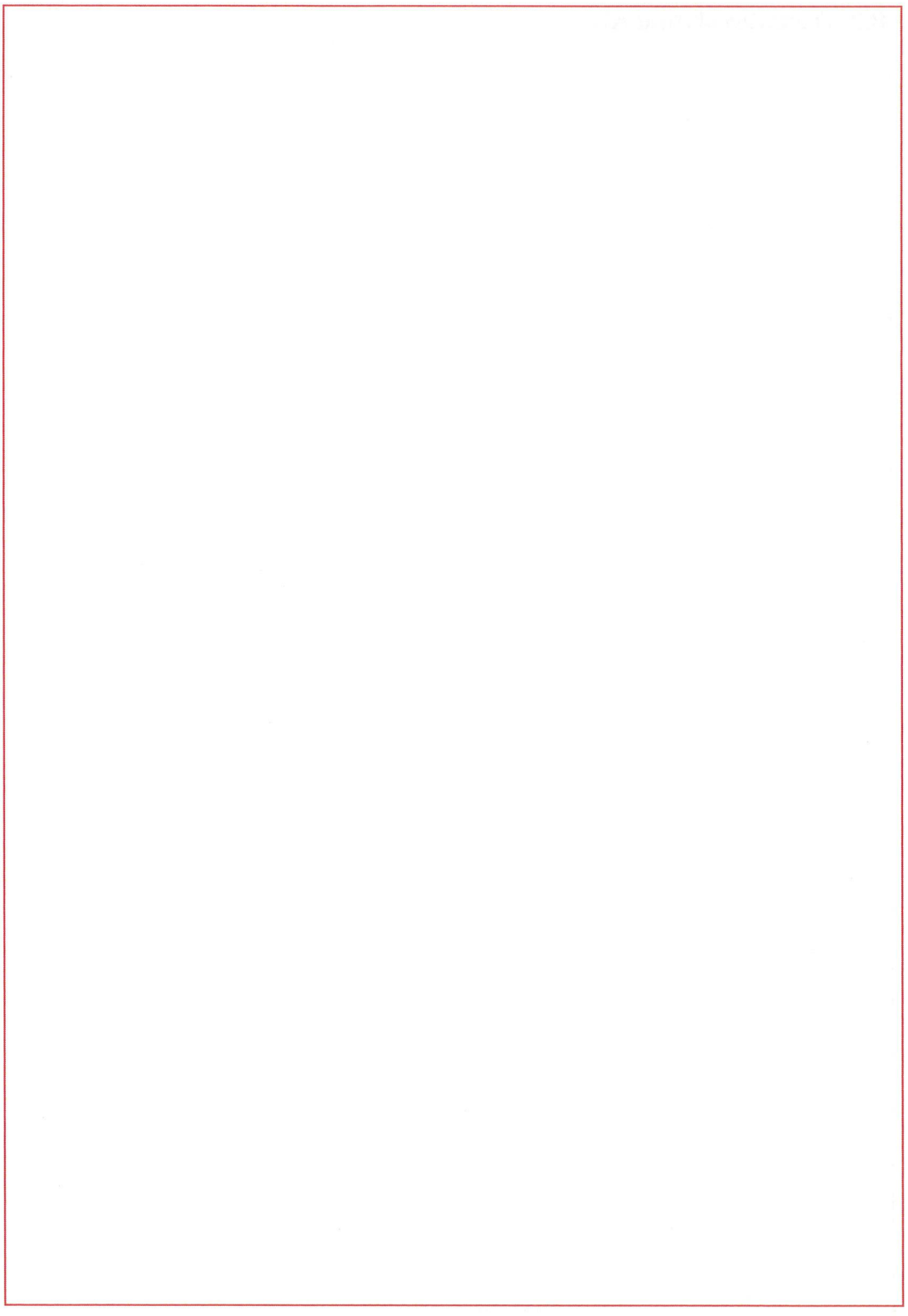

8.3. Transversal Analysis

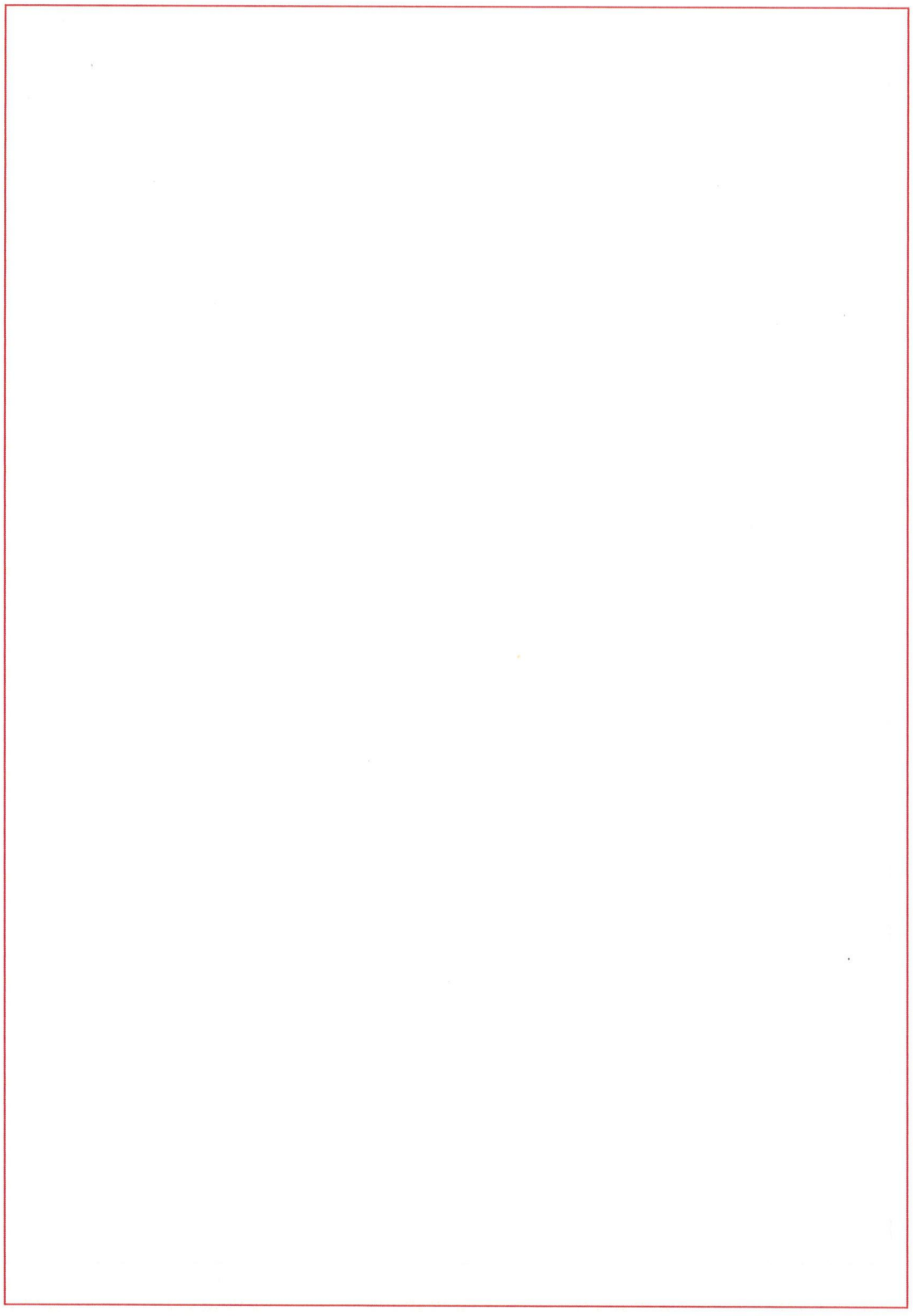

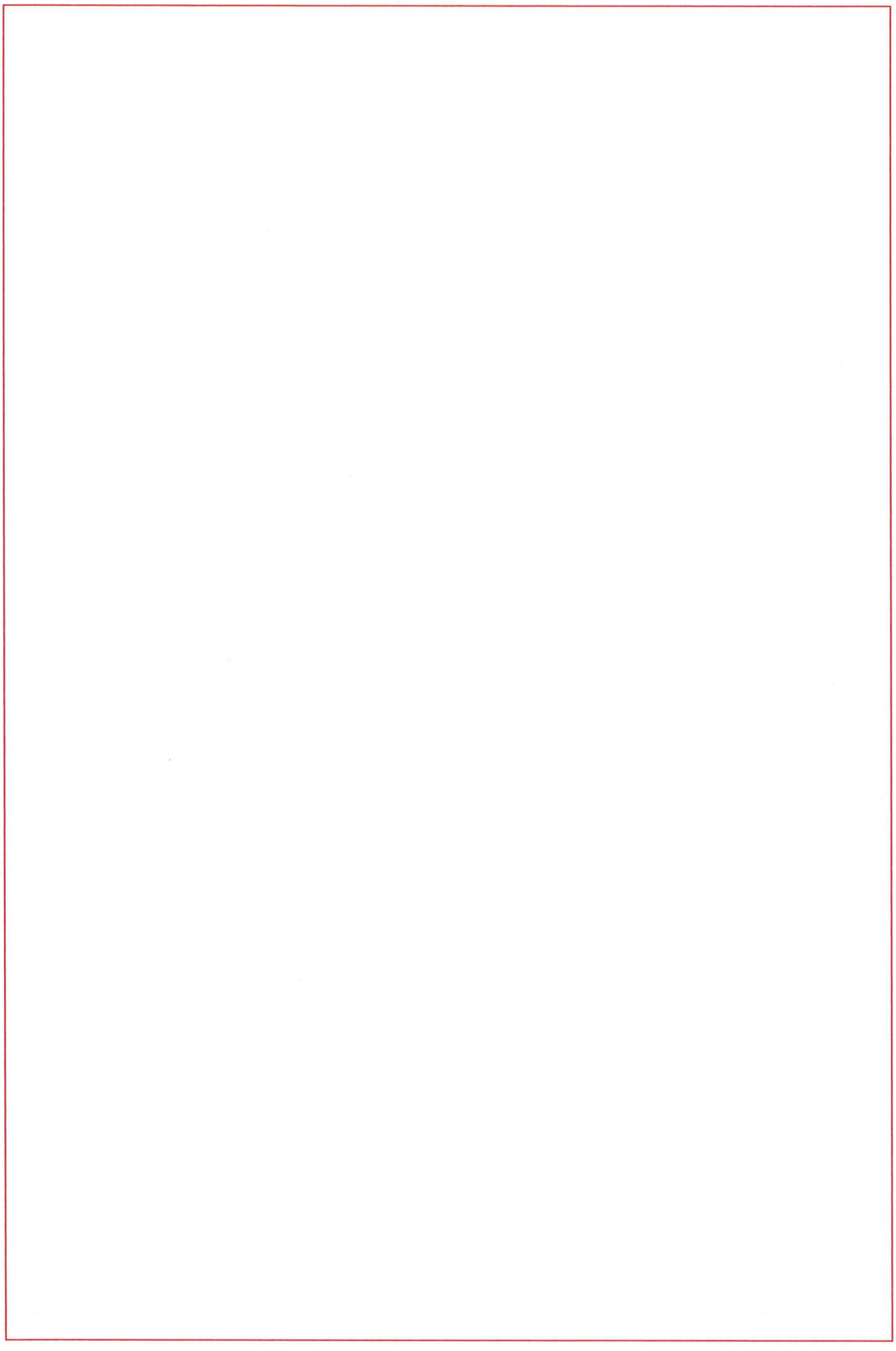

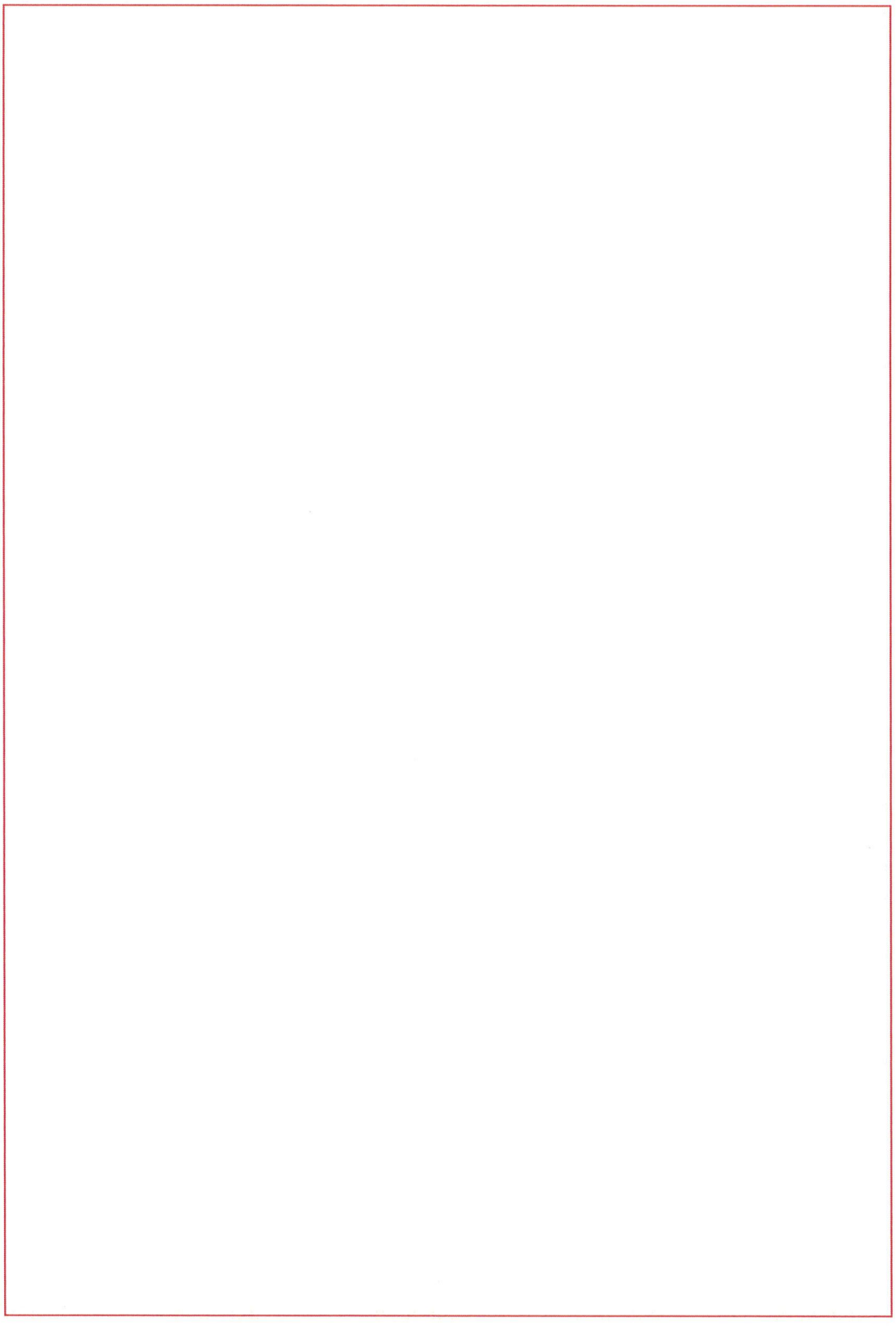

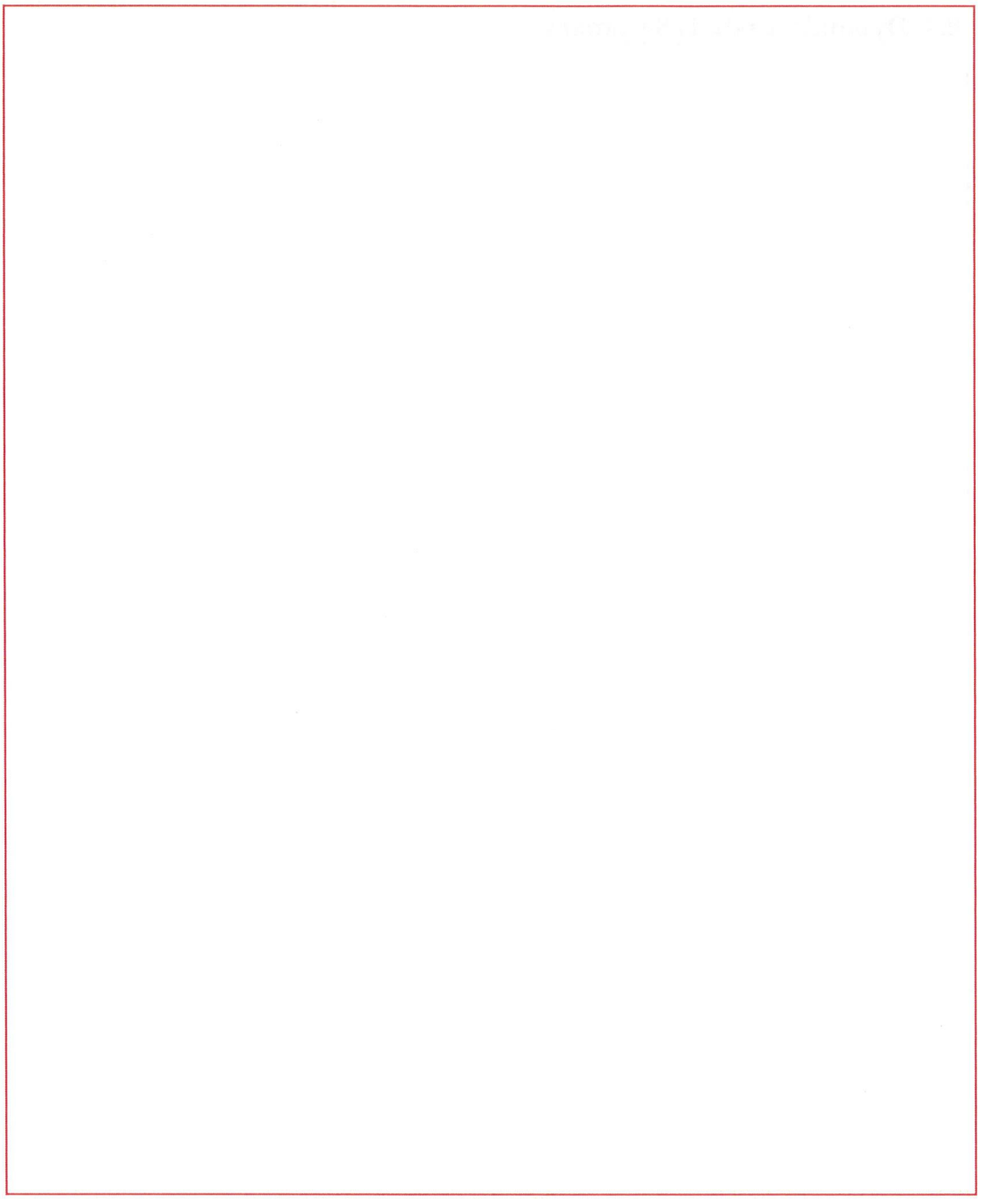

8.4. Dynamic Analysis Summary

9

Discussion and Recommendations

9.1. Design Spiral

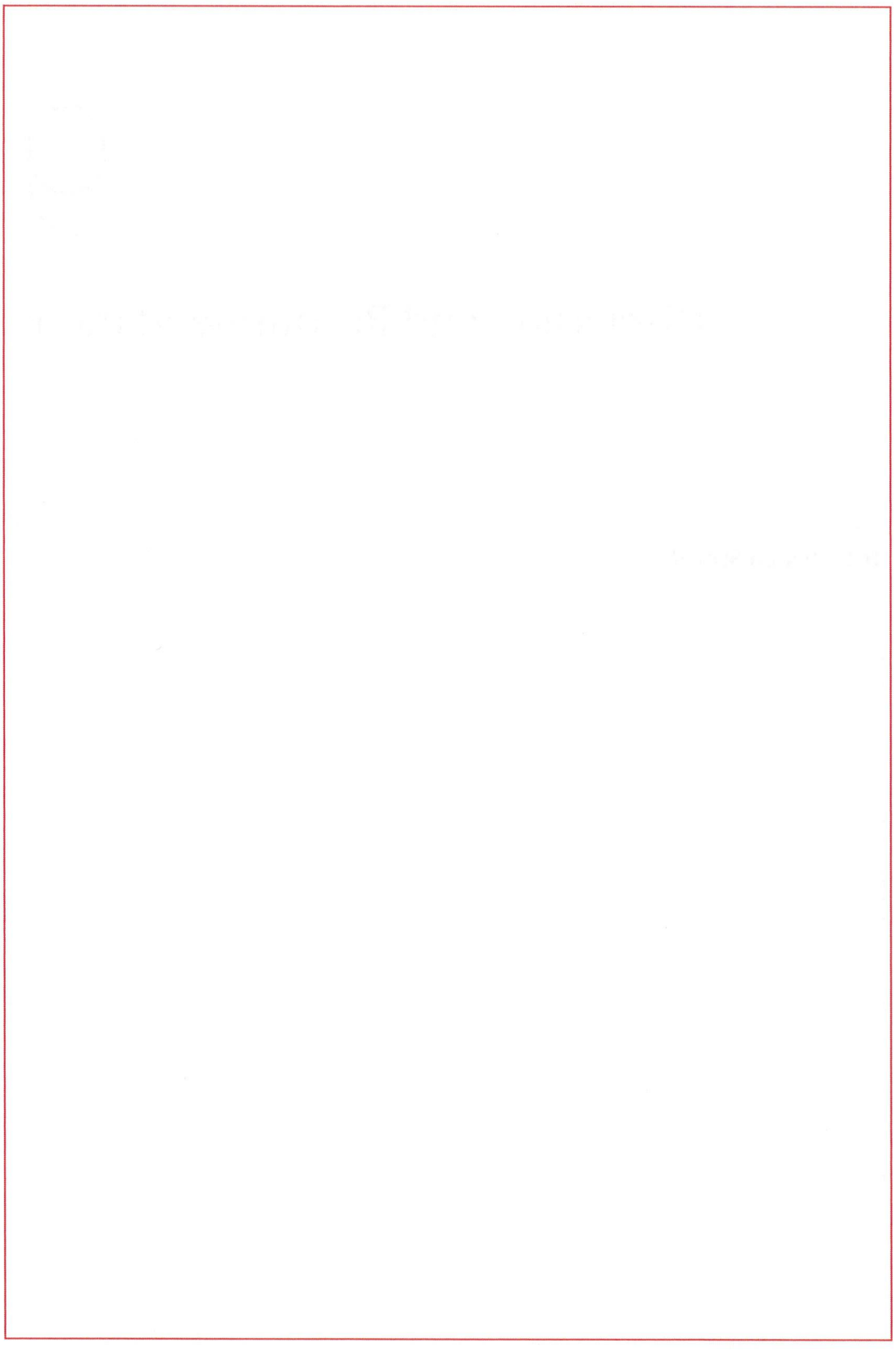

9.2. Splash Zone

9.3. Design Current

9.4. Modelling

9.5. Vortex-Induced-Vibrations

9.6. Seabed, Seafloor and Nodule Collector

9.7. Rotational Stability

9.8. Stationary Mining Method

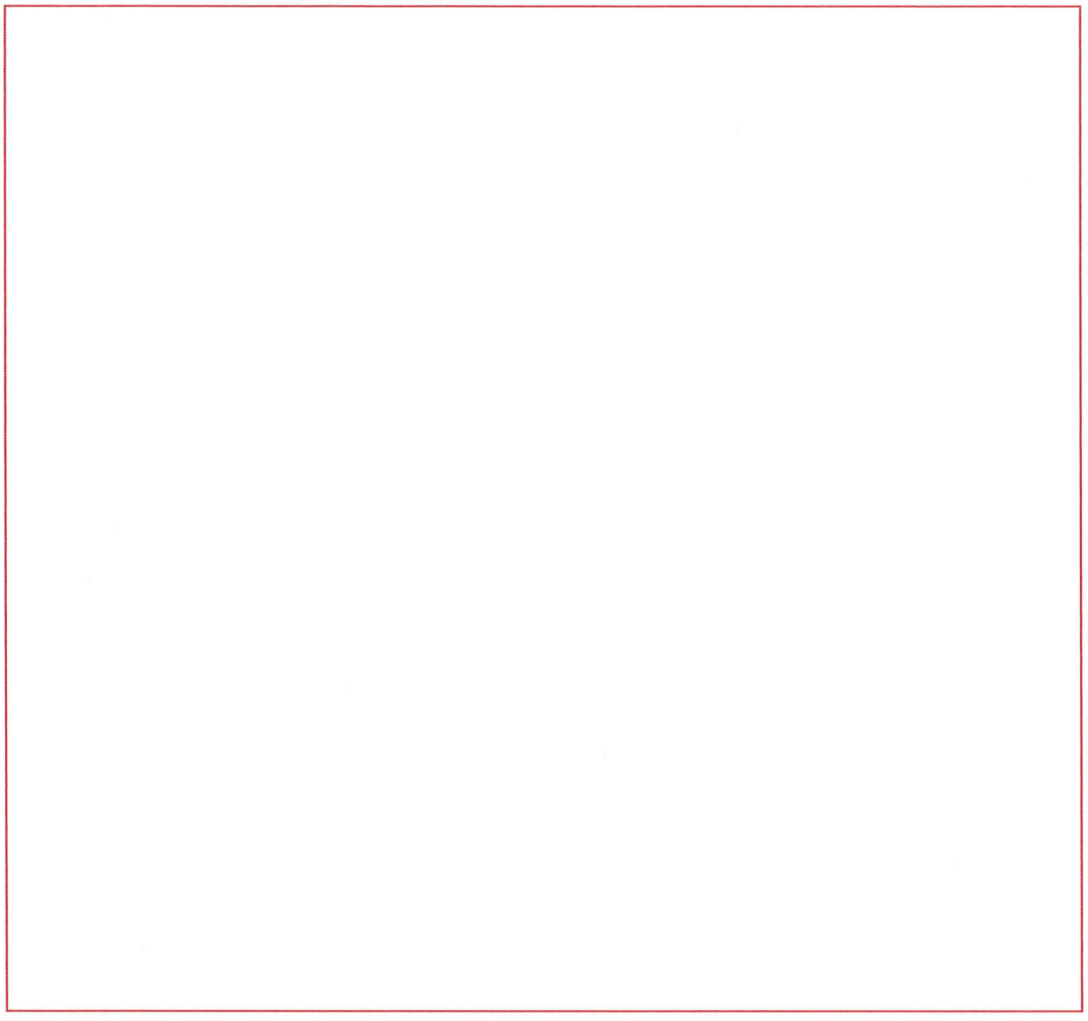

10

Conclusions

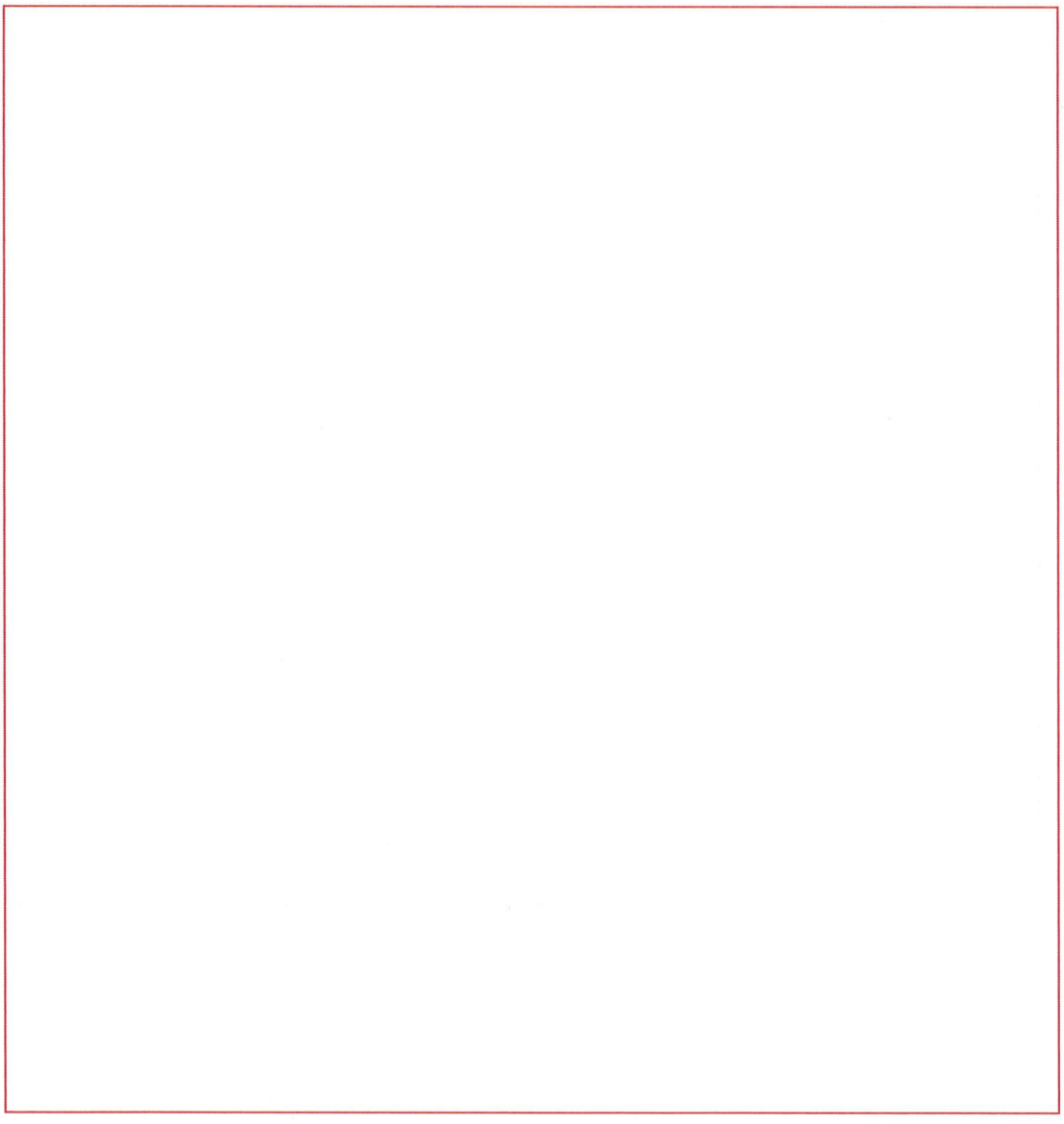

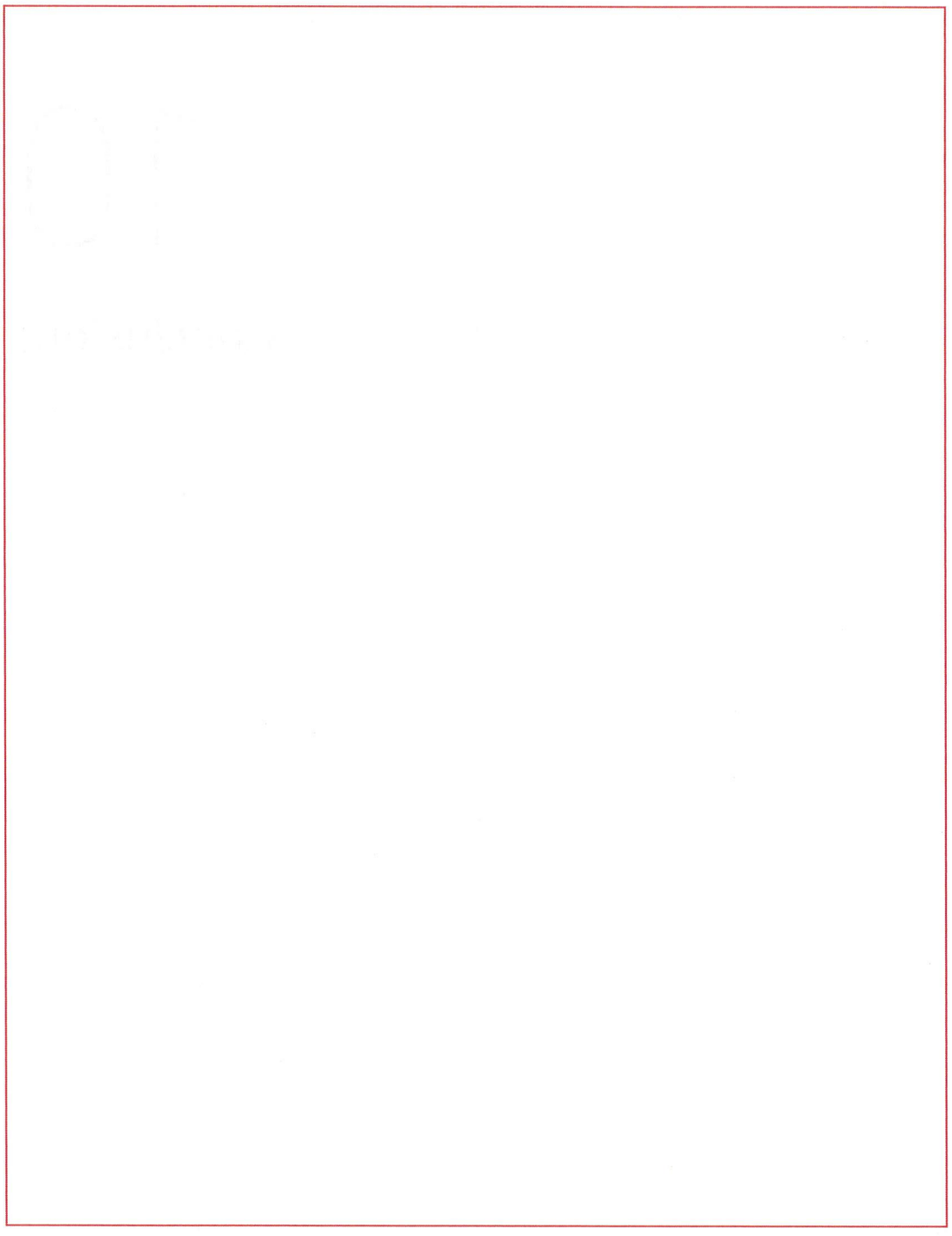

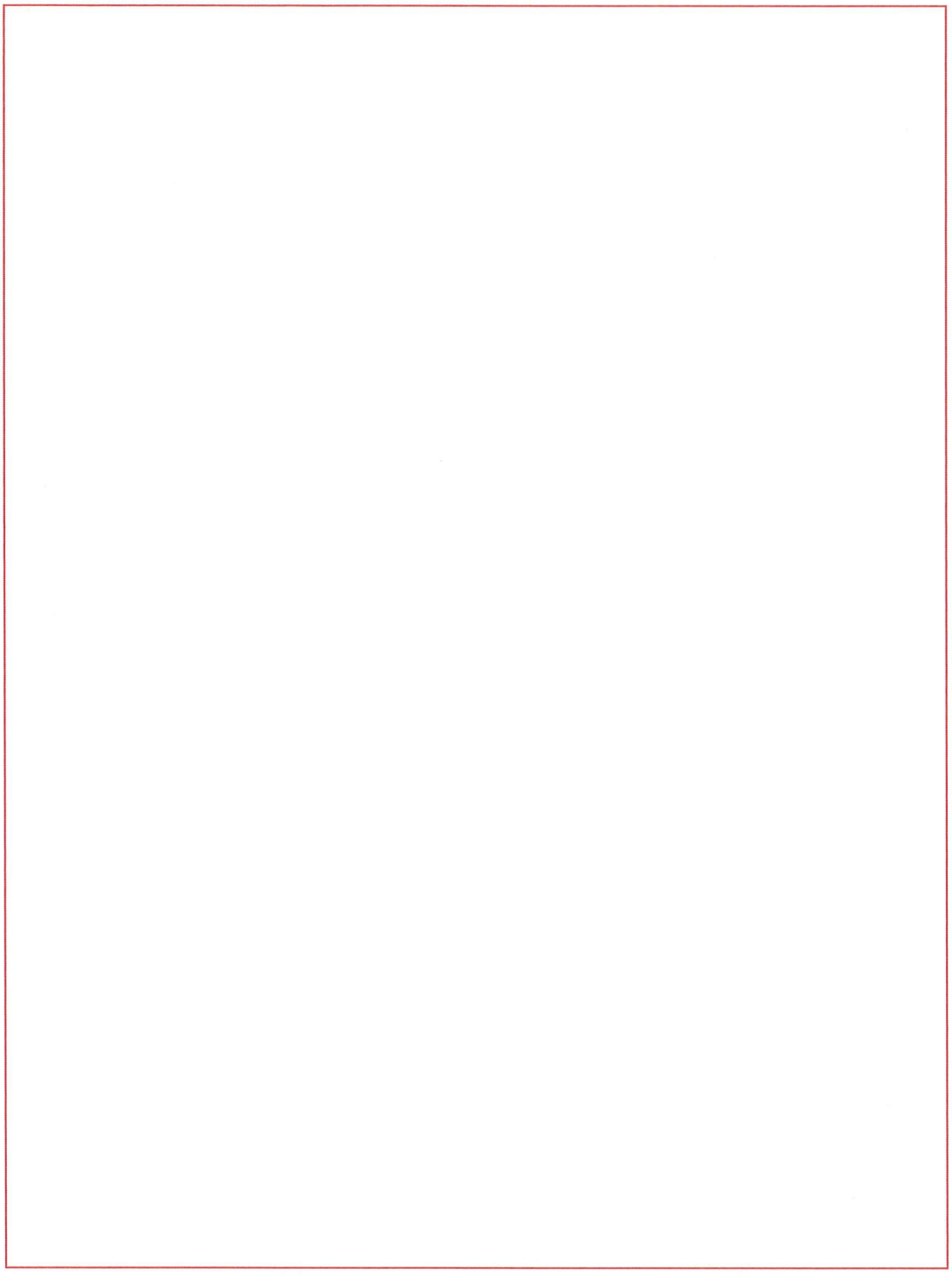

A

Polymetallic Nodule Properties

The polymetallic nodules are already introduced in Section 2.2.1 of Chapter 2. In this appendix a more detailed description is given, serving as input in further calculations. The polymetallic nodules can be best described as potato shaped objects lying on the seafloor. Most of the nodules are half buried under the sea-bottom sediment, sometimes even fully covered. As mentioned in Section 2.2.1, the nodule abundance is strongly correlated with the area examined. For the Clarion-Clipperton Zone the abundance is around 70%, which can be converted into an amount of 8 kg/m^2.

A.1. Physical Characteristics

Polymetallic- or manganese nodules can be best described as brown to black colored potato shaped objects lying on the abyssal planes of the deep ocean. Although most of the nodules have a size of approximately between $0.05m$ and $0.10m$, there is still a large variation in size and shape (from microscopic till $0.2m$). The nodule surface is on a large scale smooth, but zoomed in it tends more to rough. This property is strongly correlated to its composition, whereas nodules are highly porous (around 40%) with a large pore size and pore connectivity. This results to a high rate of permeability. When loaded as potato shaped objects in a cubic volume their void ratio is about 0.43 [-].

A.2. Density and Load Properties

In order to perform further calculations, we need to determine the weight of the nodules once loaded in the transportation skip; the bulk density. The bulk density is defined as the dry weight of soil of granulars per unit volume. Bulk density considers both the solids and the pore spaces (the voids). We distinguish two situations; above the waterline (in air) and beneath the waterline (submerged). We first consider the situation above the waterline. The dry solid density of the nodules for the Clarion-Clipperton Zone is around 1950 kg/m^3 [12]. The mean dry bulk density of polymetallic nodules is determined as approximately 1350 kg/m^3 [13]. When we consider a porosity of around 40% [12] and assume them to be fully saturated, the wet bulk density approaches 1652 kg/m^3. In a submerged situation for the same porosity, the submerged solid density of the nodules approaches 1335 kg/m^3, speaking in terms of pure nodule material. In calculating the density as material loaded in our transportation skip, we need to incorporate the void ratio of 0.43 [-]. The submerged bulk density will be 934.5 kg/m^3. A detailed overview of the derivation concerning the density is described in the following set of figures.

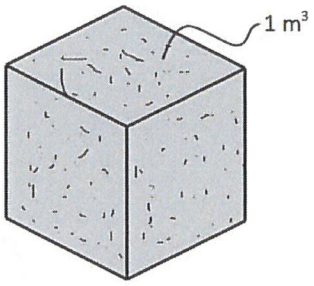

Figure A.1: Material - Pure dry

Pure dry nodule material

When considered a cubic shaped block of purely nodule material, we have the following properties:

Solid density: 1950 kg/m^3
Porosity: 40%

(60% of volume is solids, 40% of volume is air)

Mass (for a m^3): 1950 kg

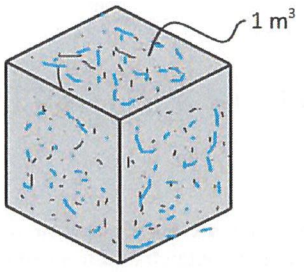

Figure A.2: Material - Pure wet

Pure wet nodule material

With a porosity of 40% and assumed fully saturated, we obtain the following properties:

Dry density: 1950 kg/m^3
Porosity: 40%

(60% of volume is solids, 40% of volume is water)

Water content (for a m^3) : $1 \cdot 1025 \cdot 0.4 = 410$ kg

Mass (for a m^3): $1950 + 410 = 2360$ kg

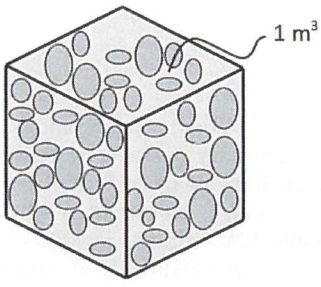

Figure A.3: Nodules dry bulk

Dry nodules loaded

Once loaded as potato shaped objects into a cubic shape results into a nodule/air ratio of:

Voids ratio = $\frac{V_{air}}{V_{nodules}} = \frac{0.3}{0.7} = 0.43$

(70% of V in cubic is nodules, 30% of V in cubic is air)
(60% of V nodules is solids, 40% of V nodules is air)

Dry bulk density: $1950 \cdot 0.7 = 1365$ kg/m^3

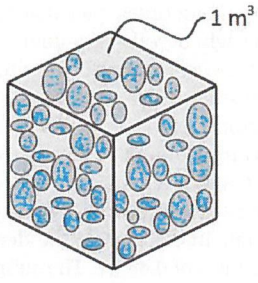

Figure A.4: Nodules wet bulk

Wet nodules loaded

Whereas the nodules have a porosity of 40% and will be assumed fully saturated, wet loaded nodules have the following properties:

(70% of V in cubic is nodules, 30% of V in cubic is air)
(60% of V nodules is solids, 40% of V nodules is water)

Dry Mass (for a m^3): $2000 \cdot 0.7 = 1365$ kg

Water content: $1 \cdot 1025 \cdot 0.7 \cdot 0.4 = 287$ kg

Wet bulk density $1365 + 287 = 1652$ kg/m^3

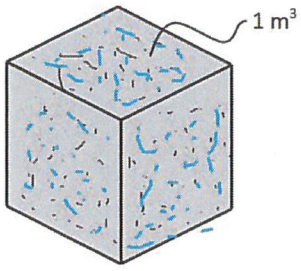

Figure A.5: Submerged pure nodule material

Pure Submerged nodule material

With a porosity of 40% and assumed fully saturated we obtain the following property for pure wet nodule material:

(60% of volume is solids, 40% of volume is water)
(The 60% solids encounter buoyancy effect)

Dry density: 1950 kg/m^3
Buoyancy: $1025 \cdot 0.6 = 615\ kg$

Submerged solid density (for a m^3): 1950 - 615 = 1335 kg/m^3

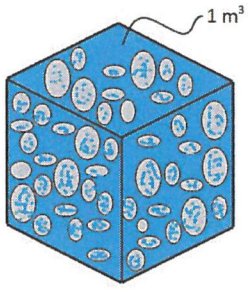

Figure A.6: Submerged loaded nodules

Submerged nodules loaded

With a porosity of 40% and assumed fully saturated we obtain the following property for pure wet nodule material:

(70% of V in cubic is nodules, 30% of V in cubic is water)
(60% of V nodules is solids, 40% of V nodules is water)

Submerged bulk density : $1335 \cdot 0.7 = 934.5\ kg/m^3$

B

Proposed Production Cycle

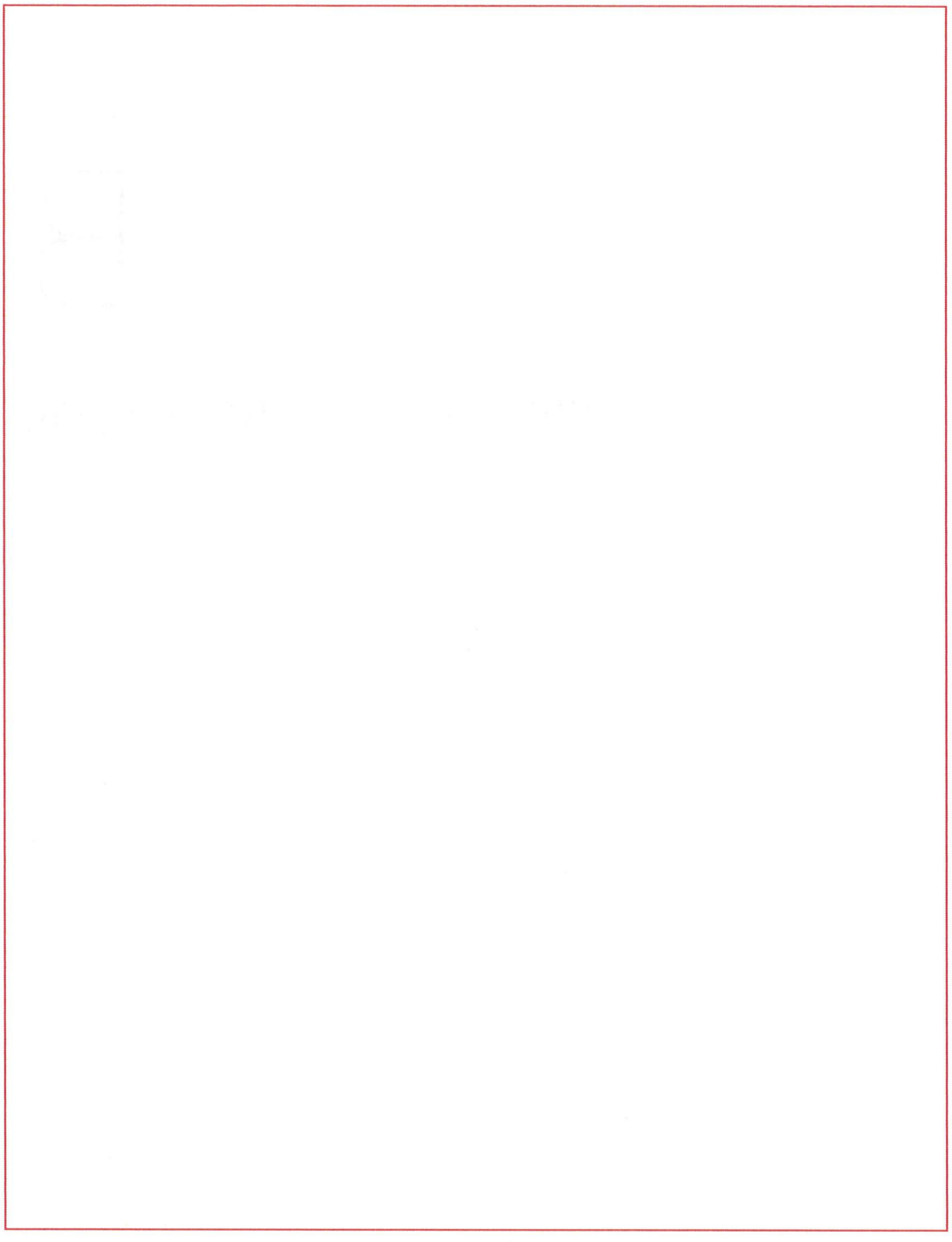

C

Wind, Wave and Current

C.1. Wave Statistics

93.5 %

H_{m0} [m]	T_p [Sec] 0-2	2-4	4-6	6-8	8-10	10-12	12-14	14-16	16-18	18-20	>20	Total [%]
0-0.5	0%	0%	0%	0%	0%	0%	0%	0%	0%	0%	0%	0%
0.5-1	0%	0%	0%	0%	0.00%	0.02%	0.04%	0.00%	0%	0%	0%	0.07%
1-1.5	0%	0%	0.02%	0.50%	1.91%	2.94%	4.29%	1.23%	0.55%	0.12%	0.00%	11.57%
1.5-2	0%	0%	0.10%	1.57%	4.55%	8.76%	17.98%	8.06%	2.95%	0.64%	0.03%	44.64%
2-2.5	0%	0%	0.08%	0.70%	1.71%	4.18%	11.65%	7.16%	2.63%	0.65%	0.08%	28.85%
2.5-3	0%	0%	0.01%	0.34%	0.73%	0.71%	3.80%	3.15%	1.27%	0.31%	0.03%	10.35%
3-3.5	0%	0%	0.00%	0.15%	0.46%	0.12%	0.71%	1.12%	0.47%	0.08%	0.01%	3.13%
3.5-4	0%	0%	0%	0.04%	0.18%	0.08%	0.07%	0.29%	0.13%	0.02%	0.00%	0.81%
4-4.5	0%	0%	0%	0.01%	0.08%	0.05%	0.01%	0.07%	0.08%	0.01%	0.00%	0.32%
4.5-5	0%	0%	0%	0.01%	0.03%	0.02%	0.01%	0.03%	0.01%	0.01%	0%	0.11%
5-5.5	0%	0%	0%	0%	0.02%	0.02%	0.01%	0.01%	0%	0%	0%	0.06%
5.5-6	0%	0%	0%	0%	0.01%	0.01%	0.01%	0%	0%	0%	0%	0.03%
6-6.5	0%	0%	0%	0%	0.00%	0.02%	0%	0%	0%	0%	0%	0.02%
6.5-7	0%	0%	0%	0%	0%	0.01%	0%	0%	0%	0%	0%	0.01%
7-7.5	0%	0%	0%	0%	0%	0.00%	0.00%	0%	0%	0%	0%	0.01%
7.5-8	0%	0%	0%	0%	0%	0.00%	0%	0.00%	0%	0%	0%	0.00%
>8	0%	0%	0%	0%	0%	0.01%	0.01%	0.00%	0%	0%	0%	0.03%
Total [%]	0%	0%	0.22%	3.33%	9.68%	16.97%	38.60%	21.13%	8.09%	1.84%	0.15%	100.0%

Figure C.1: Annual wave scatter diagram

The annual wave scatter plot of the previous diagram is given in Figure C.2.

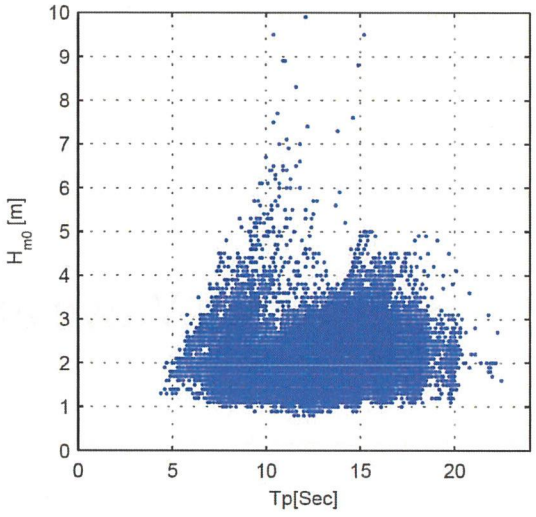

Figure C.2: Annual wave scatter

The probability of exceedance plot for the same location is given in Figure C.3.

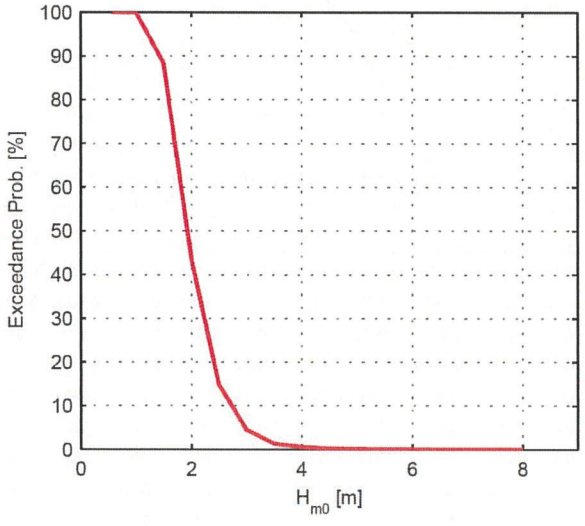

Figure C.3: Probability of exceedance

C.2. Wind Statistics

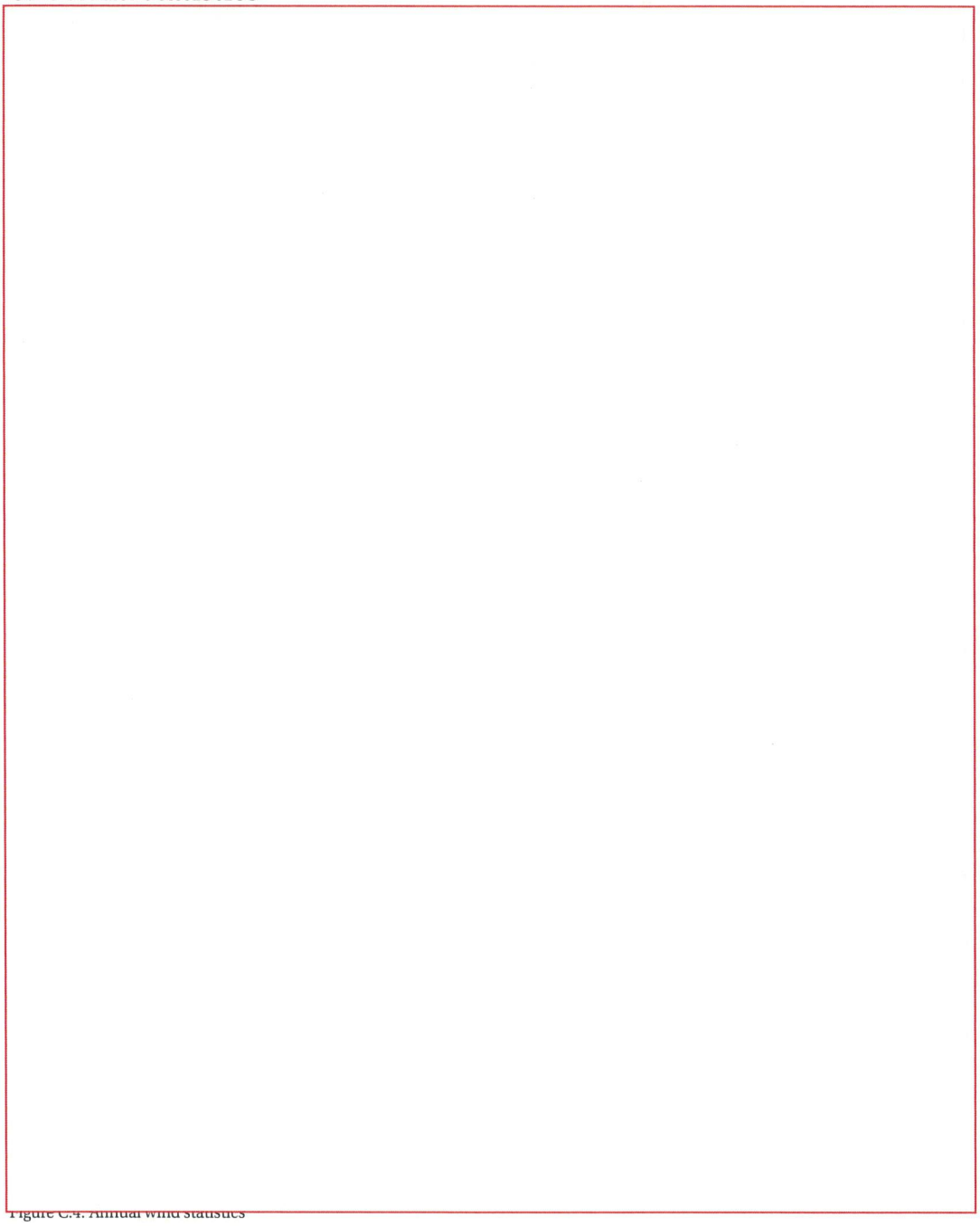

Figure C.4: Annual wind statistics

C.3. HYCOM® Data

D

Static Model - Derivation and Validation

This appendix is dedicated to the derivation and validation of the static model. During the static analysis in Chapter 6, the model formed the foundation of all calculations. First the origin of the approach, based on a discretized catenary shaped function, is introduced. This same approach is applied to a suspended wire in a uniform current. Finally, the technique to connect multiple wires is explained in more detail. This connection is in the end the motivator for the numeric approach. Connected wire shapes can be determined analytically [14], but applying numerics is more pragmatic and therefore convenient.

D.1. Catenary

The origin of the approach is founded in the succes of discretizing a catenary shaped wire. A catenary can be defined as a flexible chain or wire hanging between two fixed points. Its shape looks parabolic but is in fact a catenary. First the analytical derivation of the wire shape will be introduced and afterwards the numerical . In the validation section, the results of both approaches will be compared.

D.1.1. Analytical

In Figure D.1 a schematic representation of a catenary is given. In this situation we will consider the lowest part of the chain to be located at the origin of the axis system. The wire has a linear constant density, which practically means that the weight of the wire with respect to the origin *(0,0)* increases linearly. The weight (per unit length) is based on the mass per unit length and gravitational acceleration ($w = mg$). The magnitude of the weight at a random point along the arc length is therefore a result of the distance (length) s times the weight per unit length. This weight results into a tension T, which is always tangential to the wire shape. At the origin, the tension equals its horizontal component (tangent is zero) and is therefore denoted as T_0

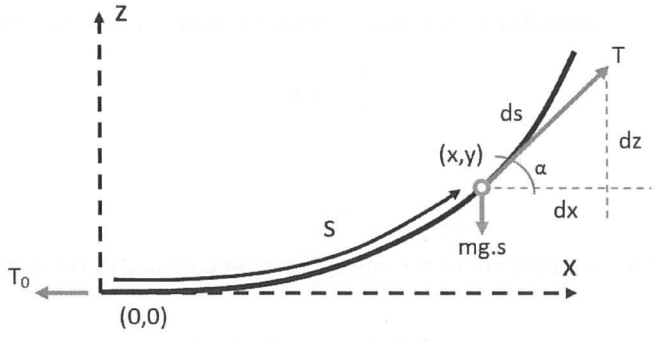

Figure D.1: Catenary - Equilibrium of forces

We will now focus on the arbitrary point (*x,y*). If we describe this point as a differential element, the forces can be expressed in three contributions; the weight of the wire in point (*x,y*), the tension in point (*x,y*) and the horizontal component of the tension (which is T_0). This equilibrium can be described in x- and y-direction using the following relationship:

$$\begin{aligned} T_0 &= T\cos\alpha \\ mg\cdot s &= T\sin\alpha \end{aligned} \tag{D.1}$$

To reduce the number of unknowns, the tensions T can be eliminated using the following geometric property:

$$\frac{T\sin\alpha}{T\cos\alpha} = \tan\alpha = \frac{mg\cdot s}{T_0} = as \tag{D.2}$$

Where a is introduced for convenience:

$$a = \frac{mg}{T_0} \tag{D.3}$$

Using the geometric relationship between the delta's, Eq-D.2 can be rewritten as:

$$\frac{dz}{dx} = as \tag{D.4}$$

In order to write the wire shape explicitly in terms of x and z, the s should be eliminated. This can be done by applying the Pythagoras' theorem for the lengths of the legs of the differential element:

$$ds^2 = dx^2 + dz^2 \tag{D.5}$$

If we first differentiate Eq-D.4, the Pythagoras relation can be substituted for *ds*. The result is:

$$\frac{d^2z}{dx^2} = a\cdot\frac{ds}{dx} = a\cdot\frac{\sqrt{dx^2+dz^2}}{dx} \tag{D.6}$$

The differential equation of the catenary now reads:

$$\frac{d^2z}{dx^2} = a\cdot\sqrt{1+\left(\frac{dz}{dx}\right)^2} \qquad with \quad a = \frac{mg}{T_0} \tag{D.7}$$

This differential equation can be easily solved using the separation of variables principle (in two steps). In the end we obtain the following explicit equation for the catenary shape:

$$z(x) = \frac{1}{a}\cdot cosh(ax) + C \qquad where \quad a = \frac{mg}{T_0} \tag{D.8}$$

The constant of integration can be determined by applying the boundary condition at *z(0)=0*:

$$z(0) = 0 = \frac{1}{a}\cdot cosh(0) + C \tag{D.9}$$

Therefore

$$C = -\frac{1}{a} \tag{D.10}$$

When solved explicitly for z as function of x we obtain the following analytical expression for an inextensible catenary shaped wire:

$$z(x) = \left(\frac{T_0}{mg}\right)\cdot\left\{cosh\left(\frac{mg\cdot x}{T_0}\right) - 1\right\} \tag{D.11}$$

In which T_0 is the horizontal tension component and mg the self-weight per unit length of the wire.

D.1.2. Numerical

In the numerical approach we divide the length of wire L in a number of elements n (discretization), with an element length dS. This automatically yields into a number of nodes of size $n+1$. The i indicates the node number starting from the tip of the wire. These nodes are the points where acting wire forces per segment will be concentrated. The horizontal force in the catenary shape is constant along the length of wire (in every node). This means that the magnitude of $F_{h;tip}$ is equal to $F_{h;top}$. The vertical force per node increases per element as a function of the self-weight and wire length, starting from the tip. This practically means that $F_{v;top}$ equals the entire weight of the wire. The tension in each node is composed out of the horizontal and vertical component and can simply be calculated using Pythagoras' theorem:

$$T(i) = \sqrt{(F(i)_x)^2 + (F(i)_y)^2} \tag{D.12}$$

In this section we will take the elongation of the wire into account. Here the tension is required to obtain the elongation of each element as a result of the forces. This can be expressed as:

$$dL(i) = dS \cdot \left(1 + \left(\frac{T(i)}{EA}\right)\right) \tag{D.13}$$

The cartesian coordinates of each node can be determined by the geometric relation between the vertical and horizontal forces. This ratio of forces will first result into an angle in each node. The angle of the complete segment is composed out of the angles of both its adjacent nodes divided over two. When combined in one formula for x- and z- coordinates one obtains:

$$x(i) = x(i-1) + \left\{dS \cdot \left(1 + \left(\frac{T(i)}{EA}\right)\right)\right\} \cdot cos\left(\frac{\theta(i) + \theta(i-1)}{2}\right) \tag{D.14}$$

$$z(i) = z(i-1) + \left\{dS \cdot \left(1 + \left(\frac{T(i)}{EA}\right)\right)\right\} \cdot sin\left(\frac{\theta(i) + \theta(i-1)}{2}\right) \tag{D.15}$$

To change the origin from tip to top of the wire, one can easily subtract the value for the last coordinate:

$$\begin{aligned} x'(i) &= x(i) - x(end) \\ z'(i) &= z(i) - z(end) \end{aligned} \tag{D.16}$$

D.1.3. Validation

The numerical approach is validated by comparing its output with the analytical results. The accuracy increases when the step size in the discretization is decreased (smaller segments). The stiffness of the numerical model is set infinite to create an inextensible wire. The following input parameters were used:

L	100	[m]	**mg**	275.5	[N/m]
EA	∞	[-]	$\mathbf{T_0}$	10^4	[kN]

The results are shown in Figure D.2.

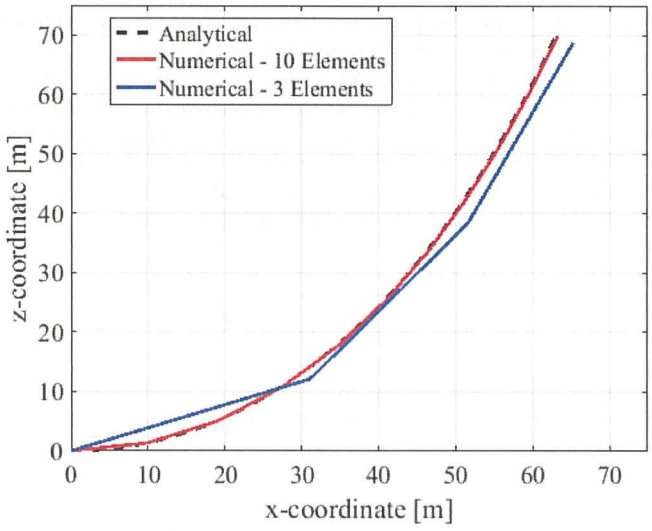

Figure D.2: Comparison analytical and numerical output

D.2. Suspended Wire

In describing the static configuration of a suspended wire in a uniform flow, a similar approach can be applied. The self-weight of the wire is still present and the drag contribution as result of the wire-fluid interaction is added. On top of that, a sinker is attached to the tip of the wire. A schematization will look like:

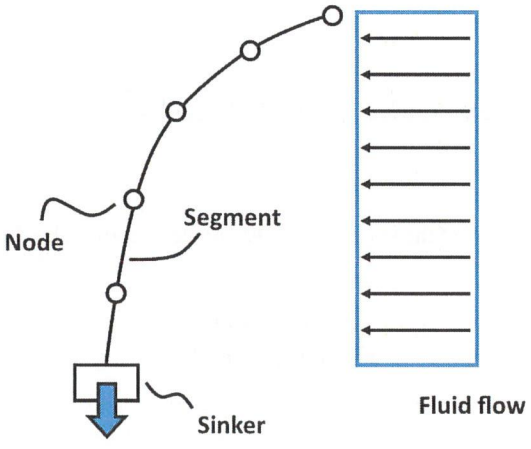

Figure D.3: Simplified schematization of a suspended wire in uniform flow

The presence of the weight of the sinker W_0 will have a similar role as the initial tension T_0 in Section D.1.1. Here the tangent of the wire shape at the tip is again zero. From hereon we follow the same procedure as Section D.1.2. The length of wire L is again subdivided in a number of elements n (discretization), with an element length dS. This automatically yields into a number of nodes of size $n+1$. The i indicates the node number starting from the tip of the wire (the location where the sinker is attached). These nodes are the points where acting wire forces per segment will be concentrated. Now the vertical force along the wire shape

consists out of a constant (submerged) sinker-weight and an increasing weight as result of the (submerged) wire self-weight and length. The horizontal force in each node consists out of the drag force:

$$F_{x;drag} = \frac{1}{2}\rho_w C_d(\theta) D_{wire} U^2 \quad [N/m] \tag{D.17}$$

As shown in Eq-D.17, the drag coefficient depends on the angle of incidence with respect to the fluid flow. Theoretically this angle of incidence will lead to a drag and a lift force. As the angles of incidence will be small, the lift contribution will be neglected. The tension in each node is composed out of the horizontal and vertical component and can simply be calculated using Pythagoras theorem:

$$T(i) = \sqrt{(F(i)_x)^2 + (F(i)_y)^2} \tag{D.18}$$

The elongation of each segment is again obtained by applying this tension:

$$dL(i) = dS \cdot \left(1 + \left(\frac{T(i)}{EA}\right)\right) \tag{D.19}$$

The cartesian coordinates of each node can be determined by the geometric relation between the vertical and horizontal forces. This ratio of forces will first can be expressed into an angle in each node. The angle of the complete segment is composed out of the angles of both nodes divided over two. When combined in one formula for x- and z- coordinates one obtains:

$$x(i) = x(i-1) + \left\{dS \cdot \left(1 + \left(\frac{T(i)}{EA}\right)\right)\right\} \cdot sin\left(\frac{\theta(i) + \theta(i-1)}{2}\right) \tag{D.20}$$

$$z(i) = z(i-1) + \left\{dS \cdot \left(1 + \left(\frac{T(i)}{EA}\right)\right)\right\} \cdot cos\left(\frac{\theta(i) + \theta(i-1)}{2}\right) \tag{D.21}$$

To change the origin from tip to top of the wire, one can again easily subtract the value for the last coordinate:

$$\begin{aligned} x'(i) &= x(i) - x(end) \\ z'(i) &= z(i) - z(end) \end{aligned} \tag{D.22}$$

The total elongation can be obtained by:

$$dL_{tot} = \sum_{i=1}^{N} dL(i) - L \qquad [m] \tag{D.23}$$

D.2.1. Angle of incidence

As shown in the expression for the drag (Eq-D.17), the magnitude of the force is dependent on the angle of incidence of the wire with respect to the fluid flow. A visual representation is shown in Figure D.4. This influence is taken into account by the drag coefficient C_d, which is dependent on the angle. A relation for the coefficient as function of the angle is found in Figure D.5 in [3] and can be written as $C_d(\theta) = 1.2 \cdot sin^2\theta$.

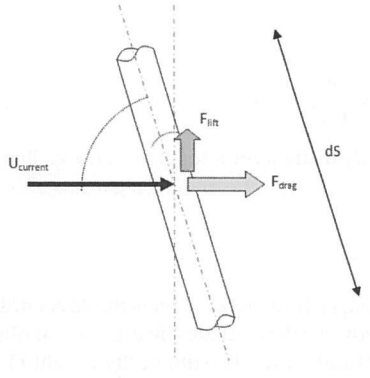

Figure D.4: Angle of incidence

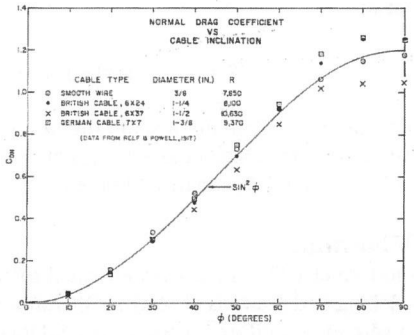

Figure D.5: Drag coefficient as function of the angle

D.2.2. Curvilinear Coordinates

In the suggested method the influence of lift was neglected. A method that includes lift in deriving the static configuration, is by curvilinear coordinates. In order to derive the force balance and in the end the static configuration of the wire, we employ the curvilinear axial coordinate *s*. The coordinate describes a curved path and will be inverted to cartesian coordinates to obtain the wire configuration. Forces acting on a differential segment of the wire are presented in Figure D.6.

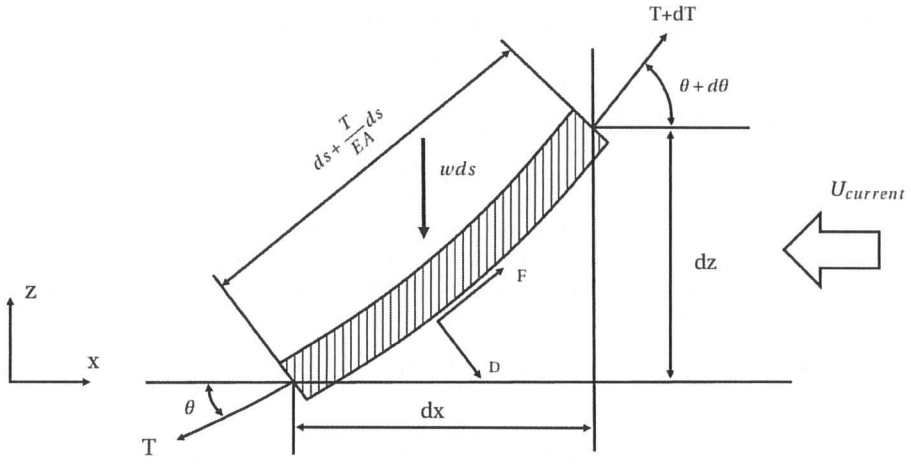

Figure D.6: Differential segment in curvilinear coordinates

Where:

ds	The length of the differential element	[m]	U	Current velocity	[m/s]
EA	Axial rigidity	[N/m]	F_n	Normal hydrodynamic force	[N]
T	Local tension	[N]	F_t	Tangential hydrodynamic force	[N]
w	Submerged weight wire per unit length	[kg/m]			

The forces acting on the differential element from figure D.6 can be expressed in force balances in tangential and normal direction.

Tangential direction:

$$(T+dt)\cos d\theta - T - w_n\, ds \sin\theta + F_t\left(ds + \frac{T}{EA}ds\right) = 0 \tag{D.24}$$

Normal direction:

$$(T+dT)\sin d\theta - w_n\, ds \cos\theta - F_n\left(ds + \frac{T}{EA}ds\right) = 0 \tag{D.25}$$

These balances can be turned into a set of differential equations. By using a numerical solver, e.g. Runge-Kutta, one can obtain the coordinates of the static configuration. For more information regarding this approach, the titles [10] and [37] can be addressed.

D.2.3. DNV Formula

The last method which will be incorporated into the validation section, is the general offset formula according to DNV - Modelling and Analysis of Marine Operations [8]. This method will calculate the offset of an object attached to a wire in an uniform current. As guidance note, it is assumed that the sum of the weight of the wire and submerged weight of the object are so large that the angle between wire and vertical is small. The horizontal offset can be derived analytically according to formula 5.2.2.2:

$$\xi_L = L\left(\frac{q}{w}k - \lambda\right) ln\left[\frac{k}{k+1}\right] + \frac{qL}{w} \quad [m] \tag{D.26}$$

Where k is the ratio between the weight of the lifted object and the weight of the wire;

$$k = \frac{W}{wL} \quad [-] \tag{D.27}$$

λ is the ratio between the drag on the lifted object, F_{D0} and the weight of the wire;

$$\lambda = \frac{F_{D0}}{wL} \quad [-] \tag{D.28}$$

The hydrodynamic drag force per unit length of wire is given by;

$$q = \frac{1}{2}\rho\, C_{Dn}\, D_c U_c^2 \quad [N/m] \tag{D.29}$$

This method is only applicable in case of a uniform current and considered as highly simplified. The reason for addressing these results is to judge the results of the previous methods in order of magnitude.

D.2.4. Validation

In the validation of the numerical approach, its results were compared to the outcome of both the curvilinear approach as the DNV formula. This is done for various input parameters. An example set of input parameters is given in Table D.1.

u_{cur}	0.25	[m/s]	D_{wire}	0.09	[m]
W_{obj}	$1 \cdot 10^3$	[kN]	$C_{d;wire}$	1.2	[-]
$F_{d;object}$	2500	[N]	w_{wire}	245.25	[N/m]

Table D.1: Validation parameters

In the first Figure D.7 the wire shape for given parameters is shown. The second Figure D.8 shows the offset of the tip of the wire as function of wire payout length for all three approaches. As shown in the figure, the lines cover each other (at least at this scale). However, the error with respect to the wire length, x_{diff}/L is in the order of $2.5 \cdot 10^{-5}$ [-].

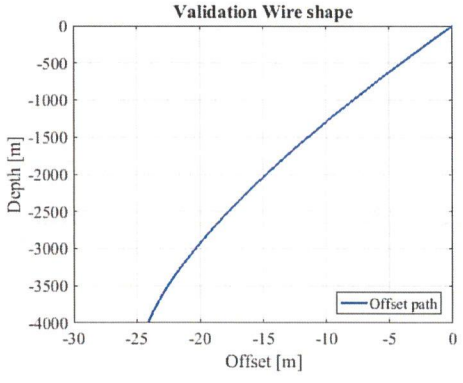

Figure D.7: Example validation wire shape

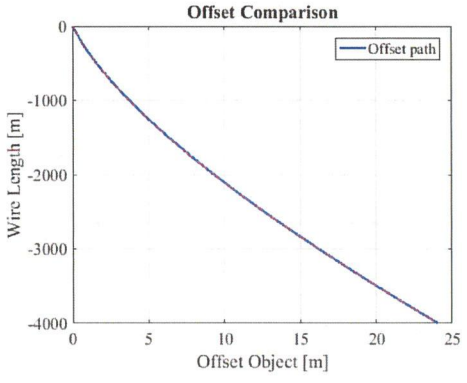

Figure D.8: Offset as function of payout length

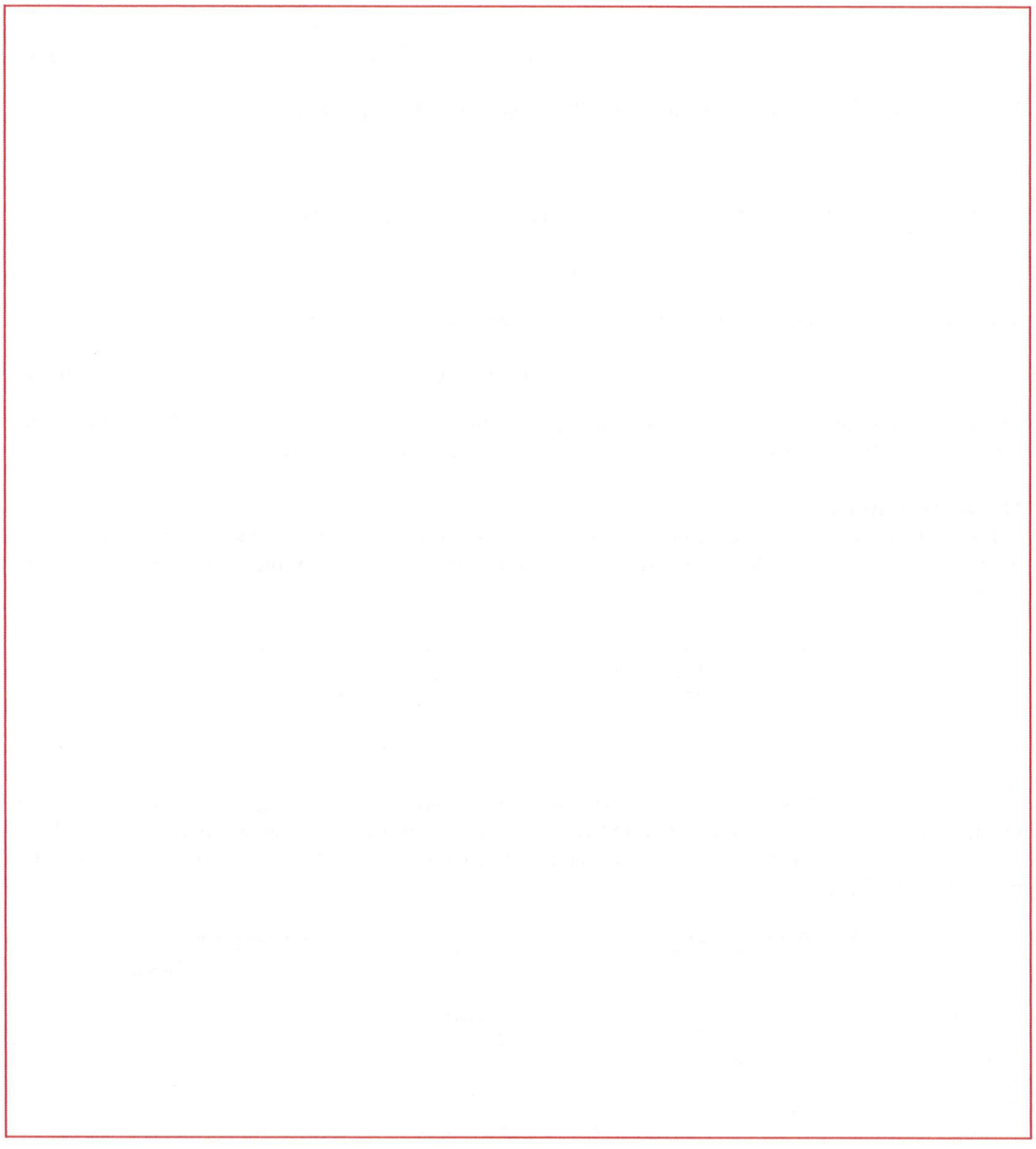

E

Mining Vessel

The following sections provide information with respect to the input data required and used for Seaway. The applied reference vessel VERSLUIS.049 - TANKER can be found in *Diktaat 438-A, Moederscheepsvormen* [38].

E.1. Vessel Data Sheet

Designation (VERSLUIS.049 TANKER)	**Symbol**	**Unit**	**Unit**
Length between perpendiculars	Lpp	[m]	277.9
Length Waterline	Lwl	[m]	280
Overall Breadth	Boa	[m]	44.8
Breadth Waterline	Bwl	[m]	44.8
Depth	D	[m]	NA
Draft Hull	T	[m]	16.6
Volume	λ	[m^3]	173243
Mass	W	[ton]	177574
Longitudinal Centre of Gravity wrt. App	LcG	[m]	145.0
Vertical Centre of Gravity wrt. base	KG	[m]	17.50 | 17.00
Transverse Metacentre Height	KM	[m]	18.05
Transverse Metacentre Height	Gmt	[m]	0.55 | 1.05
Radius of gyration around x-axis (0.35 · Boa)	Kxx	[m]	15.7
Radius of gyration around y-axis (0.3 · Lpp)	Kyy	[m]	83.4
Radius of gyrationaround z-axis (0.3 · Lpp)	Kzz	[m]	83.4

Table E.1: Vessel data sheet 1 - VERSLUIS.049 TANKER

File Name	**Ship Type**	**CB**	**CWL**	**CVP**	**L/B**	**B/D**	**LCB**
VERSLUIS.049	Tanker	0.842	0.897	0.938	6.2	2.7	2.28

Table E.2: Vessel data sheet 2 - VERSLUIS.049 TANKER

E.2. Lines Drawing

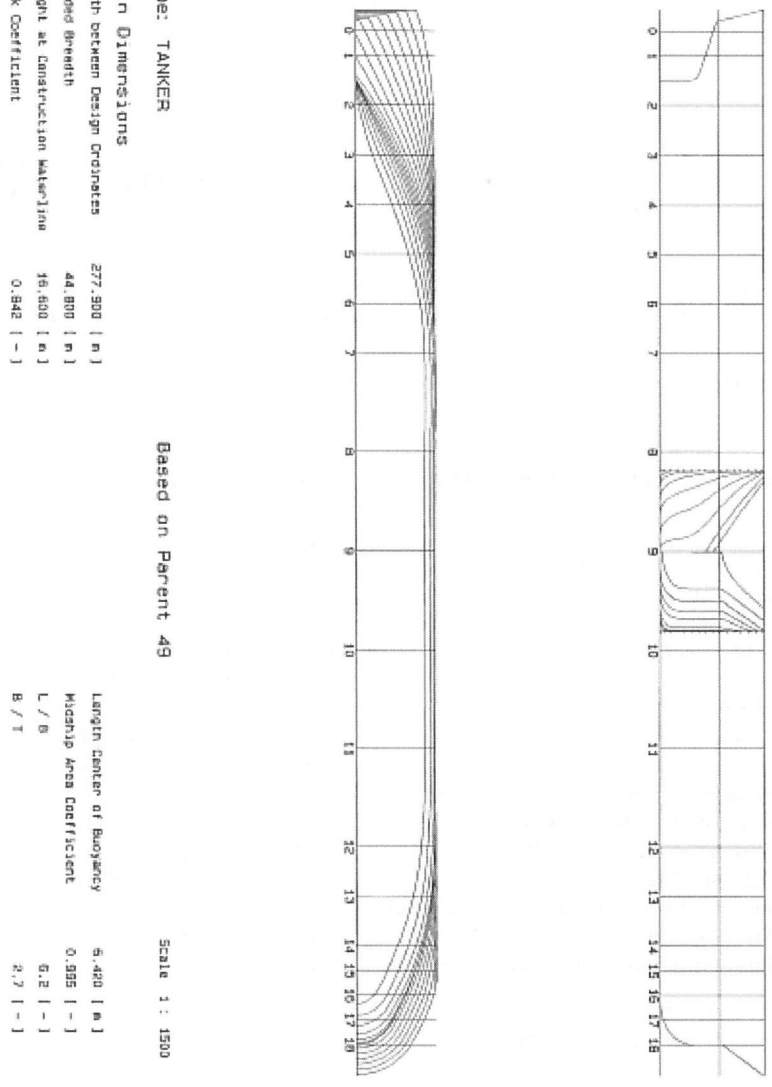

Figure E.1: VERSLUIS.049 TANKER - Lines drawing

F

Crane-tip motions

In order to calculate the dynamics of the system (wires, skips and collector) we are interested in the motions of the crane-tip in particular. The wires are attached to the crane-tip and the tip dictates the motion of the first wire node. In this study the computer Program Seaway is used to calculate the vessel response. The output of Seaway gives the RAO [m/m] and phase [Degr] of the six degrees of freedom in the ships center of gravity. To obtain the absolute motions of the crane-tip we are interested in, we need to post-process this data. This is done using superposition according to (Journee, Massie) [18] and will result in the RAO and phases for the point of interest; the crane-tip.

Absolute motions for a point of interest on the vessel P(x_b, y_b, z_b) are composed out of:

$$\begin{aligned} x_p &= x - y_b\psi + z_b\theta \\ y_p &= y + x_b\psi - z_b\phi \\ z_p &= z - x_b\theta + y_b\phi \end{aligned} \tag{F.1}$$

In which x, y and z are respectively *surge*, *sway* and *heave*, and ψ, θ and ϕ are respectively *roll*, *pitch* and *yaw*. These contributions are the motions of and about the center of gravity of the vessel. The x_b, y_b and z_b are the so-called body bound coordinates of the point of interest with respect to the center of gravity of the vessel, see Figure F.1. This type of notation was formerly introduced as a local coordinate system.

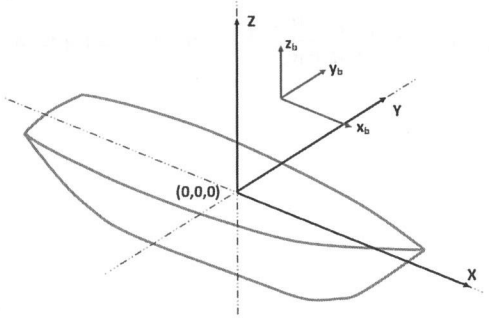

Figure F.1: Body-bound axis system

Example Vertical motion

In this study we are particularly interested in the vertical motion of the crane tip, z_P. P(x_b, y_b, z_b) is referred to as the location of the point of interest (crane-tip) with respect to the CoG of the vessel. In the absolute vertical motion of z_p contribute heave, roll and pitch motions. To gain insight, these contributions will be fully elaborated. For convenient writing, the vertical motion of z_P is now written as η.

$$\begin{aligned}\eta(\omega,t) &= z - x_b\theta + y_b\phi \\ &= z_a\,cos(\omega t+\epsilon_{z\zeta}) - x_b\theta_a\,cos(\omega t+\epsilon_{\theta\zeta}) + y_b\phi_a\,cos(\omega t+\epsilon_{\phi\zeta}) \\ &= \{z_a\,cos(\epsilon_{z\zeta}) - x_b\theta_a\,cos(\epsilon_{\theta\zeta}) + y_b\phi_a\,cos(\epsilon_{\phi\zeta})\}\cdot cos(\omega t) \\ &\quad - \{z_a\,sin(\epsilon_z\zeta) - x_b\theta_a\,sin(\epsilon_{\theta\zeta}) + y_b\phi_a\,sin(\epsilon_{\phi\zeta})\}\cdot sin(\omega t)\end{aligned} \tag{F.2}$$

Here the subscript a indicates the amplitudes of the center of gravity of the vessel. The subscript b is logically related to the body bound coordinates. Motion η has been obtained by linear superposition of three harmonic motions. This means that motion η will be of harmonic nature as well:

$$\begin{aligned}\eta(\omega,t) &= \eta_a\,cos(\omega t+\varepsilon) \\ &= \{\eta_a\,cos(\varepsilon)\}\cdot cos(\omega t) - \{\eta_a\,sin(\varepsilon)\}\cdot sin(\omega t)\end{aligned} \tag{F.3}$$

The in-phase term $\eta_a\,cos(\varepsilon_{\eta\zeta})$ and out-of-phase term $\eta_a\,sin(\varepsilon_{\eta\zeta})$ can be found by equating the terms in Eq-F.3 and Eq-F.2. This results into:

$$\begin{aligned}\eta_a\,cos(\varepsilon_{\eta\zeta}) &= z_a\,cos(\varepsilon_{z\zeta}) - x_b\theta_a\,cos(\varepsilon_{\theta\zeta}) + y_b\phi\,cos(\varepsilon_{\phi\zeta}) \\ \eta_a\,sin(\varepsilon_{\eta\zeta}) &= z_a\,sin(\varepsilon_{z\zeta}) - x_b\theta_a\,sin(\varepsilon_{\theta\zeta}) + y_b\phi\,sin(\varepsilon_{\phi\zeta})\end{aligned} \tag{F.4}$$

In which we can find the amplitude and phase angle of the point of interest P(x_b, y_b, z_b).

Amplitude (η_a):

$$\eta_a = \sqrt{(\eta_a\,sin(\varepsilon_{\eta\zeta}))^2 + (\eta_a\,cos(\varepsilon_{\eta\zeta}))^2} \tag{F.5}$$

The phase shift $(\varepsilon_{\eta\zeta})$

$$\varepsilon_{\eta\zeta} = arctan\left\{\frac{\eta_a sin(\varepsilon_{\eta\zeta})}{\eta_a cos(\varepsilon_{\eta\zeta})}\right\} \qquad with \quad 0 \le \varepsilon_{\eta\zeta} \le 2\pi \tag{F.6}$$

G

Dynamic Model - Derivation and Validation

This is appendix contains the derivation of the complete dynamic model. The dynamic system in Chapter 8, was composed gradually consisting out of an axial and a transversal part. The axial model (1-dimensiona)l serves as base. The transversal (2-dimensional) derivation follows from the axial model. In this appendix the same approach is applied, starting with the discretization of a wire by finite elements. In the transversal part an additional dimension is introduced.

G.1. One Dimensional

G.1.1. Derivation

Modelling a wire originates in the equation of motion of a rod. For convenience we neglect the gravity contribution. The equation of motion can be written as:

$$\rho A \frac{\partial^2 u}{\partial t^2} - EA \frac{\partial^2 u}{\partial z^2} = 0 \qquad for \quad -L < z < 0 \tag{G.1}$$

In this equation of motion, the ρ is the material density [kg/m^3], the A represent the area [m^2] and E the elastic modulus [N/m^2]. When written in LaGrangian energy form, this results into the following notation:

$$\mathscr{L} = T - V = \int_l \int_A \left(\rho(z) V(z)^2 - E(z) \frac{du(z)}{dz} \frac{du(z)}{dz} \right) dA\, dz \tag{G.2}$$

Here the equation consists out of a kinetic and potential energy part. We assume the axial deformations to be small. The material is considered homogeneous, isotropic and prismatic. This LaGrangian form still represents a continuous piece of material, next step is dividing the wire into a set of discrete point (discretization). If the wire would consist out of two points (located at the outermost points of the wire), the situation in between these point can be approximated by a linear function. In this manner the wire is turned from a infinite number of degrees of freedom, into just two degrees of freedom. The applied linear function is called a shape function.

Shape Function

The linear shape function for a piece of wire can be graphically expressed as:

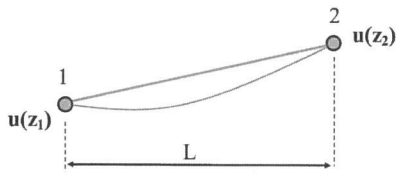

Figure G.1: Linear shape function

In this figure the blue line represents the continuous situation, the red line the approximated. When the accuracy of approximation should be increased, the number of degrees of freedom can be increased. Say, for this length of wire l, from 2 nodes to e.g. 10 nodes. In this way the numerical error can be reduced. If we would apply this method to the wire this results into:

$$\begin{aligned} u(z) &= \frac{u_2 - u_1}{l} z + u_1 \\ \frac{\partial u}{\partial z} &= \frac{u_2 - u_1}{l} \end{aligned} \tag{G.3}$$

and

$$V(z) = \frac{V_2 - V_1}{l} z + V_1 \tag{G.4}$$

Where V represent the time related part and u the spatial part with respect to the equation of motion. When implemented into the continuous LaGrangian form, this results into:

$$\mathscr{L} = \frac{A}{2} \int_l \left(\rho \left(\frac{V_2 - V_1}{l} z + V_1 \right)^2 - E \left(\frac{u_2 - u_1}{l} \right)^2 \right) dz \tag{G.5}$$

After taking the derivatives with respect to u_1 and u_2, the obtained equation of motion in matrix form can be written as:

$$\frac{\rho A l}{6} \cdot \begin{pmatrix} 2 & 1 \\ 1 & 2 \end{pmatrix} \cdot \begin{pmatrix} \ddot{u}_1 \\ \ddot{u}_2 \end{pmatrix} + \frac{EA}{l} \begin{pmatrix} 1 & -1 \\ -1 & 1 \end{pmatrix} \cdot \begin{pmatrix} u_1 \\ u_2 \end{pmatrix} = 0 \tag{G.6}$$

Assembling
System G.6 represents a situation consisting out of a single element (and two nodes). Increasing the number of elements can be done by assembling blocks of a single element. The results for two segments (and three nodes) is given in System G.7. For multiple elements this method holds.

$$\frac{\rho A l}{6} \cdot \begin{pmatrix} 2 & 1 & 0 \\ 1 & 4 & 1 \\ 0 & 1 & 2 \end{pmatrix} \cdot \begin{pmatrix} \ddot{u}_1 \\ \ddot{u}_2 \\ \ddot{u}_3 \end{pmatrix} + \frac{EA}{l} \begin{pmatrix} 1 & -1 & 0 \\ -1 & 2 & -1 \\ 0 & -1 & 1 \end{pmatrix} \cdot \begin{pmatrix} u_1 \\ u_2 \\ u_3 \end{pmatrix} = 0 \tag{G.7}$$

G.1.2. Numerical implementation and Validation

The system of differential equations (Eq-G.7) can be solved using the built-in ODE45-solver in Matlab. Validation of the numerical method is done by comparison with analytical results, e.g. initial displacement or forced vibrations. The equation of motion of a piece of wire expressed as a single-degree-of-freedom system can be written as:

$$\frac{1}{3} mL\ddot{u} + \frac{EA}{L} u = 0 \tag{G.8}$$

Here m is the mass per unit length, L the total wire length and $\frac{EA}{L}$ the wire stiffness. The analytical expression for the response as function of time can be written as Eq-G.9. Where ω_n is the systems natural frequency.

$$u(t) = u_0 \cos(\omega_n t) = \frac{v_0}{\omega_n} \sin(\omega_n t) \tag{G.9}$$

We apply for example an initial displacement of 1m. When we compare the numerical and analytical results, we obtain Figure G.2.

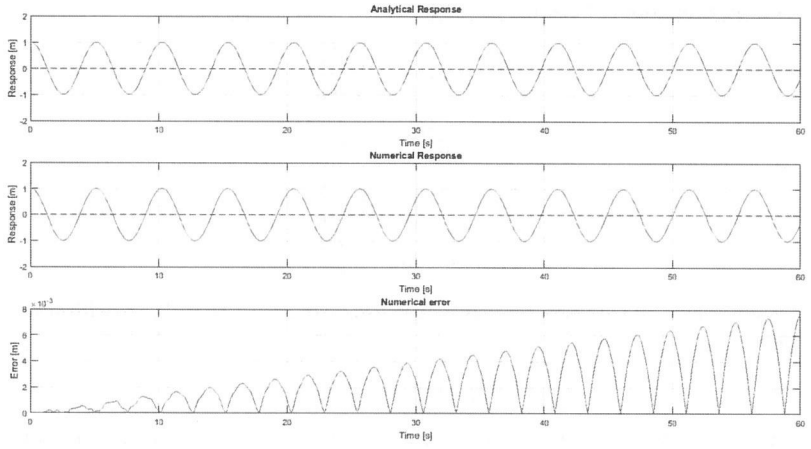

Figure G.2: Validation single element

In Figure G.2, the first two subplots show the analytical and numerical response of the wire, given an initial displacement of 1m. The last subplot shows the numerical error between the analytical and numerical result. The magnitude of this error can be reduced by increasing the number of elements.

G.2. Two Dimensional

Modelling the wire in two dimensions can be done by applying the same theory of section G.1. This method is better known as the lumped-mass finite element method. By adding an extra dimension, the shape of the wire can be taken into account, under the assumption that its bending stiffness (EI) is zero. Deformations only take place axially, captured by the introduced equation of motion of a rod (Eq-G.1).

G.2.1. Derivation

?? In the two-dimensional approach, additional degrees of freedom in z-direction are required. The result is doubling of the number of equations of motion. The stiffness contribution in the equation of motion will be a result of the absolute spring elongation. Absolute elongation can be calculated by both the change in position in x-direction and z-direction, Figure G.3.

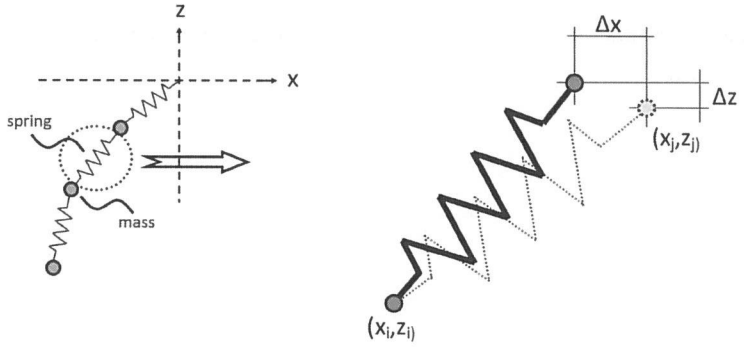

Figure G.3: Spring force as result of elongation

The current length of the spring (l_c) can be calculated by its coordinates:

$$l_{cur} = \sqrt{(z_j - z_i)^2 + (x_j - x_i)^2} \tag{G.10}$$

The spring forces in adjacent nodes become:

$$\begin{aligned} F_{x;j} &= +k(l_{cur} - l)\frac{\delta x}{l_{cur}} \\ F_{x;i} &= -k(l_{cur} - l)\frac{\delta x}{l_{cur}} \\ F_{z;j} &= +k(l_{cur} - l)\frac{\delta z}{l_{cur}} \\ F_{z;i} &= -k(l_{cur} - l)\frac{\delta z}{l_{cur}} \end{aligned} \tag{G.11}$$

As a result of this approach, the stiffness matrix as used in System G.7 is replaced with force terms. The notation now reads:

$$M\ddot{u} + f(q_n) = F_{ext} \tag{G.12}$$

Here $f(q_n)$ is a function dependent on the force terms as a result of displacement and stiffness for each element. The axial motion in the wire is still denoted as u.

G.2.2. Validation

The validation of the two-dimensional model is done by a double pendulum [39]. As initial condition a rotational displacement of the first bar of 30 °is given. The system of equations of the double pendulum is solved using Matlab as well.

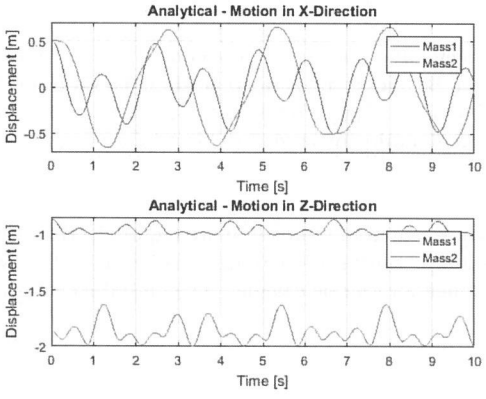

Figure G.4: Wire interaction - Single wire

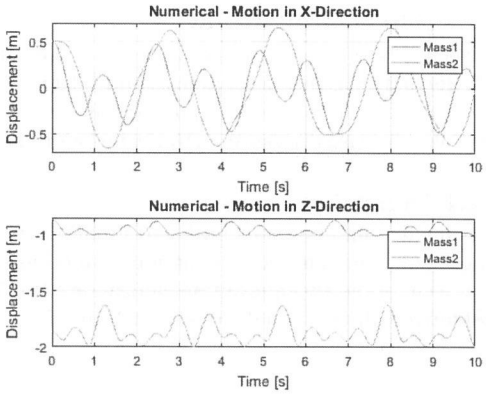

Figure G.5: Wire interaction - Double wire

A second validation is done by a double pendulum JAVA-script [9].

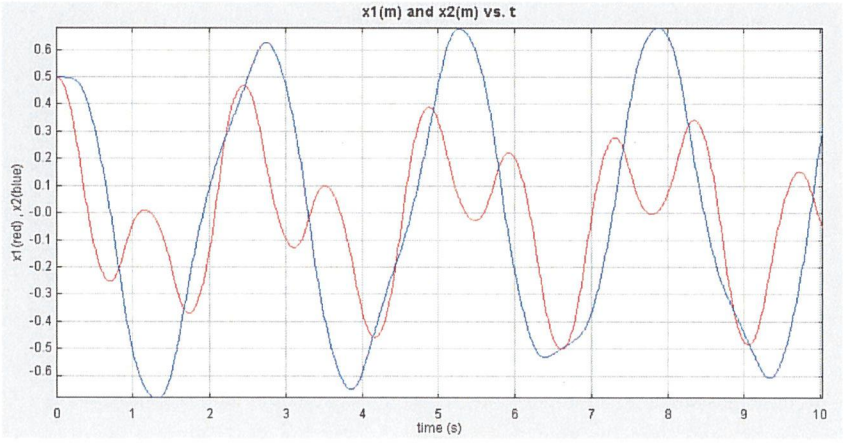

Figure G.6: Second validation

H

Rotational Stability

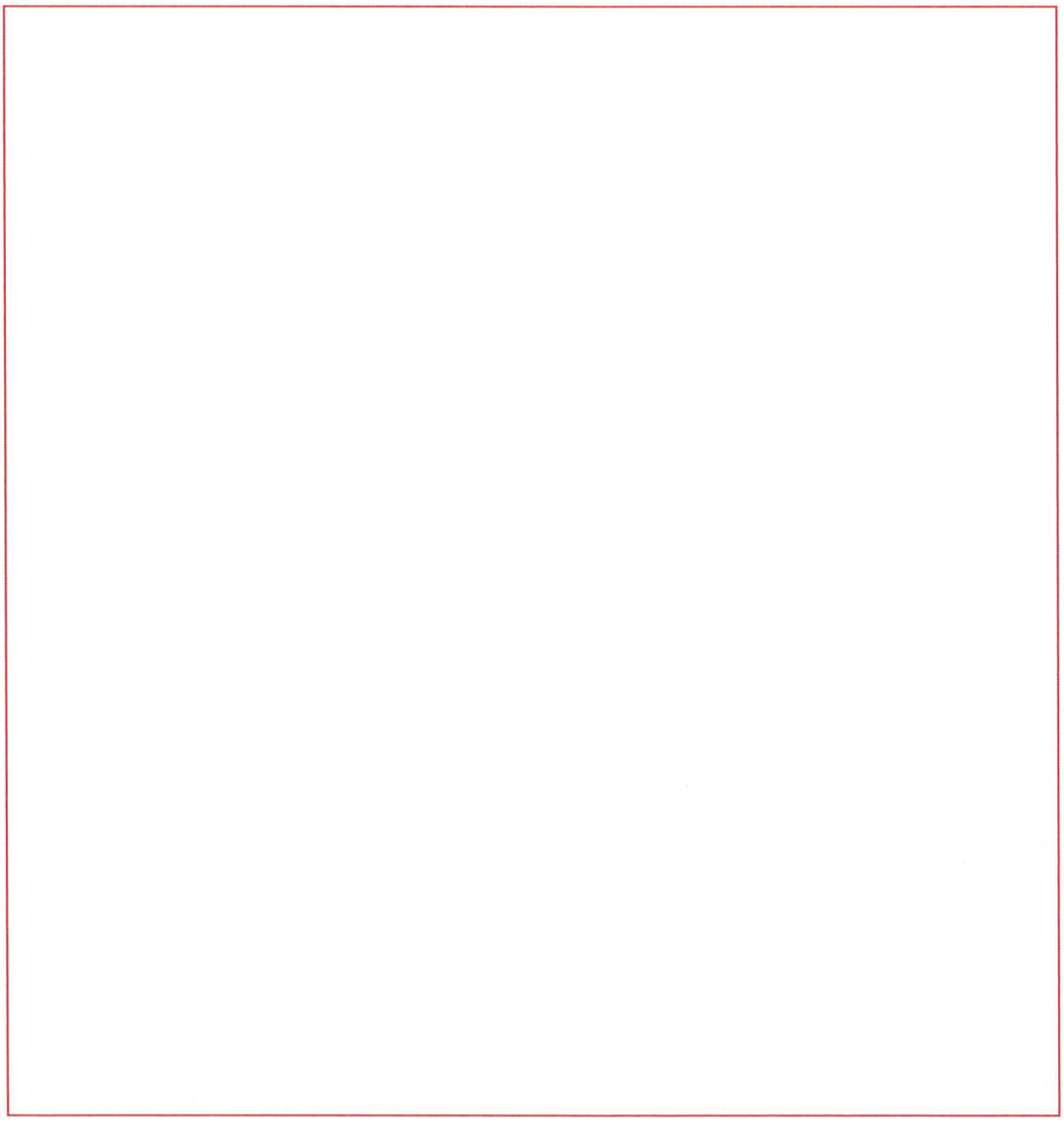

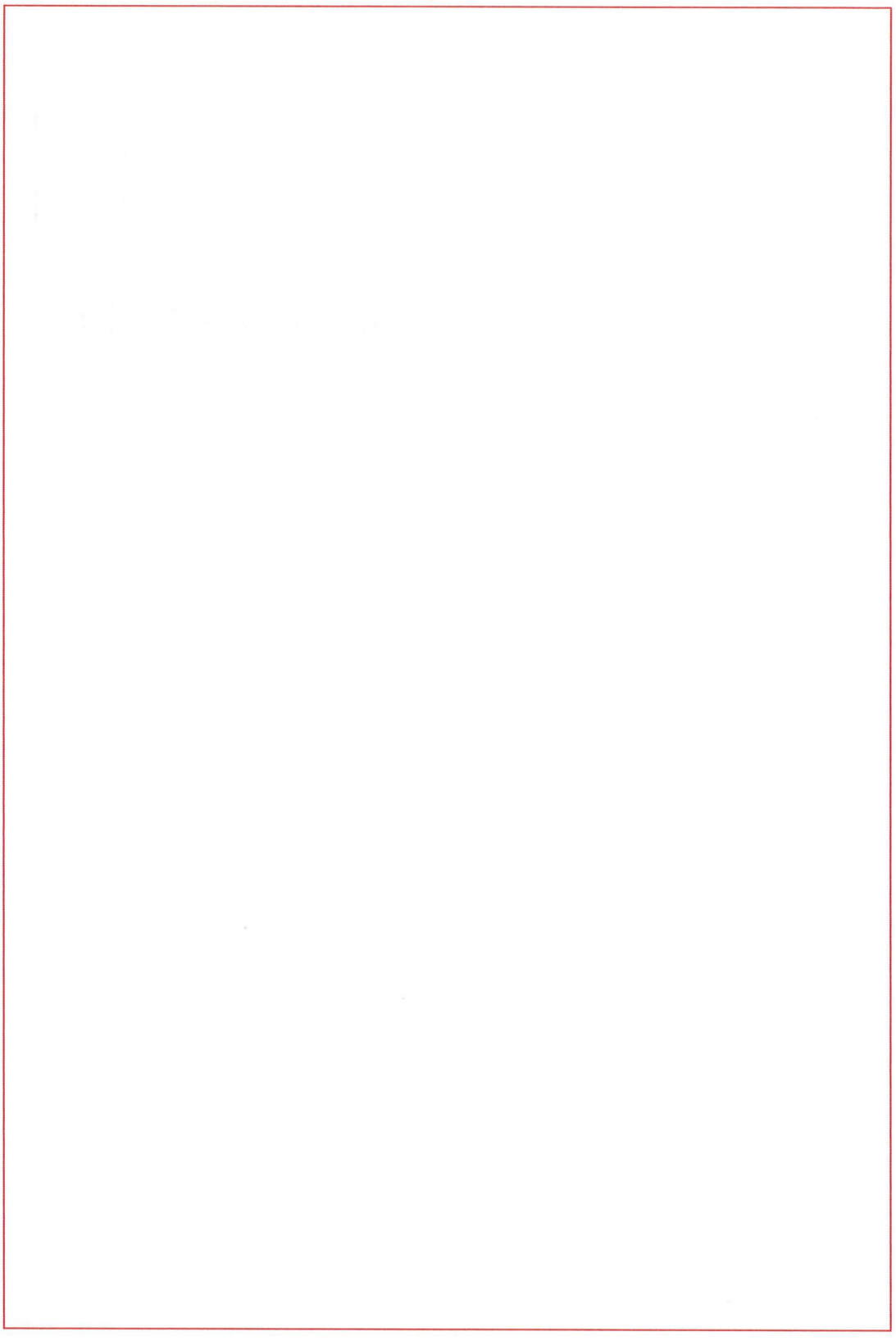

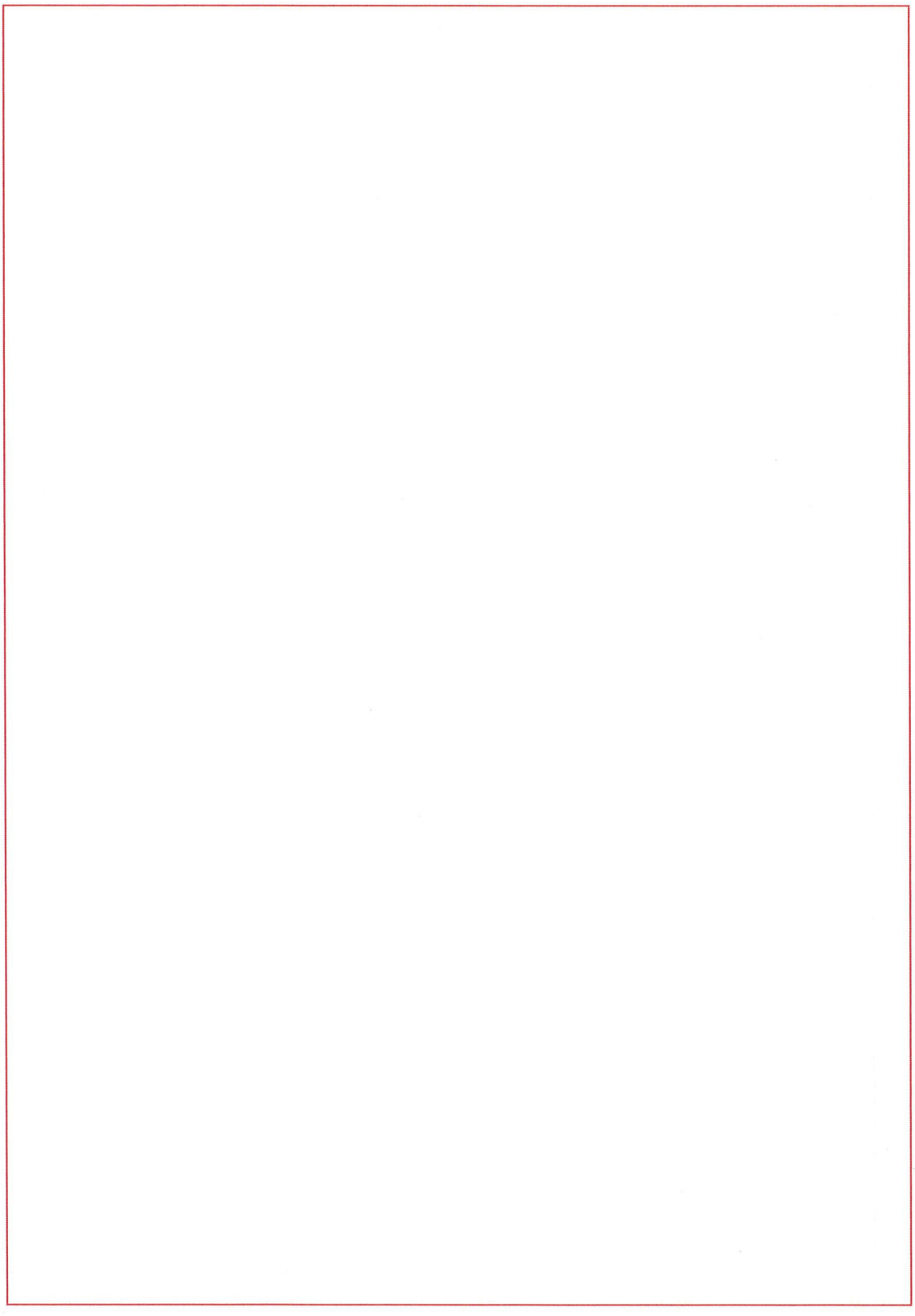

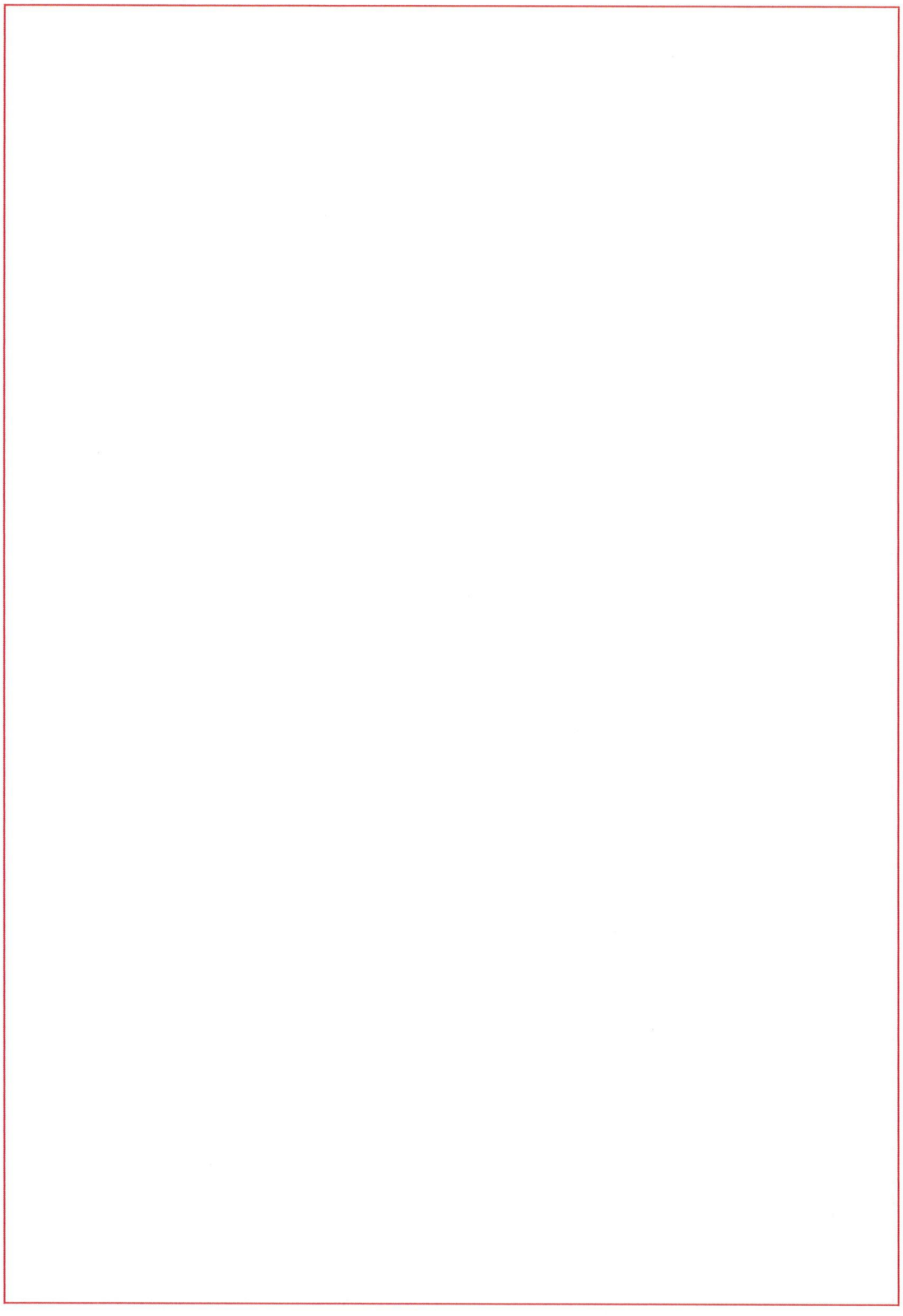

Bibliography

[1] B. Agarwal, P. Hu, M. Placidi, H. Santo, and J. J. Zhou. *Feasibility Study on Manganese Nodules Recovery in the Clarion-Clipperton Zone*, volume 2. LRET Collegium, 2012.

[2] A.F. Amos and O.A. Roels. Environmental Aspects of Manganese Module Mining. *Marine Policy*, 1(2): 156–163, 1977.

[3] W H Bell. *Static Analysis of Single-Point Moorings*. Institute of Ocean Sciences, Patricia Bay, 1977.

[4] R.D. Blevins. Flow Induced Vibration, 2001.

[5] UK Caley Offshore Handling Systems. The Right Wires, 2017.

[6] J.P. Den Hartog. *Mechanical Vibrations*. Dover Publications, 1956.

[7] Det Norske Veritas. Environmental Conditions and Environmental Loads. *DNV*, pages 9–123, 2010.

[8] Det Norske Veritas. Modelling and Analysis of Marine Operations. *DNV*, RP-H103(April), 2011.

[9] T Dooling. Double Pendulum; Elastic rod model, 2013. URL `http://www.compadre.org/osp/`.

[10] O.M. Faltinsen. *Sea loads on ships and offshore structures*, volume 1. Cambridge University Press, 1990.

[11] G.Z. Forristall and C.K. Cooper. Design Current Profiles Using Empirical Orthogonal Function (EOF) and Inverse FORM Methods. *Offshore Technology Conference*, 1997.

[12] R. Ghosh, A.K.;Mukhopadhyay. *Mineral Wealth of the Ocean*. Balkema Rotterdam, Rotterdam, 2000.

[13] J.R. Hein, K. Mizell, A. Koschinsky, and T.A. Conrad. Deep-ocean mineral deposits as a source of critical metals for high- and green-technology applications: Comparison with land-based resources. *Ore Geology Reviews*, 51(July):1–14, 2013.

[14] H.M. Irvine. *Cable Structures*. MIT Press, Cambridge, Massachusetts and London, England, 1981.

[15] P. Jankowski, E. Heymann, P. Chwastiak, A. See, P. Munro, and I. Lipton. Offshore Production System Definition and Cost Study. *Nautilus Minerals*, 1(June):81, 2010.

[16] M. Jardin. Measuring Mass Moment of Inertia with a Bifilar Pendulum, 2016.

[17] J.M.J. Journee. Brochure Seaway, 2001.

[18] W.W. Journee, J.M.J., Massie. *Offshore Hydromechanics*, volume 47. Delft University of Technology, 2002.

[19] C. Keijdener. Discretization in space; Lecture notes Computational Dynamics for Offshore Structures. Technical report, Delft University of Technology, Delft, 2015.

[20] Lankhorst. Deep Water Deployment Ropes. *Lankhorst Ropes Brochure*, pages 0–3, 2017.

[21] K. Larsen. Subsea Lifting and Crane Operations; Lecture Slides, 2017.

[22] F. Lorenz. Manganknollen vom Meeresgrund; Goldrausch im Pazifik, 2016.

[23] R. McCulley. Fiber Flexes Deepwater Muscle. *Offshore Engineer*, 2010.

[24] V.E. McKelvey. Subsea Mineral Resources. *US Geological Survey Bulletin*, 1689 A:1–106, 1986.

[25] J.L. Mero. Oceanic Mineral Resources. *Futures*, 1(2):125–141, 1968. ISSN 00163287.

[26] A.V. Metrikine. *Dynamics, Slender Structures and an Introduction to Continuum Mechanics*. Delft University of Technology, 2015.

[27] W.H. Michel. Sea Spectra Revisited. *Marine Technology*, 36:211–227, 1999.

[28] A.E. Molly. Sea floor bathymetry near the Clarion and Clipperton fracture zones. *International Hydrographic Review*, 1963.

[29] S.K. Niedzwecki, J.M. ; Thampi. Snap Loading of Marine Cable Systems. *Applied Ocean Research*, 13(5), 1991.

[30] Orcina. Orcina - Payload Handling: F02 Passive Compensation, 2017.

[31] A.M. Post. *Deep Sea Mining and the Law of the Sea.* Martinus Nijhoff Publishers, The Hague, 1983.

[32] S. J Rowe, B. Mackenzie, and R. Snell. Deepwater Installation of Subsea Hardware. *10th Offshore Symposium*, pages 1–9, 2001.

[33] S.A. Schulte. Vertical transport methods for Deep Sea Mining. *Master Thesis, Delft University of Technology*, 2013.

[34] R. Sharma. *Deep-Sea Mining: Resource Potential, Technical and Environmental Considerations.* Springer-Verlag, 2017. ISBN 9783319525563.

[35] R.F. Steidel. *An Introduction to Mechanical Vibrations.* Wiley, 3rd editio edition, 1989.

[36] Virginie Tilot. Biodiversity and Distribution of the Megafauna: The Polymetallic nodule ecosystem of the eastern equatorial Pacific Ocean. *Intergovernmental Oceanographic Commission*, 1:1–346, 2006.

[37] M. S. Triantafyllou and F. S. Hover. *Maneuvering and Control of Marine Vehicles.* MIT Press, 2003.

[38] A. Versluis. *Diktaat 438-A, Moederscheepsvormen.* Delft University of Technology, Delft, 2009.

[39] E. Weisstein. Double Pendulum, 2007. URL `scienceworld.wolfram.com/physics/doublependulum.html`.

[40] J. K. Woodacre, R. J. Bauer, and R. A. Irani. A review of vertical motion heave compensation systems. *Ocean Engineering*, 104:140–154, 2015.

[41] L.I.U. Xiao-zhou, H.U. ; Shoa-jun. Numerical Simulation of Deepwater Deployment for Offshore Structures. 2015.